The Dissertation Committee for Yiqun Wang
certifies that this is the approved version of the following dissertation:

Measurement of Inclusive Forward Neutral Pion Production in 200 GeV Polarized Proton-Proton Collisions at RHIC

Committee:

Jerry Hoffmann, Supervisor

C. Fred Moore, Supervisor

Takeshi Udagawa

Peter Riley

William T. Guy (Jr.)

Robert L. Ray

Measurement of Inclusive Forward Neutral Pion Production in 200 GeV Polarized Proton-Proton Collisions at RHIC

by

Yiqun Wang, B.S.

DISSERTATION

Presented to the Faculty of the Graduate School of

The University of Texas at Austin

in Partial Fulfillment

of the Requirements

for the Degree of

DOCTOR OF PHILOSOPHY

THE UNIVERSITY OF TEXAS AT AUSTIN

August 2004

Dedicated to my wife Ni Mei.

Acknowledgments

I wish to thank the multitudes of people who helped me. Frist of all, I would like to thank my advisors, Prof. C. Fred Moore and Prof. Jerry Hoffmann, who helped me at the most difficult time when I switched my field from string theory to experimental high energy nuclear physics. Without their heartwarming support and patience, I would not be able to finish my degree. Next, my thanks go to STAR spin collaboration, most notably to Leslie Bland, Akio Ogawa, Greg Rakness, who welcomed me into the spin group and helped and guided me through the my research at BNL. My thanks also go those who help me .

Measurement of Inclusive Forward Neutral Pion Production in 200 GeV Polarized Proton-Proton Collisions at RHIC

Publication No. ____________________

Yiqun Wang, Ph.D.
The University of Texas at Austin, 2004

Supervisors: Jerry Hoffmann
C. Fred Moore

Measurement of inclusive forward π^0 production in the first polarized p-p collision at $\sqrt{s} = 200$ GeV was achieved using a prototype Forward (neutral) Pion Detector. The invariant differential cross section was consistent with next-to-leading order perturbative QCD calculation. Large positive analyzing power was found for large Feynman-x ($x_F > 0.3$). In addition, a new analysis program was developed for the upgraded Forward Pion Detector (FPD).

Table of Contents

List of Tables

List of Figures

Chapter 1

Introduction

Spin is inherently quantum mechanical. To really understand the structure of nucleons, it is necessary to also understand their spin structures, namely how the quark and gluon constituents contribute to the overall nucleon spin. Earlier polarized deep inelastic scattering experiments [1–3] had establish that quarks (and anti-quarks) account for only a small fraction ($\approx 20\%$) of the proton's spin. The remaining part must come either from gluon spin or orbital angular momenta of quarks and gluons.

Polarized proton scattering provides another way to look at the spin structures of protons. The probes are quarks and gluons, in contrast to polarized leptons in the deep inelastic scattering experiments. In an earlier Fermilab experiment (E704) [4] [5] (p-p and $\bar{p}$-p collisions against polarized fixed target), large values of analyzing power A_N (defined in Equation 1.1) were observed for pion production at $\sqrt{s} = 20$GeV (Figure 1.1). This was quite unexpected, as the naive perturbative QCD (pQCD) prediction was that A_N should be very small (see Section 1.2). However, at such energy and p_T (about a few GeV), it is not clear whether we can completely trust pQCD calculations. Shortly afterwards, a few theoretical models emerged. Although the proposed mechanisms differ from each other, they all give a non-zero result at higher energy, where we hope pQCD would yield more reliable predictions.

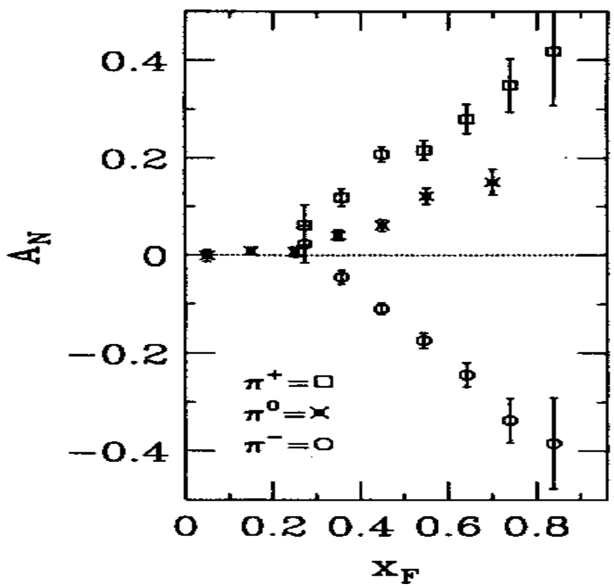

Figure 1.1: E704 result at $\sqrt{s} = 20$ GeV, p_T =0.5-2.0 GeV/c.

At a center-to-mass energy of $\sqrt{s} = 200$GeV, experiments have been conducted at RHIC (Relativistic Heavy Ion Collider), utilizing the polarized proton beams. This was the first time that polarized proton beams were made available in collider storage rings, utilizing a new technology called “Siberian Snakes” [6]. Previous experiments on polarized proton collisions always used polarized protons as fixed targets. As such, the $\sqrt{s}$ could not be as high as desired. It is not easy to obtain polarized proton beams in an accelerator. Electrons and positrons can developed significant polarization due to the Sokolov-Ternov effect [7] as they are extremely light particles ($M_e \approx 0.5$ MeV).

Protons, on the other hand, are quite heavy ($M_p = 928$ MeV), so they will not develop polarization by interacting with the synchrotron radiation. Polarized protons must be prepared beforehand, and injected and accelerated in the storage rings. However, there are numerous resonances that could depolarize the protons during the ramping of beam. These problems were overcome by a pair of the so-called "Siberian Snakes", which flip the polarization of the protons. In one revolution around the accelerator ring, the polarization is up for half of the cycle and down for the other half. Thus, the effects of resonances were almost canceled out and the polarization of the injected protons were large preserved.

During run FY02 a prototype Forward Pion Detector (pFPD) was commissioned, and high energy π^0 were observed. Subsequently, an upgrade installation of FPD was performed during the shutdown following run FY02. Run FY03 was the first year that the new FPD took data. This paper will present the results obtained from FY02 run and a new analysis program developed for the upgraded FPD. Data analysis for run FY03 data is still on-going, and the results should follow soon.

1.1 Definition of measurement

We begin by defining the single spin asymmetry and cross section measurements made by the FPD detectors. First, let's define our coordinate system (Figure 1.1). Polarized proton beam is coming along the negative z axis (for East-side FPD analysis) and its polarization points along either $+\hat{j}$ (up) or $-\hat{j}$ (down). The positive y axis is pointing upward.

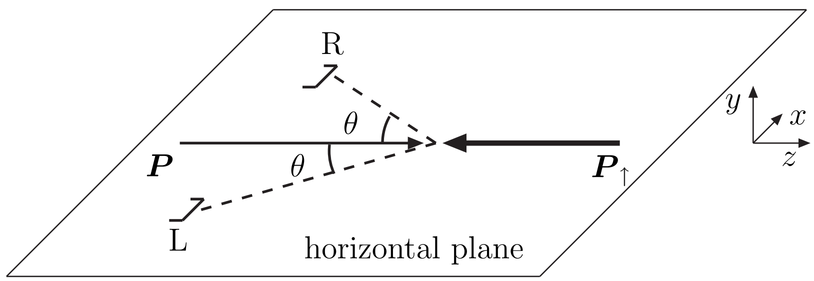

Figure 1.2: The STAR coordinate frame.

1.1.1 Single Spin Asymmetries

The analyzing power A_N for single spin asymmetry, the physical quantity that we want to measure, is defined in terms of matrix elements

$$A_N = \frac{\sigma_+ - \sigma_-}{\sigma_+ + \sigma_-}\,, \tag{1.1}$$

where $\sigma_{+(-)}$ is the cross section without summing over the spin state of one of the protons. A priori, A_N can be anywhere between -1 and 1. The "spin asymmetry" ϵ is $\epsilon = P_{beam} A_N$, where P_{beam} is the average beam polarization of one of the proton beam (usually the incoming proton beam).

To measure single spin asymmetries for inclusive π^0 production at RHIC, we do the following counting experiment: since there is a preferred direction (the polarization of incoming proton) in the transverse plane, we want to know whether the number of produced π^0 is dependent on the azimuthal angle ϕ of the detected π relative to the polarization axis of the incoming proton beam (In Figure 1.3, the detector is at $\phi = 90°$).

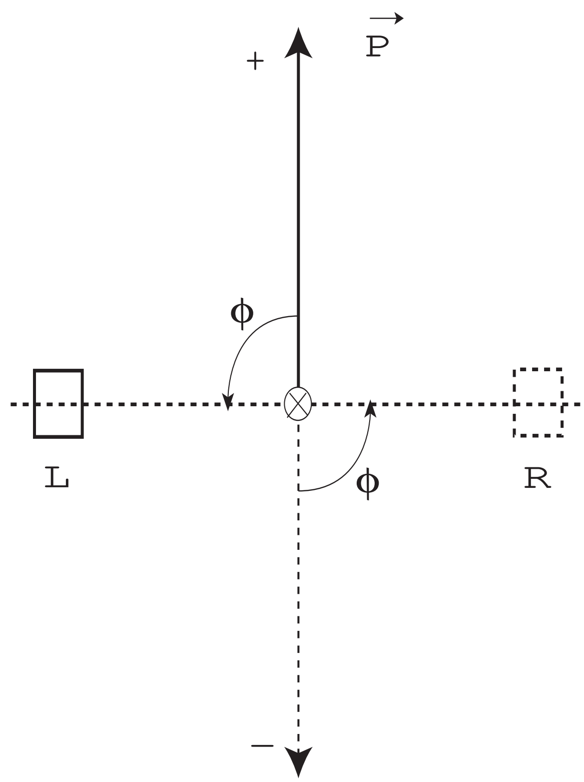

Figure 1.3: Left-right single spin asymmetry.

For a single-arm (detector L for example) measurement of single spin asymmetries,

$$P_{beam}A_N = \frac{N_+/\mathcal{L}_+ - N_-/\mathcal{L}_-}{N_+/\mathcal{L}_+ + N_-/\mathcal{L}_-} = \frac{N_+ - \mathcal{R}N_-}{N_+ + \mathcal{R}N_-}\,, \tag{1.2}$$

where P_{beam} is the average beam polarization, $N_{+(-)}$ is the number of π^0 detected at L when the beam polarization is vertically up (down), $\mathcal{L}_{+(-)}$ is the luminosity of collision with polarization vertically up (down), and $\mathcal{R}$ is spin-dependent relative luminosity $\mathcal{R} = \mathcal{L}_+/\mathcal{L}_-$, and A_N is the analyzing power.

Next we consider a left-right symmetric detector set-up (detector L and R). Generally, L and R may have different acceptance and efficiency factors Ω_L and Ω_R. Because of rotation invariance, $N_-^L/(\Omega_L\mathcal{L}_-) = N_+^R/(\Omega_R\mathcal{L}_+)$ and $N_+^L/(\Omega_L\mathcal{L}_+) = N_-^R/(\Omega_R\mathcal{L}_-)$, the asymmetry $\epsilon \equiv P_{beam}A_N$ is

$$\begin{aligned}
\epsilon &= \frac{N_+^L/(\Omega_L\mathcal{L}_+) - N_-^L/(\Omega_L\mathcal{L}_-)}{N_+^L/(\Omega_L\mathcal{L}_+) + N_-^L/(\Omega_L\mathcal{L}_-)} \\
&= \frac{N_+^L/(\Omega_L\mathcal{L}_+) - N_+^R/(\Omega_R\mathcal{L}_+)}{N_+^L/(\Omega_L\mathcal{L}_+) + N_+^R/(\Omega_R\mathcal{L}_+)} \\
&= \frac{N_+^L/\Omega_L - N_+^R/\Omega_R}{N_+^L/\Omega_L + N_+^R/\Omega_R} \\
&= \frac{N_-^R/\Omega_R - N_-^L/\Omega_L}{N_-^R/\Omega_R + N_-^L/\Omega_L}\,, \qquad (1.3)
\end{aligned}$$

where $N_{+(-)}^{L(R)}$ is the number of π^0 detected at detector $L(R)$ when the beam polarization is vertically up (down). In this case, we don't need to know the relative luminosity to get the asymmetry because the luminosities cancel out.

Furthermore, we can form a "cross-ratio" asymmetry in which Ω_L and Ω_R can be explicitly canceled out as well. To see this, let's rewrite Equation (1.3) as:

$$\begin{aligned}
N_+^L/\Omega_L &= \frac{1+\epsilon}{2}B \\
N_+^R/\Omega_R &= \frac{1-\epsilon}{2}B \\
N_-^R/\Omega_R &= \frac{1+\epsilon}{2}C \\
N_-^L/\Omega_L &= \frac{1-\epsilon}{2}C\,, \qquad (1.4)
\end{aligned}$$

where $B = N_+^L/\Omega_L + N_+^R/\Omega_R$ and $C = N_-^R/\Omega_R + N_-^L/\Omega_L$. Now consider the asymmetry between the "cross-ratios" $\sqrt{N_+^L N_-^R} = \frac{1+\epsilon}{2}\sqrt{BC\Omega_L\Omega_R}$ and $\sqrt{N_-^L N_+^R} = \frac{1-\epsilon}{2}\sqrt{BC\Omega_L\Omega_R}$. The cross-ratio is defined as:

$$\begin{aligned} \frac{\sqrt{N_+^L N_-^R} - \sqrt{N_-^L N_+^R}}{\sqrt{N_+^L N_-^R} + \sqrt{N_-^L N_+^R}} &= \frac{\frac{1+\epsilon}{2}\sqrt{BC\Omega_L\Omega_R} - \frac{1-\epsilon}{2}\sqrt{BC\Omega_L\Omega_R}}{\frac{1+\epsilon}{2}\sqrt{BC\Omega_L\Omega_R} + \frac{1-\epsilon}{2}\sqrt{BC\Omega_L\Omega_R}} \\ &= \epsilon \end{aligned} \tag{1.5}$$

and it is the same asymmetry. In addition, we combine the + and − results and effectively double the statistics compared to the single arm measurement.

In Figure (1.3), we put detectors L and R at positions that are exactly left or right to the incoming polarized proton beam, *i.e.* $\phi = 90°$. In fact, ϕ can be any where between -180 and $180°$. It is simply that if parity is conserved (in the standard model, strong and electromagnetic interactions conserve parity, while parity conversation is violated only in weak interaction), we expect the largest possible single spin asymmetries at $\phi = \pm 90°$ and zero asymmetries at $\phi = 0°$ or $\phi = 180°$. We can see this from the following argument.

First, let's redefine the transverse single spin asymmetry as (Figure 1.4):

$$\epsilon(\phi) = \frac{\mathrm{d}\sigma(\boldsymbol{S}, \boldsymbol{R_1}) - \mathrm{d}\sigma(-\boldsymbol{S}, \boldsymbol{R_1})}{\mathrm{d}\sigma(\boldsymbol{S}, \boldsymbol{R_1}) + \mathrm{d}\sigma(-\boldsymbol{S}, \boldsymbol{R_1})} = \frac{\mathrm{d}\sigma(\boldsymbol{S}, \boldsymbol{R_1}) - \mathrm{d}\sigma(\boldsymbol{S}, \boldsymbol{R_3})}{\mathrm{d}\sigma(\boldsymbol{S}, \boldsymbol{R_1}) + \mathrm{d}\sigma(\boldsymbol{S}, \boldsymbol{R_3})}, \tag{1.6}$$

where $\mathrm{d}\sigma(\boldsymbol{S}, \boldsymbol{R_1})$ is the differential cross-section of detecting a π^0 from incoming proton with spin $\boldsymbol{S}$ at detector position $\boldsymbol{R_1}$, and ϕ is the clockwise angle from $\boldsymbol{S}$ to $\boldsymbol{R_1}$. In the second expression of Equation (1.6) we use the rotation invariance $\mathrm{d}\sigma(-\boldsymbol{S}, \boldsymbol{R_1}) = \mathrm{d}\sigma(\boldsymbol{S}, \boldsymbol{R_3})$.

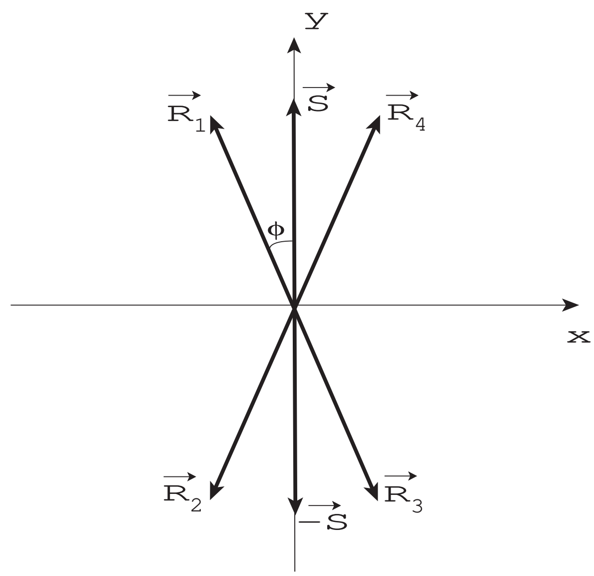

Figure 1.4: Single spin asymmetry measurement (generic ϕ).

Let's consider the parity transformation P: $(\boldsymbol{x} \to -\boldsymbol{x}, \boldsymbol{y} \to \boldsymbol{y}, \boldsymbol{z} \to \boldsymbol{z})$ on $\boldsymbol{S}$ and $\boldsymbol{R_1}$. Remember that spin $\boldsymbol{S}$ transforms like angular momentum $\boldsymbol{l} = \boldsymbol{p} \times \boldsymbol{r}$, we obtains the following after a little algebra,

$$P\boldsymbol{R_1} = \boldsymbol{R_4}\,, \tag{1.7a}$$

$$P\boldsymbol{S} = -\boldsymbol{S}\,. \tag{1.7b}$$

Therefore, if we assume parity invariant (of cross section $\mathrm{d}\sigma$), (and using rotational invariance)

$$\mathrm{d}\sigma(\boldsymbol{S}, \boldsymbol{R_1}) = \mathrm{d}\sigma(-\boldsymbol{S}, \boldsymbol{R_4}) = \mathrm{d}\sigma(\boldsymbol{S}, \boldsymbol{R_2}) = \mathrm{d}\sigma(-\boldsymbol{S}, \boldsymbol{R_3})\,, \tag{1.8a}$$

$$\mathrm{d}\sigma(\boldsymbol{S}, \boldsymbol{R_4}) = \mathrm{d}\sigma(-\boldsymbol{S}, \boldsymbol{R_1}) = \mathrm{d}\sigma(\boldsymbol{S}, \boldsymbol{R_3}) = \mathrm{d}\sigma(-\boldsymbol{S}, \boldsymbol{R_2})\,. \tag{1.8b}$$

From Equations (1.6) and (1.8),

$$\begin{aligned}\epsilon(-\phi) &= \frac{\mathrm{d}\sigma(\boldsymbol{S},\boldsymbol{R_4}) - \mathrm{d}\sigma(-\boldsymbol{S},\boldsymbol{R_4})}{\mathrm{d}\sigma(\boldsymbol{S},\boldsymbol{R_4}) + \mathrm{d}\sigma(-\boldsymbol{S},\boldsymbol{R_4})} \\ &= \frac{\mathrm{d}\sigma(\boldsymbol{S},\boldsymbol{R_3}) - \mathrm{d}\sigma(\boldsymbol{S},\boldsymbol{R_1})}{\mathrm{d}\sigma(\boldsymbol{S},\boldsymbol{R_3}) + \mathrm{d}\sigma(\boldsymbol{S},\boldsymbol{R_1})} = -\epsilon(\phi)\,. \end{aligned} \tag{1.9}$$

Together with the continuity of $\epsilon(\phi)$, we arrive at the conclusion

$$\epsilon(\phi = 0) = \epsilon(\phi = \pi) = 0\,. \tag{1.10}$$

Similarly,

$$\begin{aligned}\epsilon(\pi-\phi) &= \frac{\mathrm{d}\sigma(\boldsymbol{S},\boldsymbol{R_2}) - \mathrm{d}\sigma(-\boldsymbol{S},\boldsymbol{R_2})}{\mathrm{d}\sigma(\boldsymbol{S},\boldsymbol{R_2}) + \mathrm{d}\sigma(-\boldsymbol{S},\boldsymbol{R_2})} \\ &= \frac{\mathrm{d}\sigma(\boldsymbol{S},\boldsymbol{R_1}) - \mathrm{d}\sigma(\boldsymbol{S},\boldsymbol{R_3})}{\mathrm{d}\sigma(\boldsymbol{S},\boldsymbol{R_1}) + \mathrm{d}\sigma(\boldsymbol{S},\boldsymbol{R_3})} = \epsilon(\phi)\,. \end{aligned} \tag{1.11}$$

Therefore $\phi = \frac{\pi}{2}$ and $\phi = -\frac{\pi}{2}$ are the location of extrema of $\epsilon(\phi)$. If (beyond just the simple symmetry discussion here) we know that $|\epsilon(\phi)|$ has only 2 zero-loci at $\phi = 0$ and $\phi = \pi$, then we can conclude the $|\epsilon(\phi)|$ reaches maximum at $\phi = \frac{\pi}{2}$ and $\phi = -\frac{\pi}{2}$.

1.1.2 Differential Cross Section

Any measurement of asymmetries in a collision experiment is incompletely without also measuring the cross section of the specific reaction in question. Only when an understanding of the cross section is well established can we proceed to discuss the meaning of any observed (or unobserved) asymmetries. This is more so for the inclusive π^0 production measurement in the paper ($\sqrt(s) = 200$ GeV, at large psuedorapidity ($\eta > 3$) region), when the corresponding p_T is of the order of a few GeV.

The differential cross section for two-initial-state collision is given by Equation (3.4.15) of [8]. Keep in mind that the invariant phase space volume is $\frac{1}{E}\,\mathrm{d}^3\boldsymbol{p}$ for states on mass-shell ($p^2 + M^2 = 0$). For inclusive measurement (only π^0 is measured), all of the final states except π^0 are integrated. The Lorentz-invariant differential cross-section is thus (Equation 37.38 of [9]) $E\frac{\mathrm{d}^3\sigma}{\mathrm{d}^3\boldsymbol{p}}$. As experimentalists, we count the number of observed π^0, N. N should be proportional to the integrated luminosity for the period of data taking, L. The invariant differential cross-section is

$$E\frac{\mathrm{d}^3\sigma}{\mathrm{d}^3\boldsymbol{p}} = \frac{\mathrm{d}^3\sigma}{d\phi dy p_T dp_T} = \frac{C_{recon}C_{conv}}{f_{\pi^0}}\frac{1}{\hat{\mathfrak{L}}}\frac{N_{\pi^0}}{p_T^*\Delta p_T\Delta\phi\Delta y}\,, \tag{1.12}$$

where y is the rapidity (Equation 1.13); Δy is the rapidity range; $\Delta\phi$ is the azimuthal angle covered by the FPD detector; p_T is the transverse momentum of π^0, and p_T^* is defined as the p_T for which the cross section equals its average over the bin; C_{reco} is a correction for the acceptance, reconstruction efficiency; C_{conv} is a correction for the conversion of decay photons (π^0 to $\gamma\gamma$ branching ratio is $(98.798 \pm 0.032)\%$); f_{π^0} is the trigger bias of the BBC coincidence trigger (the fraction of the inclusive π^0 yield that satisfies the BBC coincidence trigger); and $\hat{\mathfrak{L}}$ is the integrated luminosity for the analyzed data set.

Remember that the definition of rapidity,

$$y = \frac{1}{2}\ln\left(\frac{E+p_z}{E-p_z}\right) = \tanh^{-1}\left(\frac{p_z}{E}\right)\,. \tag{1.13}$$

For $p \gg m$ and $\theta \gg 1/\gamma$, $y \approx \eta$, where eta is the pseudorapidity

$$\eta = -\ln\left(\tan\frac{\theta}{2}\right)\,. \tag{1.14}$$

For (p)FPD, for all practical purpose, $y \approx \eta$.

We should emphasize that it is in its own right very interesting to compare the cross-section measurement of inclusive forward π^0 production at RHIC with next-to-leading order (NLO) pQCD calculation [10].

1.2 Motivation

The underlying theory that governs strong interaction is Quantum Chromodynamics (QCD), one of components of the Standard Model. The elementary particles in QCD are quarks and gluons. Among the striking features of QCD are asymptotic freedom (the coupling of QCD becomes smaller at higher energy scale) and confinement (quarks and gluons are confined inside hadrons). At very high energy, the smallness of QCD coupling means perturbative expansion is a good approximation. At lower energy, the coupling constant of QCD becomes large, thus non-perturbative effects become increasing important and perturbative expansion is not expected to provide a reliable solution. In addition, as a consequence of confinement, what we measure in experiments are hadrons, not quarks or gluons. Quarks and gluons in the final states of the elementary interactions will have to somehow fragment into hadrons, a process inherently non-perturbative. Therefore, according to QCD factorization theorem, what we measure in high energy hadron scattering experiments will be the convolution of parton distribution functions (which describe the constituents (quarks, gluons) of the initial state particles), hard scattering cross sections for elementary pQCD processes, and fragmentation functions (which tell how quarks and gluons fragment into hadrons).

We consider the following process of inclusive hadron production in hadron scattering:

$$A^{\uparrow}(P_A) + B(P_B) \to h(P_h) + X, \tag{1.15}$$

where $A^{\uparrow}$ is the transversely polarized proton, B is the unpolarized proton, X is the collection of unobservable particles from the reaction, and particle h is a π^0 meson.

The hadron-hadron scattering process is schematically shown by (Figure 1.5):

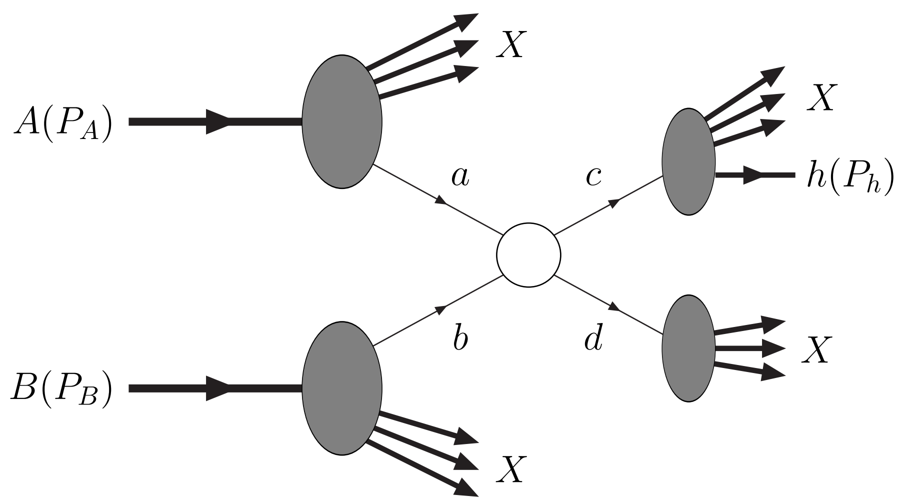

Figure 1.5: Hadron-hadron scattering with inclusive production of a particle h.

The Mandelstam variables are as usual:

$$s = (P_A + P_B)^2 \,, \qquad t = (P_A - P_h)^2 \,, \qquad u = (P_B - P_h)^2 \,, \tag{1.16}$$

and Feynman variable x_F is

$$x_F \equiv \frac{2P_{hL}}{\sqrt{s}} = \frac{t-u}{s} \,. \tag{1.17}$$

According to QCD factorization theorem, the differential cross-section for the reaction (1.15) can be formally written as

$$d\sigma = \sum_{abc} \sum_{\alpha\alpha'\gamma\gamma'} \rho^a_{\alpha\alpha'} f_a(x_a) \otimes f_b(x_b) \otimes d\hat{\sigma}_{\alpha\alpha'\gamma\gamma'} \otimes \mathcal{D}^{\gamma\gamma'}_{h/c}(z) \,. \tag{1.18}$$

Here f_a (f_b) is the distribution function of parton a (b) inside the hadron A (B), $\rho^a_{\alpha\alpha'}$ is the spin density matrix of parton a, $\mathcal{D}^{\gamma\gamma'}_{h/c}(z)$ is the fragmentation matrix of parton c into hadron h, and $d\hat{\sigma}/d\hat{t}$ is the partonic cross-section:

$$\left(\frac{d\hat{\sigma}}{d\hat{t}}\right)_{\alpha\alpha'\gamma\gamma'} = \frac{1}{16\pi\hat{s}^2} \frac{1}{2} \sum_{\beta\delta} \mathcal{M}_{\alpha\beta\gamma\delta} \mathcal{M}^*_{\alpha'\beta\gamma'\delta}, \tag{1.19}$$

where $M_{\alpha\beta\gamma\delta}$ is the scattering amplitude of the elementary partonic process

$$a(k_a) + b(k_b) \to c(k_c) + d(k_d). \tag{1.20}$$

and $\hat{s}$ and $\hat{t}$ are partonic Mandelstam invariants. (see Figure 1.6).

If the produced hadron h is unpolarized, or spinless, we would expect in the collinear case that matrix $\mathcal{D}^{\gamma\gamma'}_{h/c}$ is diagonal, *i.e.*, $\mathcal{D}^{\gamma\gamma'}_{h/c} = \delta_{\gamma\gamma'}\, \mathcal{D}_{h/c}$, where

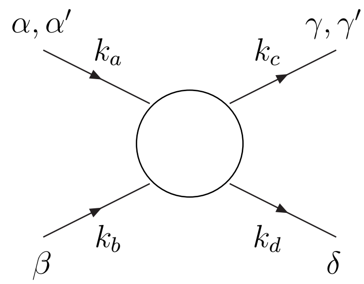

Figure 1.6: Elementary parton-parton scattering processes.

$\mathcal{D}_{h/c}$ is the unpolarized fragmentation function (see Subsection 1.4.3). Combined with helicity conservation in the partonic subprocess ($\alpha + \beta = \gamma + \delta$ and $\alpha' + \beta = \gamma' + \delta$), we would then arrive at $\alpha = \alpha'$. Therefore, in (1.19) there is no dependence on the spin of hadron A in the leading twist (leading order pQCD and collinear case) of pQCD and all single-spin asymmetries are zero at leading twist. Higher twist terms would be suppressed (such as by the mass of quark, $\frac{m_q}{p_T}\alpha_s \ll 1$), and single-spin asymmetry for inclusive π production in polarized p-p collision was thus expected to be small. However, we know from experiments that there is large non-zero single-spin asymmetry A_N at large x_F.

To summarize, it is necessary to look beyond the collinear terms at leading twist.

1.3 Single Spin Asymmetries in $p_\uparrow + p \rightarrow \pi^0 + X$

Remember that Equation (1.18) is for the collinear case and leading twist. To get non-zero single-spin asymmetries, we may either take into account the transverse motion of quarks inside hadrons (either the initial states or the final states), or consider higher twist terms. The following 3 models have been proposed:

1. Collins effect [11]: Intrinsic transverse momentum $\boldsymbol{\kappa}_T$ of hadron h (π^0) relative to the fragmenting quark opens up the possibility that $\mathcal{D}_{h/c}^{\gamma\gamma'}$ is not necessarily diagonal (owing to T-odd fragmentation functions). This effect also requires a non-zero value for the transversity structure function (also called transversity distribution), which represents the difference in probability to find a quark with its spin up ($\uparrow$) and down ($\downarrow$) inside a transversely polarized proton in the infinite momentum frame (Equation 1.33c).

2. Sivers effect [12]: Intrinsic transverse momentum $\boldsymbol{k}_T$ of quarks inside hadron A requires that $f_a(x_a)$ in (1.18) be replaced by the probability density $\mathcal{P}_a(x_a, \boldsymbol{k}_T)$, which may depend on the spin of hadron A due to T-odd distribution functions (Equation 1.35).

3. Higher twist terms [13–17].

When the intrinsic transverse motion of quarks inside hadrons is taken into account, the quantum chromodynamics (QCD) factorization theorem is not proven. Here we will assume that a factorization formula similar to (1.18) can be written

$$E_h \frac{\mathrm{d}\sigma}{\mathrm{d}^3\boldsymbol{P}_h} = \sum_{abc} \sum_{\alpha\alpha'\beta\beta'\gamma\gamma'} \int \mathrm{d}x_a \int \mathrm{d}x_b \int \mathrm{d}^2\boldsymbol{k}_T \int \mathrm{d}^2\boldsymbol{k}'_T \int \mathrm{d}^2\boldsymbol{\kappa}_T \frac{1}{\pi z} \times \mathcal{P}_a(x_a, \boldsymbol{k}_T)\, \rho^a_{\alpha'\alpha}\, \mathcal{P}_b(x_b, \boldsymbol{k}'_T)\, \rho^b_{\beta'\beta} \left(\frac{\mathrm{d}\hat{\sigma}}{\mathrm{d}\hat{t}}\right)_{\alpha\alpha'\beta\beta'\gamma\gamma'} \mathcal{D}^{\gamma'\gamma}_{h/c}(z, \boldsymbol{\kappa}_T)\,, \quad (1.21)$$

where

$$\left(\frac{\mathrm{d}\hat{\sigma}}{\mathrm{d}\hat{t}}\right)_{\alpha\alpha'\beta\beta'\gamma\gamma'} = \frac{1}{16\pi\hat{s}^2} \sum_{\beta\delta} \mathcal{M}_{\alpha\beta\gamma\delta}\mathcal{M}^*_{\alpha'\beta\gamma'\delta}\,. \quad (1.22)$$

1.3.1 Collins' Effect

Let us first consider the Collins' effect for single-spin asymmetries [11, 18]. Intrinsic transverse motion of the produced hadron h is considered, while the transverse momenta of quarks inside the initial-state hadrons are ignored. Thus Equation (1.21) becomes

$$E_h \frac{\mathrm{d}\sigma}{\mathrm{d}^3\boldsymbol{P}_h} = \sum_{abc} \sum_{\alpha\alpha'\gamma\gamma'} \int \mathrm{d}x_a \int \mathrm{d}x_b \int \mathrm{d}^2\boldsymbol{\kappa}_T \frac{1}{\pi z} \times f_a(x_a)\, \rho^a_{\alpha'\alpha}\, f_b(x_b) \left(\frac{\mathrm{d}\hat{\sigma}}{\mathrm{d}\hat{t}}\right)_{\alpha\alpha'\gamma\gamma'} \mathcal{D}^{\gamma'\gamma}_{h/c}(z, \boldsymbol{\kappa}_T)\,, \quad (1.23)$$

and the elementary cross-sections are given by (1.19), with $\boldsymbol{\kappa}_T$ retained. We are interested in transverse spin asymmetries $\mathrm{d}\sigma(\boldsymbol{S}_T) - \mathrm{d}\sigma(-\boldsymbol{S}_T)$. Therefore, since we are neglecting the intrinsic $\boldsymbol{k}_T$ motion of quarks inside A, the spin density matrix elements that contribute to the asymmetry are ρ^a_{+-} and ρ^a_{-+} (off-diagonal terms of s_x and s_y in Equation 1.31), and the contributing elementary cross-sections are $\mathrm{d}\hat{\sigma}_{+-+-} = \mathrm{d}\hat{\sigma}_{-+-+}$ and $\mathrm{d}\hat{\sigma}_{+--+} = \mathrm{d}\hat{\sigma}_{-++-}$.

The asymmetry is

$$
\begin{aligned}
E_h \frac{\mathrm{d}\sigma(\boldsymbol{S}_T)}{\mathrm{d}^3\boldsymbol{P}_h} \quad - \quad E_h \frac{\mathrm{d}\sigma(-\boldsymbol{S}_T)}{\mathrm{d}^3\boldsymbol{P}_h} &= \\
& -2|\boldsymbol{S}_T| \sum_{abc} \int \mathrm{d}x_a \int \mathrm{d}x_b \int \mathrm{d}^2\boldsymbol{\kappa}_T \, \frac{1}{\pi z} \, \Delta_T f_a(x_a) \, f_b(x_b) \\
& \times \left[\left(\frac{\mathrm{d}\hat{\sigma}}{\mathrm{d}\hat{t}} \right)_{+-+-} \sin(\phi_\kappa + \phi_S) + \left(\frac{\mathrm{d}\hat{\sigma}}{\mathrm{d}\hat{t}} \right)_{+--+} \sin(\phi_\kappa - \phi_S) \right] \\
& \times \Delta_T^0 D_{h/c}(z, \boldsymbol{\kappa}_T^2) \,, \qquad (1.24)
\end{aligned}
$$

where ϕ_κ and ϕ_S are the azimuthal angles of $\boldsymbol{\kappa}_T$ and $\boldsymbol{S}_T$, respectively (see Figure 1.4.2), $\Delta_T f_a(x_a)$ is the transversity distribution (Equation 1.33c), and $\Delta_T^0 D_{h/c}$ is the T-odd fragmentation function (Equation 1.39).

In particular, if the spin of hadron A is directed along y ($\phi_S = \frac{\pi}{2}$), Equation (1.24) takes the form[1]

$$
\begin{aligned}
E_h \frac{\mathrm{d}\sigma(\boldsymbol{S}_T)}{\mathrm{d}^3\boldsymbol{P}_h} \quad - \quad E_h \frac{\mathrm{d}\sigma(-\boldsymbol{S}_T)}{\mathrm{d}^3\boldsymbol{P}_h} &= \\
& -2|\boldsymbol{S}_T| \sum_{abc} \int \mathrm{d}x_a \int \frac{\mathrm{d}x_b}{\pi z} \int \mathrm{d}^2\boldsymbol{\kappa}_T \, \cos(\phi_\kappa) \, \Delta_T f_a(x_a) \\
& \times f_b(x_b) \Delta_{TT}\hat{\sigma}(x_a, x_b, \boldsymbol{\kappa}_T) \, \Delta_T^0 D_{h/c}(z, \boldsymbol{\kappa}_T^2) \,, \qquad (1.25)
\end{aligned}
$$

where the elementary double-spin asymmetry $\Delta_{TT}\hat{\sigma}$ is given by

$$
\begin{aligned}
\Delta_{TT}\hat{\sigma} &= \left(\frac{\mathrm{d}\hat{\sigma}}{\mathrm{d}\hat{t}} \right)_{+-+-} - \left(\frac{\mathrm{d}\hat{\sigma}}{\mathrm{d}\hat{t}} \right)_{+--+} \\
&= \frac{\mathrm{d}\hat{\sigma}(a^\uparrow b \to c^\uparrow d)}{\mathrm{d}\hat{t}} - \frac{\mathrm{d}\hat{\sigma}(a^\uparrow b \to c^\downarrow d)}{\mathrm{d}\hat{t}} \,. \qquad (1.26)
\end{aligned}
$$

[1]Original equation in [19] omitted a factor of $\cos(\phi_\kappa)$ in the integrand.

The key to the Collins effect is a non-zero T-odd fragmentation function that arises from intrinsic transverse motion of the fragmented hadron relative to the fragmenting quark.

1.3.2 Sivers' Effect

The Sivers effect [12, 18, 20, 21] relies on T-odd distribution functions. This mechanism predicts a single-spin asymmetry of the form

$$\begin{aligned} E_h \frac{\mathrm{d}\sigma(\boldsymbol{S}_T)}{\mathrm{d}^3\boldsymbol{P}_h} \;-\; E_h \frac{\mathrm{d}\sigma(-\boldsymbol{S}_T)}{\mathrm{d}^3\boldsymbol{P}_h} & \\ = |\boldsymbol{S}_T| \sum_{abc} \int \mathrm{d}x_a \int \frac{\mathrm{d}x_b}{\pi z} \int \mathrm{d}^2\boldsymbol{k}_T \Delta_0^T f_a(x_a, \boldsymbol{k}_T^2)\, f_b(x_b) & \\ \times \frac{\mathrm{d}\hat{\sigma}}{\mathrm{d}\hat{t}}(x_a, x_b, \boldsymbol{k}_T)\, D_{h/c}(z)\,, & \qquad (1.27) \end{aligned}$$

where $\Delta_0^T f$ is the T-odd distribution defined in Equation (1.35).

1.3.3 Higher Twist Effect

Higher twist effects on single spin asymmetry were studied in [13–17].

At twist 3 the cross-section for the reaction (1.15) can be formally written as

$$\begin{aligned} \mathrm{d}\sigma = \sum_{abc} \Big\{ & G_F^a(x_a, y_a) \otimes f_b(x_b) \otimes \mathrm{d}\hat{\sigma} \otimes D_{h/c}(z) \\ & + \Delta_T f_a(x_a) \otimes E_F^b(x_b, y_b) \otimes \mathrm{d}\hat{\sigma}' \otimes D_{h/c}(z) \\ & + \Delta_T f_a(x_a) \otimes f_b(x_b) \otimes \mathrm{d}\hat{\sigma}'' \otimes D_{h/c}^{(3)}(z) \Big\}\,, \qquad (1.28) \end{aligned}$$

where $G_F(x_a, x_b)$ and $E_F(x_a, x_b)$ are related to the quark-gluon correlation functions in Section 1.4.4, $D^{(3)}_{h/c}$ is some twist-three fragmentation function, and $\mathrm{d}\hat{\sigma}$, $\mathrm{d}\hat{\sigma}'$ and $\mathrm{d}\hat{\sigma}''$ are cross-sections of hard partonic subprocesses.

The first line in (1.28), which does not contain the transversity distributions, corresponds to the chirally-even mechanism studied in [15]. The second term in (1.28) is the chirally-odd contribution analyzed in [16]. The elementary cross-sections can be found in the original papers. In practice, it turns out that the transversity-dependent term is negligible. [17]. Thus the first term gives the initial-state twist-3 effect, and the third term the final-state twist-3 effect.

1.4 Theoretical background

Here we present brief definitions for those quantities relevant to the single spin asymmetries in inclusive hadronic production measurement. For a full review, please refer to [19].

1.4.1 Transverse Polarization and Spin Density Matrix

The polarization vector of a spin-$\frac{1}{2}$ particle with momentum $\boldsymbol{P}$ is $s^\mu = (\frac{\lambda|\boldsymbol{P}|}{m}, \frac{P_0\lambda}{m|\boldsymbol{P}|}\boldsymbol{P} + \boldsymbol{s}_\perp)$. In the high-energy limit ($|\boldsymbol{P}| \gg m$, $P_0 = |\boldsymbol{P}| + O(|\boldsymbol{P}|^{-1})$),

$$s^\mu \approx \lambda \frac{p^\mu}{m} + s^\mu_\perp, \tag{1.29}$$

where λ is (twice) the helicity of the (spin-$\frac{1}{2}$) particle and $s^\mu_\perp = (0, \boldsymbol{x}_\perp$.

The spin density matrix for a spin-$\frac{1}{2}$ particle is

$$\rho = \frac{1}{2}\left(1 + \boldsymbol{\sigma}\cdot\boldsymbol{s}\right). \tag{1.30}$$

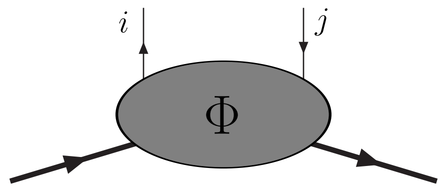

Figure 1.7: The quark-quark correlation matrix Φ.

This matrix provides a general description of the spin structure of a system, that is also valid when the system is not in a pure state. The polarization vector $\boldsymbol{s} = (s_x, s_y, s_z)$ is, in general, such that $\boldsymbol{s}^2 \leq 1$: in particular it is $\boldsymbol{s}^2 = 1$ for pure states, $\boldsymbol{s}^2 < 1$ for mixtures. Explicitly, ρ reads

$$\rho = \frac{1}{2} \begin{pmatrix} 1 + s_z & s_x - \mathrm{i}s_y \\ s_x + \mathrm{i}s_y & 1 - s_z \end{pmatrix} . \tag{1.31}$$

1.4.2 Quark Distribution Functions

Formally, quark distribution functions are light-cone Fourier transformations of connected matrix elements of certain quark field bilinears [22] (See Figure 1.7),

$$\mathrm{Tr}(\Gamma\Phi) = \int \mathrm{d}^4\xi \; \mathrm{e}^{\mathrm{i}k\cdot\xi} \, \langle PS|\bar{\psi}(0)\, \Gamma \, \psi(\xi)|PS\rangle \, , \tag{1.32}$$

where Γ is a Dirac matrix structure. In the basis of Dirac matrices, the matrix have a natural decomposition into terms of different space-time transformation properties.

To build the terms of various space-time transformation properties, we only have the following independent Lorentz 4-vectors: hadron momentum

P^μ, quark momentum k^μ, and polarization vector S^μ. For collinear quark and hadron momenta, k^μ is proportional to P^μ. Thus we have only two independent 4-vectors: P^μ and S^μ. At leading twist (at order $\mathcal{O}(P^+)$), there are three leading-twist functions

$$\begin{aligned} f(x) &= \int \frac{\mathrm{d}\xi^-}{4\pi}\, \mathrm{e}^{\mathrm{i}xP^+\xi^-} \langle PS|\bar{\psi}(0)\gamma^+\psi(0,\xi^-,0_\perp)|PS\rangle \,, && (1.33a) \\ \Delta f(x) &= \int \frac{\mathrm{d}\xi^-}{4\pi}\, \mathrm{e}^{\mathrm{i}xP^+\xi^-} \langle PS|\bar{\psi}(0)\gamma^+\gamma_5\psi(0,\xi^-,0_\perp)|PS\rangle \,, && (1.33b) \\ \Delta_T f(x) &= \int \frac{\mathrm{d}\xi^-}{4\pi}\, \mathrm{e}^{\mathrm{i}xP^+\xi^-} \langle PS|\bar{\psi}(0)\gamma^+\gamma^1\gamma_5\psi(0,\xi^-,0_\perp)|PS\rangle \,. && (1.33c) \end{aligned}$$

$f(x)$ is the probability of finding a quark with longitudinal momentum k^+/P^+ inside the nucleon, regardless of polarization of the quark, while $\Delta f(x)$ is the difference between number density of quarks with helicity $+$ and the number density of quarks with helicity $-$ (when the parent nucleon has helicity $+$). Similarly $\Delta_T f(x)$ represents the number density of quarks with transverse polarization $\uparrow$ minus the number density of quarks with transverse polarization $\downarrow$ (when the parent nucleon has transverse polarization $\uparrow$).

As noted before, sometimes we need to go beyond the collinear case and consider transverse motion of quarks inside nucleons. The quark momentum is now given by

$$k^\mu \simeq xP^\mu + k_\perp^\mu \,, \qquad (1.34)$$

where we have retained $k_\perp^\mu$, which is zeroth order in P^+, and thus suppressed by one power of P^+ with respect to the longitudinal momentum. By introducing $k_\perp^\mu$, at leading twist, we now have the following three independent 4-momenta:

$k_\perp^\mu$, P^μ and the pseudo-vector $s_\perp^\mu$. These vectors are depicted in the plane orthogonal to the momentum $\boldsymbol{P}$ axis of the polarized proton $p_\uparrow$ (Figure 1.4.2). Refer to Figure (1.1) for our choice of the coordinate system.

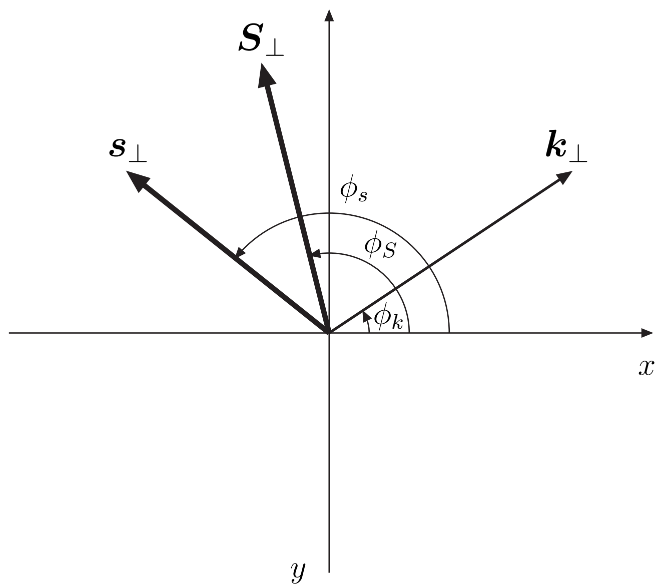

Figure 1.8: Definition of the azimuthal angles.

One of the T-odd distribution function $\Delta_0^T f(x, \boldsymbol{k}_\perp^2)$ that arises in the non-collinear scenario is key to the Sivers' effect:

$$\begin{aligned} \mathcal{P}_{q/N\uparrow}(x, \boldsymbol{k}_\perp) - \mathcal{P}_{q/N\downarrow}(x, \boldsymbol{k}_\perp) &= \mathcal{P}_{q/N\uparrow}(x, \boldsymbol{k}_\perp) - \mathcal{P}_{q/N\uparrow}(x, -\boldsymbol{k}_\perp) \\ &= \Delta_0^T f(x, \boldsymbol{k}_\perp^2)\, \sin(\phi_k - \phi_S)\,. \end{aligned} \tag{1.35}$$

where $\mathcal{P}_{q/N}(x, \boldsymbol{k}_\perp)$ is the probability of finding a quark with longitudinal momentum fraction x and transverse momentum $\boldsymbol{k}_\perp$, and $\lambda(x, \boldsymbol{k}_\perp)$, $\boldsymbol{s}_\perp(x, \boldsymbol{k}_\perp)$ are the quark helicity and transverse spin densities, respectively. Thus $\Delta_0^T f(x, \boldsymbol{k}_\perp^2)$ is related to the number density of unpolarized quarks in a transversely polarized nucleon.

1.4.3 Fragmentation functions

The quark fragmentation functions are related to traces of the decay matrix Ξ

$$\mathrm{Tr}[\Gamma\,\Xi] = \sum_X \int \mathrm{d}^4\xi\ \mathrm{e}^{\mathrm{i}\kappa\cdot\xi}\,\mathrm{Tr}\langle 0|\psi_i(\xi)|P_h S_h, X\rangle\langle P_h S_h, X|\bar{\psi}_j(0)\,\Gamma|0\rangle\,, \tag{1.36}$$

where Γ is a Dirac matrix.

Similar to parton distribution function, there are three leading-twist fragmentation functions: the unpolarized fragmentation function $D_q(x)$, the longitudinally Polaris ed fragmentation function $\Delta D_q(x)$, and the transversely Polaris ed fragmentation function $\Delta_T D_q(x)$. For example,

$$\begin{aligned} D(z) \quad &= \quad \frac{z}{4}\sum_X \int \frac{\mathrm{d}\xi^+}{2\pi}\ \mathrm{e}^{\mathrm{i}P_h^-\xi^+/z} \\ &\qquad \times \langle 0|\psi(\xi^+, 0, 0_\perp)|P_h S_h, X\rangle\langle P_h S_h, X|\bar{\psi}(0)\gamma^-|0\rangle\,. \end{aligned} \tag{1.37}$$

The normalization of $D(z)$ is such that

$$\sum_h \sum_{S_h} \int \mathrm{d}z\, z\, D(z) = 1\,, \tag{1.38}$$

where $\sum_h$ is a sum over all produced hadrons. Hence, $D(z)$ is the number density of hadrons of type h with longitudinal momentum fraction z in the fragmenting quark.

The T-odd $\boldsymbol{\kappa}_T$-dependent fragmentation function $\Delta_T^0 D(z, \boldsymbol{\kappa}'^2_\perp)$ plays a crucial role in Collins' effect,

$$\mathcal{N}_{h/q\uparrow}(z, \boldsymbol{\kappa}'_T) - \mathcal{N}_{h/q\downarrow}(z, \boldsymbol{\kappa}'_T) = z\Delta_T^0 D(z, \boldsymbol{\kappa}'^2_\perp) \sin(\phi_\kappa - \phi_{s'}) \,, \tag{1.39}$$

where ϕ_κ and $\phi_{s'}$ are the azimuthal angles of the quark momentum and polarization, respectively, defined in a plane perpendicular to $\boldsymbol{P}_h$. The angular factor in Equation (1.39), which is (recall that $\boldsymbol{P}_h$ is directed along $-z$)

$$\sin(\phi_\kappa - \phi_{s'}) = \frac{(\boldsymbol{\kappa} \times \boldsymbol{P}_h)\cdot \boldsymbol{s}'}{|\boldsymbol{\kappa} \times \boldsymbol{P}_h| \, |\boldsymbol{s}'|} \,, \tag{1.40}$$

is related to the so-called Collins angle, the azimuthal angle between the spin vector of the fragmenting quark and the momentum of the produced hadron [11],

$$\Phi_C = \phi_\kappa - \phi_{s'} \,. \tag{1.41}$$

1.4.4 Twist-three distributions

At twist-3 quark distribution function is related to the quark correlation matrix with a gluon insertion (see Figure 1.9)

$$\begin{aligned} \Phi^\mu_{Aij}(k, \tilde{k}, P, S) \;\; = \;\; & \int \mathrm{d}^4\xi \int \mathrm{d}^4 z \; \mathrm{e}^{\mathrm{i}\tilde{k}\cdot\xi} \; \mathrm{e}^{\mathrm{i}(k-\tilde{k})\cdot z} \\ & \times \langle PS|\bar{\phi}_j(0) \, gA^\mu(z) \, \phi_i(\xi)|PS\rangle \,. \end{aligned} \tag{1.42}$$

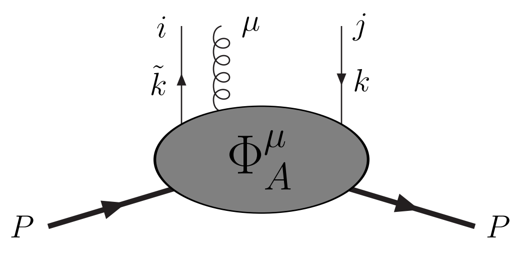

Figure 1.9: The quark-quark-gluon correlation matrix Φ_A^μ.

Chapter 2

Description of Experiment

In high-energy experiments, it is quite usual to write the physics observables as function of azimuthal angle ϕ and pseudo-rapidity η. Remember the definition of η with regard to the zenith angle θ (Equation 1.14), at the forward (large η) region, a detector with relatively small physical dimension could cover a relatively large η region. This is in contrast to mid-rapidity detectors. The Forward Pion Detector (FPD) of STAR is such a forward electromagnetic calorimeter.

In this chapter, we will first describe accelerator facility and polarized proton beam. Then we talk briefly about the detector technologies used in the paper. Although FPD (Forward π^0 Detector) setups for FY02 and FY03 were different, there were many similar components. We will describe the FY02 FPD setup, followed by the FY03 setup. Common components of FY02 and FY03 are put in the section of FY03 FPD.

2.1 Polarized Proton Beam

RHIC (Relativistic Heavy Ion Collider) at Brookhaven National Laboratory is the first polarized proton collider (see Figure 2.1). To accelerate, store and collide positively charged ions, RHIC has two independent storage rings, the Yellow ring (in which the particles go counter-clockwise) and the Blue ring (in which the particles go clockwise). Therefore RHIC is capable of colliding beams of different combinations of species and with the same sign of charges.

The optically pumped polarized ion source (OPPIS) provides the polarized protons, which are accelerated by LINAC and then transferred to the AGS Booster [23]. The polarization of the protons measured at the source can be as high as 70-80%. AGS has its own polarimeter. The polarization measured at AGS generated generally shows reduced proton polarization, at 35% for FY02 and 45% for FY03, at flat-top energy of 24.3 GeV.

The polarization measurement at RHIC injection energy of 24.3 GeV at RHIC polarimeter has a known analyzing power for Column-Nuclear Interference (CNI) reaction, $A_N^{CNI} = 0.0133 \pm 0.0041$ [24, 25]. However, there has been no measurement of A_N^{CNI} at 100 GeV, RHIC flat-top energy for both FY02 and FY03. There are two indirect arguments that suggest A_N^{CNI} at 100 GeV is nearly the same as A_N^{CNI} at 23 GeV.

1. A theoretical model has been made to fit the $|t|$ dependence of A_N^{CNI} at RHIC injection energy. From this model, the $\sqrt{s}$ dependence is found to be small [26, 27].

2. Hal Spinka analyzed ϵ_{CNI} data at RHIC injection energy and 100 GeV and found many occurrences when the measured spin asymmetries were

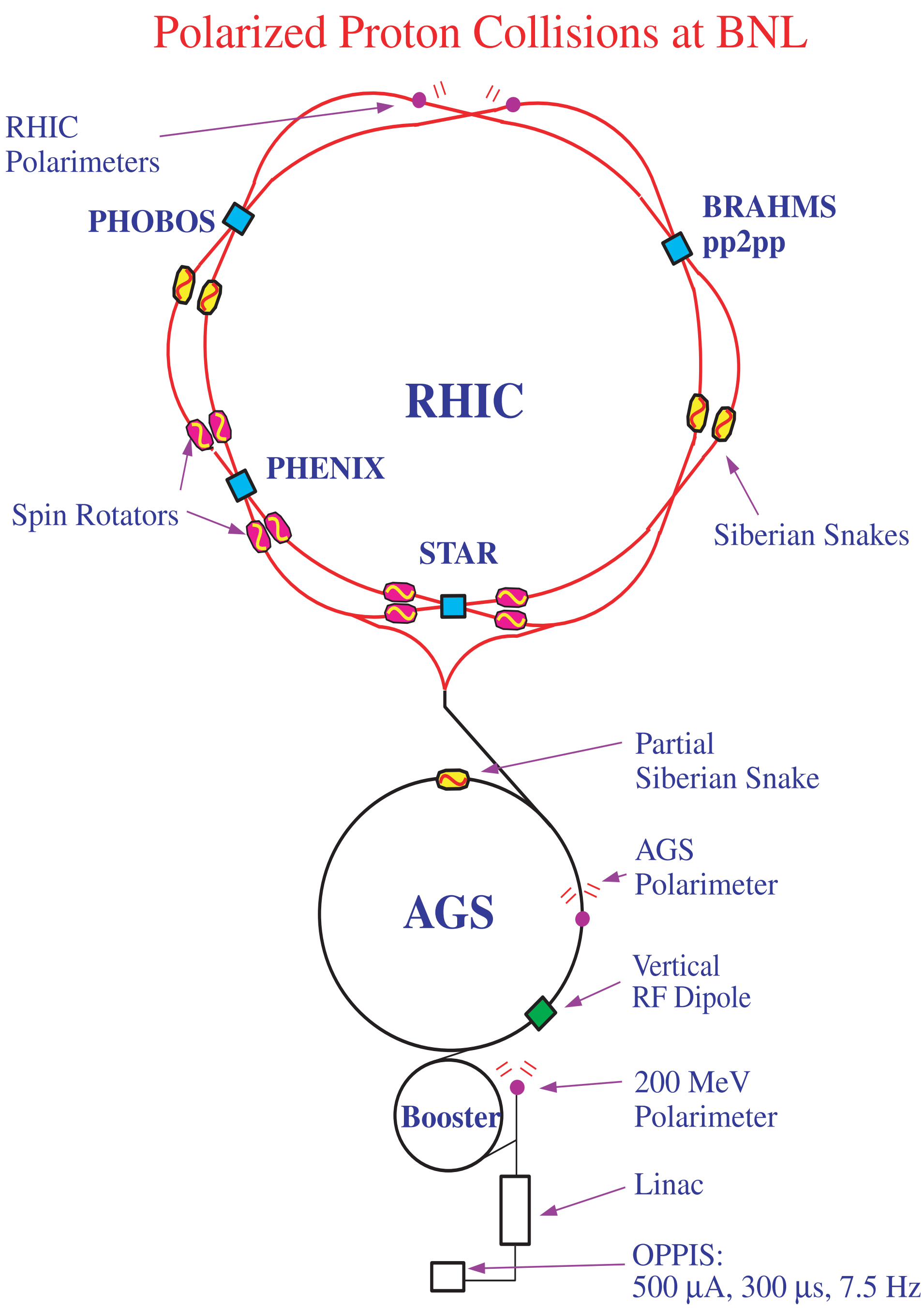

Figure 2.1: RHIC Spin setup.

the same at the two energies. Acceleration of the beam can destroy, but not create, beam polarization. Hence, the analyzing powers at the two energies must be nearly equal.

The measurements we made in run FY02 (and also for FY03) was thus based on the assumption that $A_N^{CNI}(100\text{GeV}) = A_N^{CNI}(24.3\text{GeV})$. Under this assumption, the polarization is thus given by the measured asymmetries ϵ at CNI

$$P_{beam} = \frac{\epsilon}{A_N^{CNI}} \; . \tag{2.1}$$

The average store polarization of protons for run FY02 was 15 % (with peak value of 25%). For FY03, those values were 25% (35%).

Polarization of protons are preserved in RHIC by utilizing, for the first time in a high energy accelerator, full "Siberian Snakes" [6] during the acceleration of protons from RHIC injection energy 24.3 GeV to flat-top energy 100 GeV. For each ring, the two helical dipole magnets ("Siberian Snakes") flip the spin orientation of protons, in attempt to cancel out the depolarization effects of numerous resonances during the acceleration of beam. The stable spin axis of the RHIC rings is vertical.

During a typical store in FY02 and FY03, there were 55 bunches in each ring, resulting to a proton beam bunch crossing at STAR (Solenoidal Tracker At RHIC) every 213 nsec. The average store luminosity for FY02 p-p run was $1.5 \times 10^{30}\text{cm}^{-2}\text{s}^{-1}$, with peak luminosity $2 \times 10^{30}\text{cm}^{-2}\text{s}^{-1}$, and integrated luminosity of $0.5\,(\text{pb})^{-1}$. For FY03 p-p run, average store luminosity was

$3 \times 10^{30}\mathrm{cm}^{-2}\mathrm{s}^{-1}$, peak luminosity $6 \times 10^{30}\mathrm{cm}^{-2}\mathrm{s}^{-1}$, and integrated luminosity of $1.0\,(\mathrm{pb})^{-1}$.

For run FY02, the polarization vector was vertical at STAR IP. For run FY03, a pair of spin rotators were installed on both sides of STAR for each ring. When the rotators were turned on, the spin of protons were rotated from vertical to radial before the beam entered STAR. The spin orientation was further rotated to longitudinal after the beam passed the DX and D0 magnets. After the beam left STAR IP, the reverse process happened, and the spin reverted to the stable vertical direction in the RHIC ring. FY03 p-p run was thus divided into a first period of vertical polarization and a second period of longitudinal polarization. The integrated luminosity for vertical polarization was about $0.5\,(\mathrm{pb})^{-1}$, and about $0.4\,(\mathrm{pb})^{-1}$ for longitudinal polarization.

Let's talk about the spin patterns, *i.e.* the polarization patterns of each beam bunch in a store (for each ring). For FY02 and FY03 p-p runs, the Yellow ring polarization direction was alternated between of up and down for every bunch, while for the Blue ring it was alternated between up and down for every two bunches (See Figure 2.2).

At STAR, which is located at 6 o'clock position of RHIC, the beam pipe is along the east-west direction. The Yellow beam goes from west to east, while the Blue beam goes from east to west.

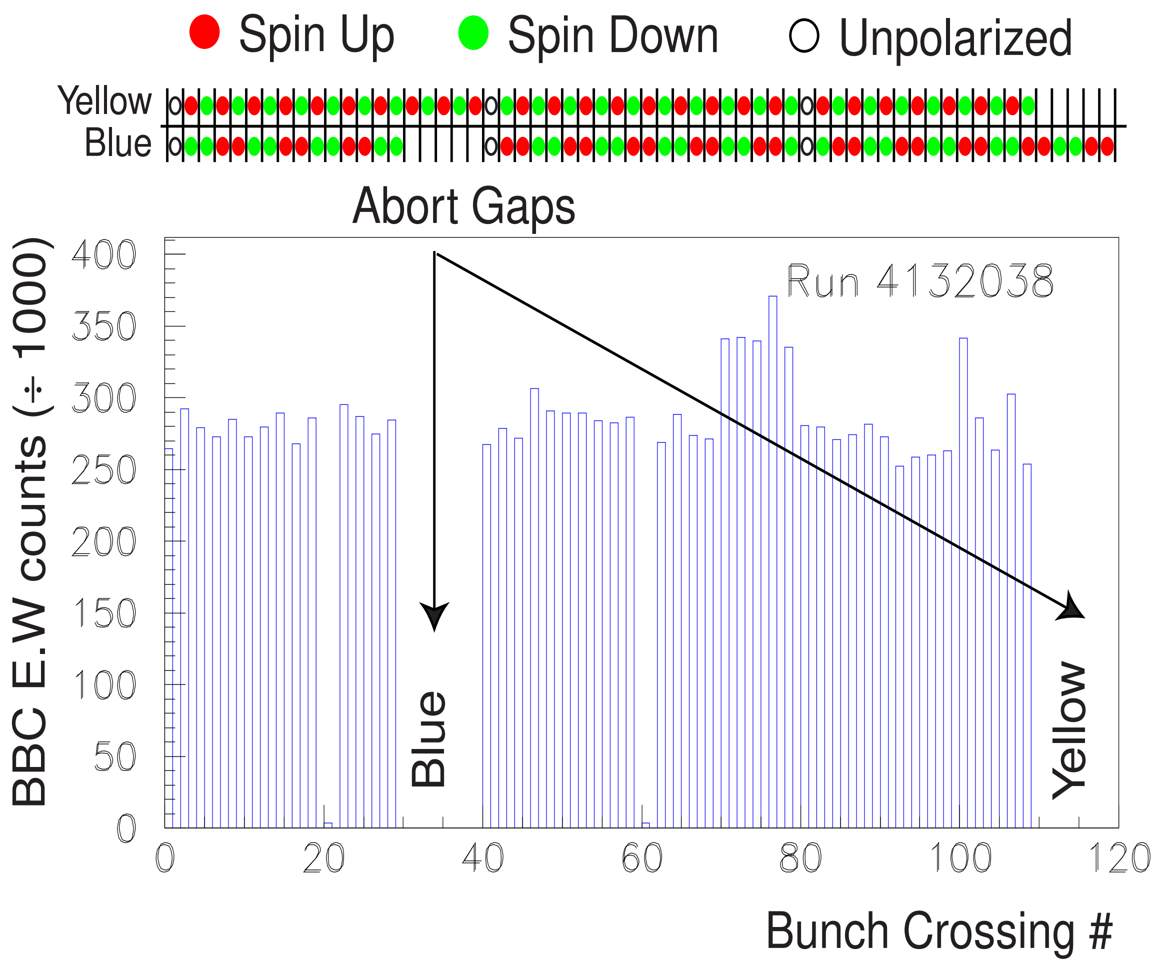

Figure 2.2: Spin Patterns.

2.2 Detector Technologies

Two main types of detector technologies were used in FY02 and FY03 p-p run FPD measurement: Pb-glass and Pb-plastic sampling calorimeter [28]. Pb-glass detectors work by collecting the Cerenkov lights generated by charged particles in an electromagnetic shower [29]. A shower of electrons, positrons, and lower energy photons is generated when a high energy photon (or electron or positron) interacts with the Pb in the detector. The Cerenkov light undergoes total internal reflection at the boundaries of Pb-glass, and is eventually collected and counted at the PMT at the far end of the detector. The Cerenkov cone angle of each individual charged particles is not measured. The number of Cerenkov photons is roughly proportional to the incident energy of EM particle that originated the shower. The Pb-glasses we use in FPD has an index of refraction of 1.67, and negligible optical attenuation. The final counts largely depend on the quantum efficiency of the photo-multiplier-tube (PMT). In general, Pb-glass measures the energy of an EM particle (photon, electron, positron) quite well.

Plastic scintillators are used in scintillator sampling calorimeters (prototype FPD for FY02), shower-maximum detectors (SMD) and STAR Beam-Beam-Counter (BBC). As charged particles pass through the material, atoms in the material are excited. For certain atoms in plastic scintillators, a smaller percentage of the excited energy is released as optical photons. Typically the scintillation process yields about 1 photon per 100 eV of energy deposit. Therefor a minimum-ionizing particle (MIP) generates about 2×10^4 photons going through a 1-cm thick plastic scintillator. The final count of photoelectrons (thus the signal recorded by the electronics) depends on collection and transportation efficiency of the optical fibers and the quantum efficiency of PMTs. The decay times are in ns range, and rise times are much faster. Thus, in the case of BBC, this technology provides fairly good time resolution, and enable BBC to become part of collision trigger of STAR. For SMD and FY02 prototype FPD, the main focus is on sampling the energy of particles that pass through the scintillator, rather than timing resolution.

2.3 FY02 FPD Setup

As we will shown later in the next chapter, detection of π^0 by reconstructing the di-photon invariant mass requires a good measurement of the opening angle between the two photons and the total energy of π^0. The measurement of the relative energy sharing between the photons can be less precise.

From the discussion in the previous chapter, for vertical polarization at STAR IP, we expect the measured A_N to have the largest value for left-right detector(s), and for top-bottom detectors we expect A_N to be zero. The detector setups (for both FY02 and FY03) were designed with this in mind, as we shall see shortly. Left (right) detector(s) would give us a better chance of measuring A_N, while top (bottom) detectors would provide a systematic check.

For run FY02, a prototype End-cap Electro-Magnetic Calorimeter (pEEMC) was used as a prototype FPD, installed on STAR east tunnel platform extension and to the left side of incoming polarized proton beam (in Figure (2.3) pEEMC was marked as North module). It was a lead/plastic scintillator sampling calorimeter, including also a plastic scintillator strip Shower-Maximum-Detector (SMD). To study possible systematics for the A_N measurement, three 4×4 array of Pb-glass detectors were placed to the right side (South module), top (Top module), and bottom (Bottom module) of the incoming polarized proton beam (conventionally called Yellow beam of RHIC).

The north module (pEEMC) and south module were at longitudinal distance of ≈ 750 cm from STAR IP (Interaction Point), while top and bottom modules were closer to STAR IP (Figure 2.4).

2.3.1 prototype EEMC

The pEEMC was a traditional Pb sampling calorimeter, similar to an earlier design of STAR end-cap EMC (hence the name pEEMC) [30]. It consisted of 24 layers of 5 mm thick Vulcan lead sheets, interleaved with 24 layers of 4 mm thick Kururay SCSN-81 plastic scintillator sheets. The total material is approximately 20 radiation length. The layers were machined into 12 optically isolated tiles in a 3×4 pattern, and thus formed 12 towers. The collection and transportation of the scintillation light were done using 0.83 mm-diameter wavelength shifting (WLS) fibers inserted into "sigma grooves" machined in the scintillator.

The calorimeter was contained within a light-tight aluminum box of

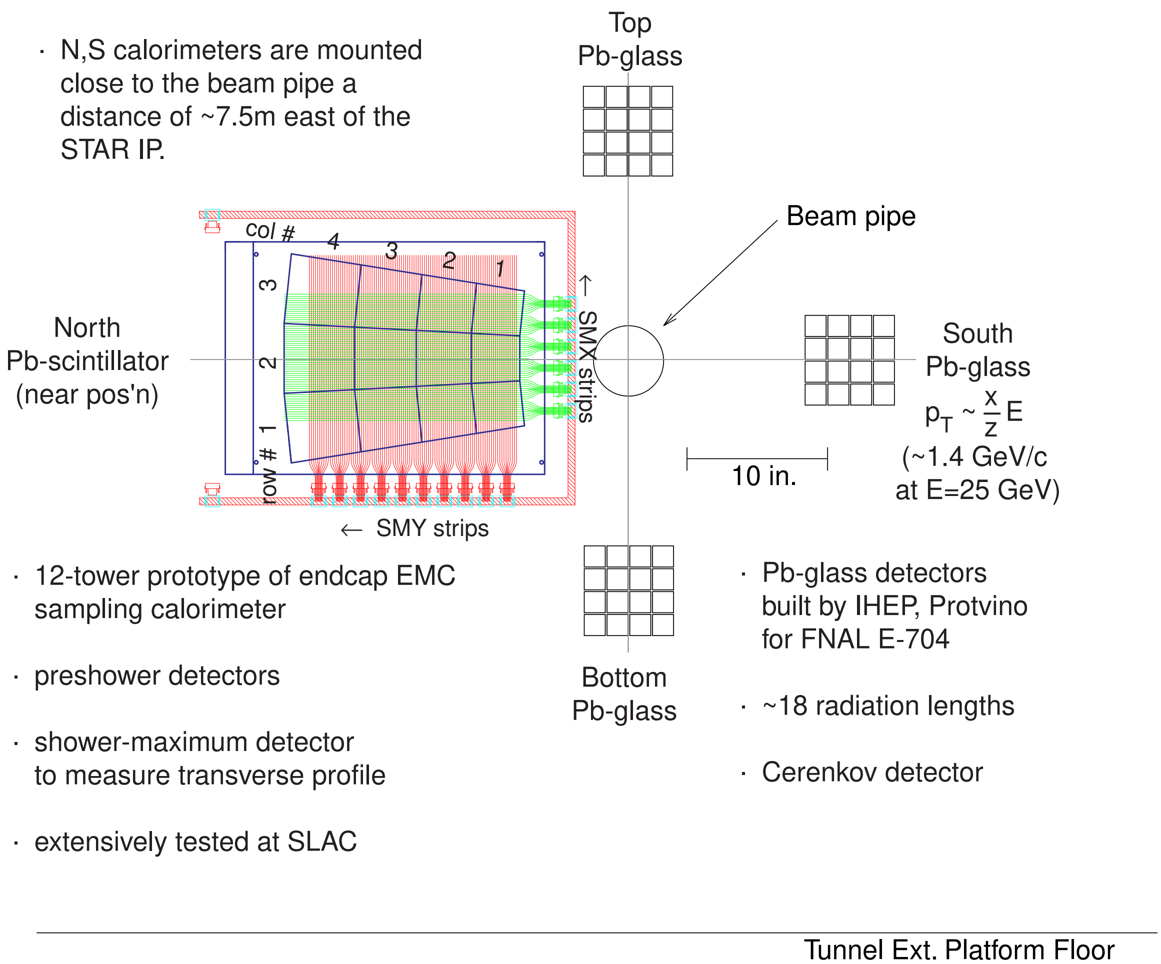

Figure 2.3: FPD Beam View (FY02)

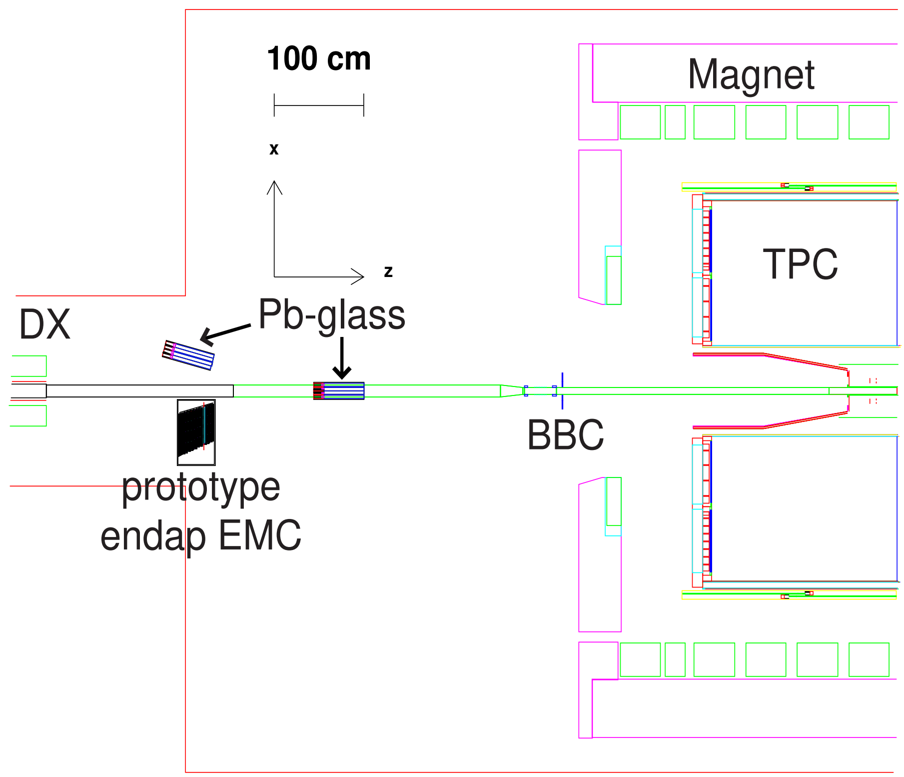

Figure 2.4: Top view of the STAR experiment (FY02)

dimension $15'' \times 21'' \times 28''$ ($l \times w \times h$). Inside the box, the 12 WLS fibers from a single layer were bundled into 2 bundles (6 fibers per bundle). In total, there were $24 \times 12/6 = 48$ bundles. On the side of aluminum box there were 48 10-fiber connector. 0.9 mm-diameter clear fibers connected to the connectors then transported the light to the tower PMT box. Inside the tower PMT box were 12 EMI 9107B PMTs. Scintillation lights from 24 layers of the same tower were summed by routing all 24 fibers onto a lucite light mixer that was viewed by the photo-cathode of a single PMT. Bias voltage was supplied to tower PMT using Cockcroft-Walton bases described later.

2.3.2 prototype SMD

The shower maximum detector (SMD) was just behind the sixth layer of pEEMC (thus about 5 radiation length of pEEMC material in front of it). It was comprised of two orthogonal planes of finely segmented scintillator strips. 60 strips were running horizontally, while 100 strips were running vertically.

The cross-section of strips was an equilateral triangle, with a base width of 7.5 mm and an apex-to-base height of 5 mm. Optical isolation was achieved by wrapping individual triangle with 50 μm of aluminized mylar. Two adjacent strips had their apexes pointing to the opposite direction. Thus, after the strips were glued together, they form a 0.5 cm thick plane (Figure 2.5).

0.83 mm WLS fibers were inserted in holes running axially along the center of each triangle through the complete length of the strip. One end of the fiber was mirrored. The scintillation light from the SMD was transported

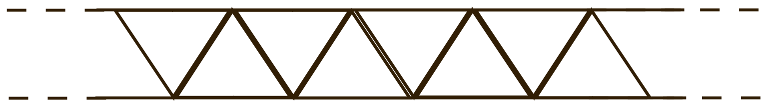

Figure 2.5: cross section of SMD strips.

by WLS fibers from the SMD strips to 16 optical connectors located in the wall of the aluminum box. The length of these WLS fibers was shorter than 0.5 meter. Each optical connector could handle 10 fibers. Thus, 160 0.91 mm-diameter clear fibers were connected one-to-one with 160 WLS fibers from 160 SMD strips. The clear fibers were bundled into 16 groups of 10 fibers per group. The other ends of the clear fibers were connected to multi-anode photomultiplier tubes (MAPMT's). Each MAPMT had 16 pixels. 12 MAPMT's in total were housed in a second box called MAPMT box. Every SMD strip had its own MAPMT pixel. The routing of fibers was arranged to minimize cross-talk between adjacent SMD strips. The bases of the MAPMT's were resistive voltage dividers manufactured by Hamamatsu, and were biased to high voltage of $\approx |900|$ V.

2.3.3 Pb-glass (FY02)

The Pb-glass detectors (including the PMTs and bases) were built by IHEP (Protvino, Russia) for FNAL E704 experiment. For a detailed description of the characteristics of those Pb-glass detector, see [31]. 48 of those Pb-glass detectors were used in FY02. Since we used exactly the same detectors (243 Pb-glass detectors in total) in FY03, and the focus of this paper is on Pb-glass event reconstruction for FY03 p-p run, we will refer to Subsection (2.4.1) on FY03 FPD for more details.

2.3.4 FY02 BBC

BBC consists of 18 small tiles and 18 large tiles of plastic scintillators. For run FY02, the smaller tiles of BBC were all installed. However, only 1/3 of large tiles were built and installed for FY02. Otherwise, the FY02 BBC was almost identical to FY03 BBC (see Subsection 2.4.3).

2.3.5 FY02 Electronics

The racks that housed the FPD electronics was located on the floor directly below the STAR east tunnel platform. For SMD, the anode outputs from each of the 10 MAPMT's were sent through passive delay line chips, and the currents were subsequently carried to a LeCroy 4300B analog-to-digital converter (FERA) over shielded twisted pair cables. SMD signals were not used in trigger decision.

The TDC start was generated by the RHIC clock in coincidence with a FPD trigger. The 12 signals from the 12 tower PMT's were sent over $\approx$ 100ft. of coaxial LEMO cables, thus delayed by $\approx$ 150 ns. The signals were first split by a 50Ω passive splitter. One of these signals was fed into another LeCroy 4300B FERA module, in the same CAMAC crate as the FERA module for SMD, to encode the total charge. The other were fed into a linear fan-in/fan-out (FIFO) module. One of the outputs from this linear FIFO went through a discriminator, and then was delayed by ≈ 200 ns before arriving as the TDC stop signal in a LeCroy 2228A TCD. The other output went to cascading linear FIFO's together with the other tower PMT signals in order to create the sum of tower signals. Four sets of sums were performed, one for the tower PMTs (from pEEMC), the other three from Pb-glass arrays (Top, Bottom, and South).

In the forward region where FPD covered, it is expected that there are large backgrounds besides high energy electromagnetic particles. It was decided that a high energy threshold was set to discriminate against those backgrounds. A programmable value was set, and only events that had a energy deposit that was larger than this value in one of the 4 FPD modules (1 pEEMC and 3 pb-glass arrays) were triggered. Basically, a sum of all tower energy deposits within each module was performed, and then was used as input for FPD trigger electronics.

In Figure (2.6), we show the FPD STAR DAQ (Data AcQuisition system) schematics for FY02.

Note that in FY02, the signals always went to a local FPD DAQ system running on a Linux PC in the STAR control room, as oppose to most of other STAR detector sub-systems whose data streams were integrated with and directly read out by STAR DAQ. Since FPD was a faster detector compared to the mid-rapidity TPC (Time Projection Chamber, with dead time o the order of ≈ 10 msec), FPD was operated in two different modes: with STAR DAQ or stand-alone. In STAR DAQ mode, the runs were controlled STAR RTS (Run

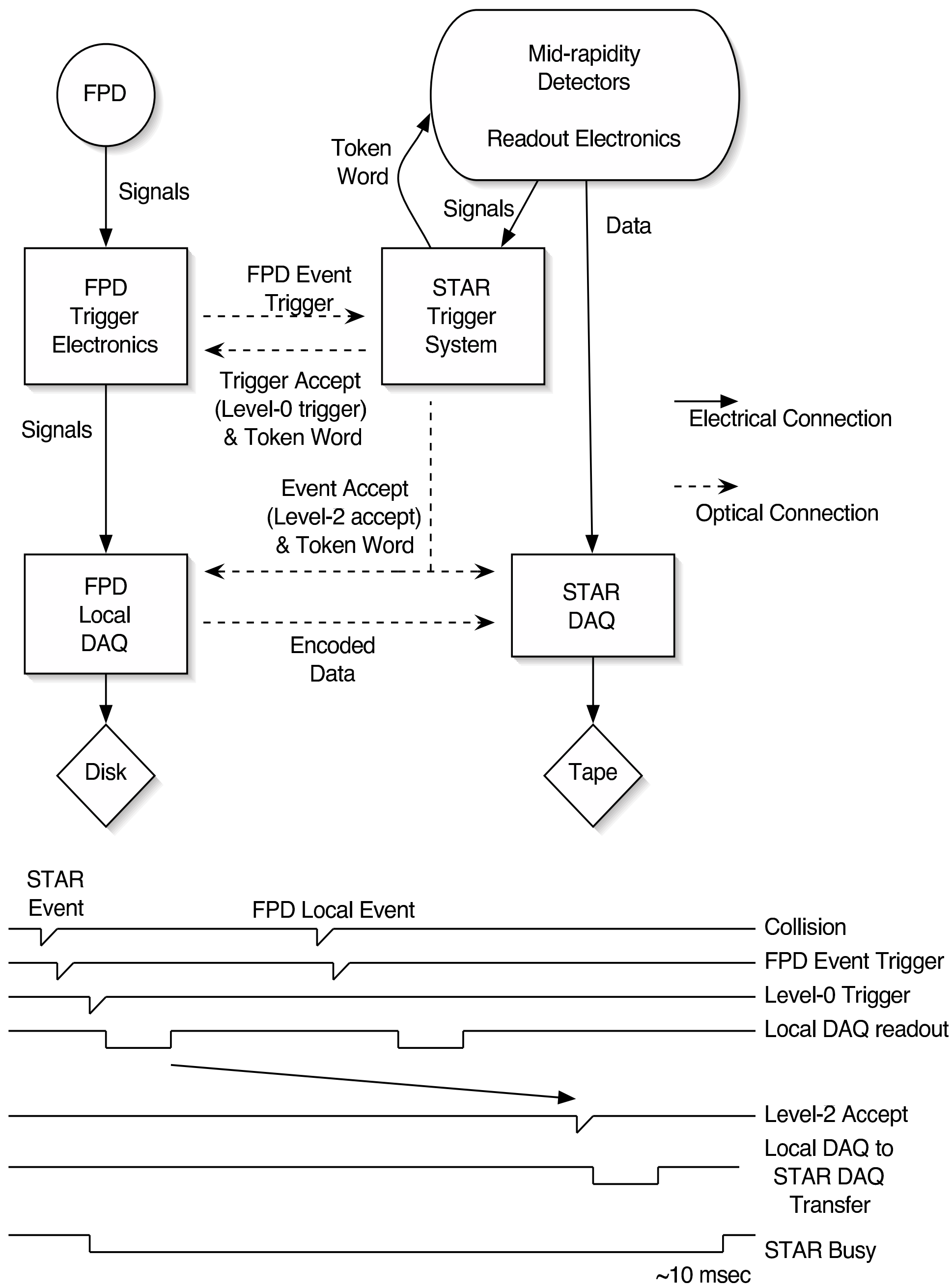

Figure 2.6: FPD STAR DAQ (FY02).

Time System). And when a level 2 accepted was issued, FPD data (including SMD data) were sent as TCP-IP packets to a designated port at STAR DAQ machine through the local network. Every event recorded by STAR was tagged by a 12-bit "token" word. The STAR trigger system broadcasted the "token" word to all of the detector subsystems. This token was embedded in the data header in the packet that was sent to the event builder (EVB). EVB assembled a full event by collecting data from all subsystems. A good event had data packets from all subsystems, each packet having the same token.

In stand-alone mode, FPD operated on its own, and recorded data whenever the thresholds were crossed. In either case, data were written to local disk. Most of data in FY02 were recorded in the stand-alone mode. Note that the stand-alone data were complete for an inclusive cross section and A_N measurement. Checks were made in the analysis of inclusive events recorded locally and inclusive events recorded with STAR. Results of the two analysis agreed.

2.4 FY03 FPD Setup

As we can see from Section (2.3), the FPD setup of FY02 was not left-right symmetric. As discussed in Section (1.1.1), it is advantageous to have a left-right symmetrical setup. Further more, the pEEMC used in FY02 was no longer available for run FY03. The upgraded Forward π^0 Detector (FPD) [32] installed for run FY03 was mainly based on the Pb-glass detectors that were used in FY02 which proved to be a good technology for forward neutral pion detection. Unlike the prototype FPD, the upgraded FPD was installed on both the east and west tunnel platforms in the Wide Angle Hall at the STAR experiment.

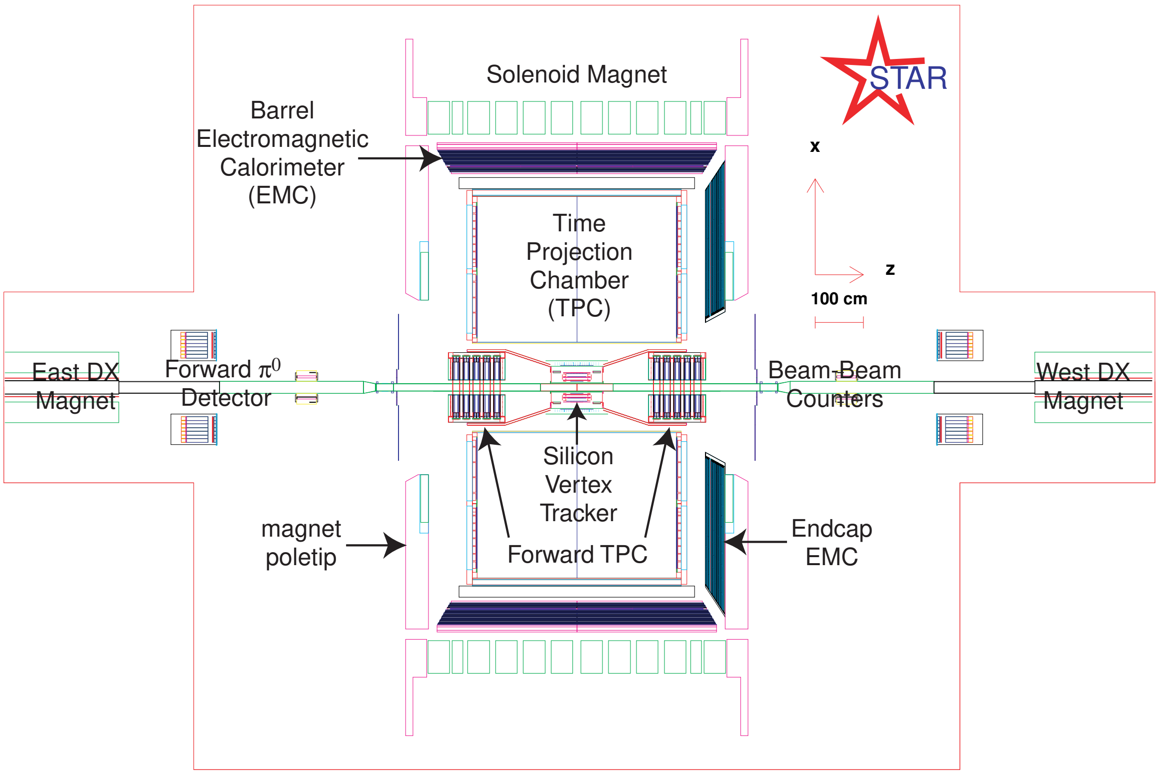

Figure 2.7: Top view of the STAR experiment (FY03)

When it is completely installed, FPD will consist of an East FPD side and West FPD side (with respect to STAR IP). One side has two modules on the right and left side of the beam pipe (called North and South modules by their location), and two modules above and below the beam pipe (called Top and Bottom modules).

The North (or South) module has 7×7 array of Pb-glass detectors as the towers, 7 vertical placed Pb-glass (in front the towers) as pre-shower detectors, and 48 horizontal Shower-Maximum-Detector (SMD) strips per plane between towers and pre-showers. To add more materials in front of SMD for better shower developing, square Pb-sheets of 1.27 cm thickness were also placed just in front of the pre-showers during the p-p run (but not during the dAu run) in FY03. Top and Bottom FPD modules have 25 Pb-glass towers arranged in a 5 matrix (no SMD or pre-shower, or Pb-sheet).

For FY03, we had complete installation of East FPD. For West FPD, only West-South and West-Bottom were installed. Moreover, during FY03 p-p run, there were no electronics for West-South FPD SMD (available electronics were connected to East-North SMD and East-South SMD to form a left-right symmetrical setup). The implication of such arrangement is that we need a Pb-glass only analysis method for West-South (and all Top and Bottom) detectors. An Pb-glass only analysis program will be discussed in the next chapter.

2.4.1 Pb-glass

The dimension of each Pb-glass detector is approximately 45 cm × 3.81 cm × 3.81cm. (The length of 45 cm is equal to 18 radiation length.) Each detector is wrapped by aluminized mylar reflector. For FY02, we made the Pb-glass detectors light-tight by wrapping each detector with black construction paper. For FY03, all detectors were put inside light-tight boxes. The FEU-84

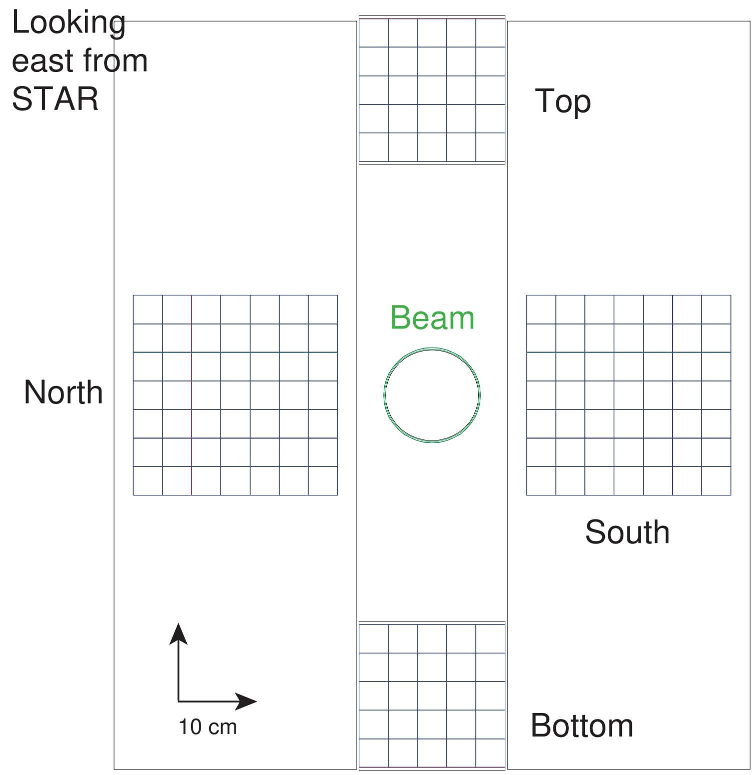

Figure 2.8: Beam view from STAR IP (FY03)

photo-multiplier tubes were connected to the Pb-glass by silicon rubber optical "cookies" for FY02. For FY03, optical grease was used instead for the optical connection of Pb-glass and the PMT. The base has resistive voltage divider, with a total resistance of 9.2 MΩ, that provides the voltage differences to the twelve dynode stages of the FEU-84. The back of base has connections for one high voltage cable and one LEMO signal cable. During FY03 run, the dividers typical operated at voltage about 1600 V. The Pb-glass, PMT's and dividers were taken from old detector array built by IHEP, Protvino group for E704 at Fermi National Accelerator Laboratory. Forty-eight of those Pb-glass detectors were used as part of the prototype FPD for run FY02. A total of 243 Pb-glass detectors were used during run FY03.

2.4.2 FY03 SMD

The FY03 SMD differs from FY02 SMD in several ways. First, both North and South Modules have SMD as part of the detector. Second, there are 48 horizontal strips and 48 vertical strips. And third, the geometry of each strip is different. Again, the cross-section of one strip is equilateral triangle, but apex-to-base height is 0.7 cm and the base width is 1 cm. The length of the strips is 26 cm. Thus, after the 48 strips are glued together, they form a plane roughly 26 cm$\times$ 26 cm in transverse dimension and 0.7 cm in thickness. Remember the Pb-glass towers form an array of 7×7 matrix for North and South modules. The total width of 7 Pb-glass is $7 \times 3.81 = 26.67$ cm. So the horizontal plane and vertical plane of strips effectively cover the cross-section

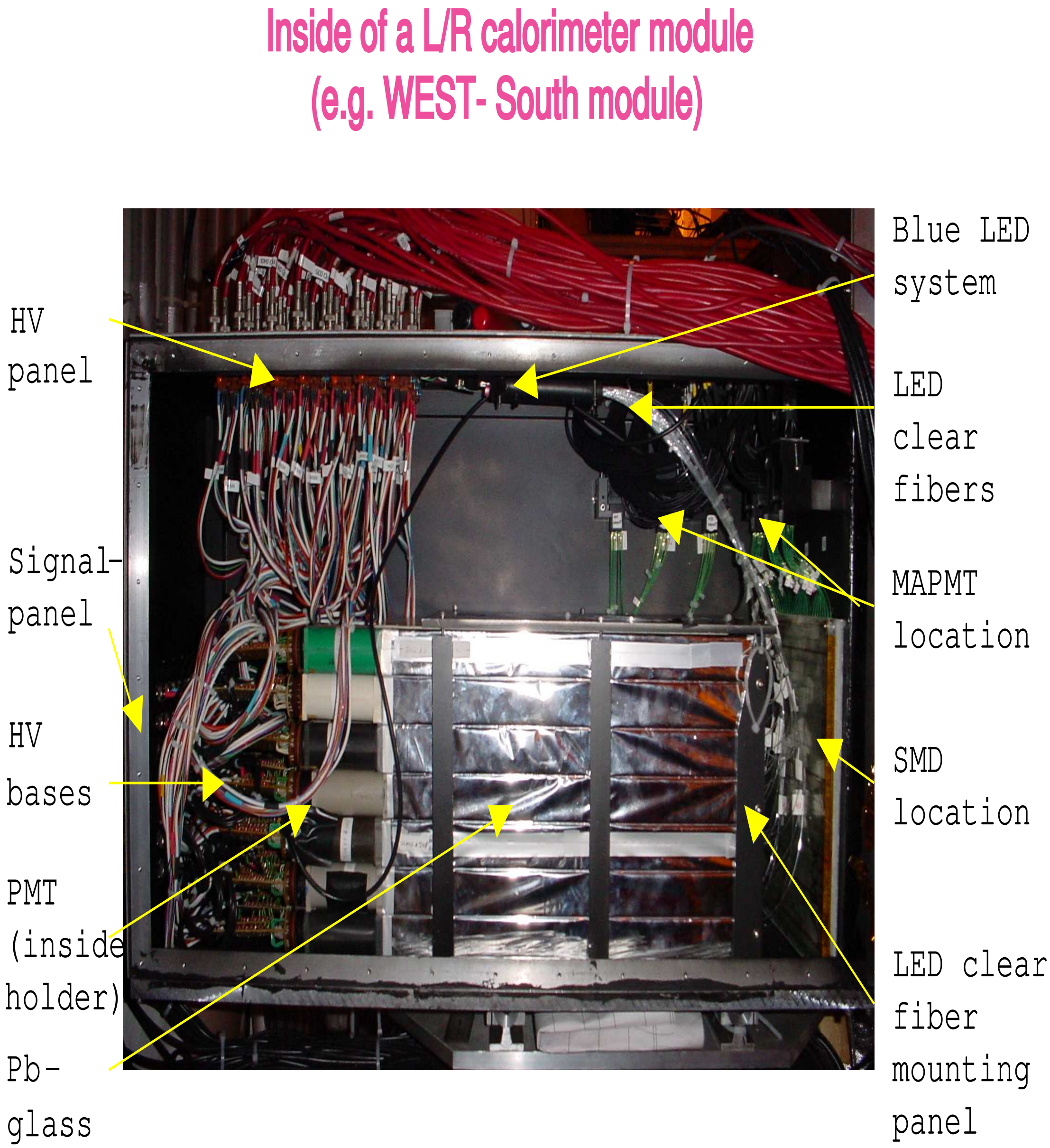

Figure 2.9: FPD West-South.

of Pb-glass towers. The increased depth of SMD (compared with FY02's depth of 0.5 cm) increases the photon counts and thus improves the energy resolution a little bit.

There are around 1 radiation length of material in front FPD. The pre-shower Pb-glass has 1.5 radiation length. Therefore, to improve the effectiveness of SMD, which is most effective when there are around 5 to 6 radiation length of material in front, lead sheet of 1.27 cm thickness (2.3 radiation length) was place in front of the pre-shower Pb-glass detectors for the North or South modules.

Scintillation light from the SMD is again collected and transported by 0.83 mm WLS fibers, just like for FY02 SMD. Since the MAPMTs are inside the same light-tight box that contains the array of Pb-glass detectors and SMD, there is no need for connection to outside clear fibers (as done in FY02 SMD). The MAPMTs are the same Hamamastu H6568, each with 16 pixels.

2.4.3 FY03 BBC

STAR BBC provides a crucial STAR p-p collision trigger. It is also a good local luminosity and polarization detector. FY02 analysis was able to reduce non-collision background to about 1% by requiring coincidence from BBC East and BBC West.

What is shown in Figure (2.10) is the full configuration implemented for run FY03.

BBC is made of 2 sets of 18 small and 18 large hexagonal plastic scin-

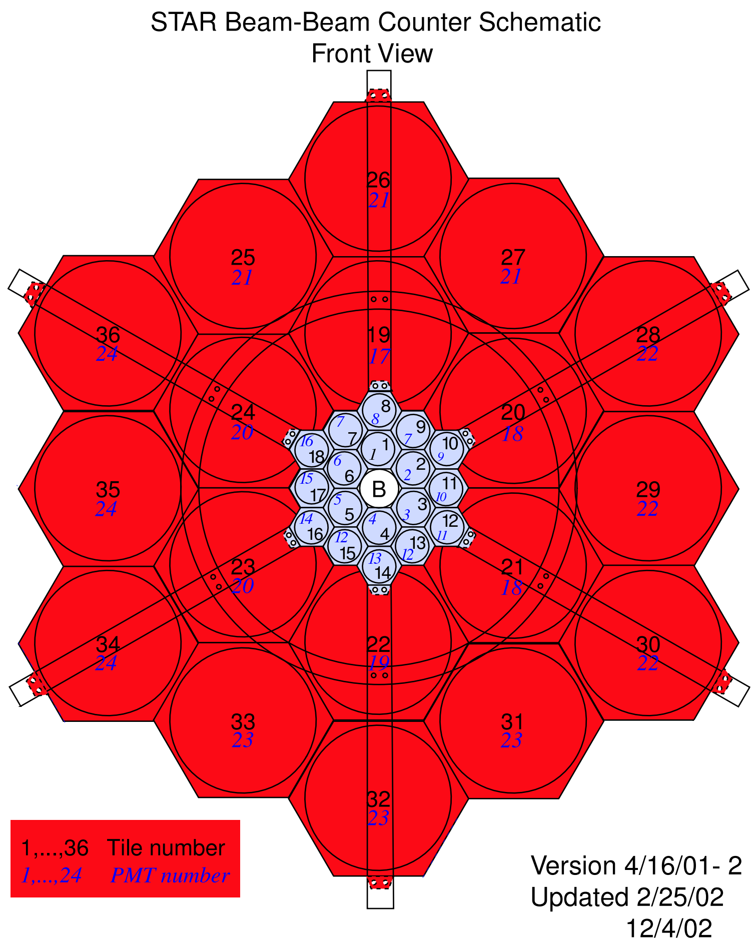

Figure 2.10: BBC configuration for FY03.

tillators. One set is positioned on the STAR east magnetic pole-tip, and the other set on the west pole-tip. The large tiles have 4 times the diameter of the small ones. Both are 1 cm thick. Aluminized mylar sheets are attached to the front and back surfaces of the hexagonal scintillators to serve as mirrors. The edges of the hexagons are optically isolated using MgO_2 paint. WLS fibers inserted in them form a loop and collect the scintillation light. One end of the fiber was polished and mirrored. The other end was polished and glued into optical connections mated to clear fibers for transportation of the scintillation light. Charged particles that travel through the scintillators produce scintillation light, which is then transported to PMT boxes installed on STAR pole-tip above the BBC.

2.4.4 FY03 Electronics

There are both similarities and differences between the FPD electronics for FY02 and FY03 p-p runs. SMD data followed the same path as in FY02. A network connection was still needed from a local FPD Linux machine to STAR DAQ to transmit SMD data when FPD crossed threshold and a level-2 accept was issued for the event. However, the rest of FPD data streams (including signals from pre-shower Pb-glass detectors in front of SMD for North and South modules) were fully integrated with the rest of the STAR system. Trigger logic decisions and data readout used Data Storage and Manipulation (DSM) boards (Figure 2.11). Again, a trigger was issued when sum of signals in any of the 6 FPD modules (4 in East, 2 in West) crossed the threshold. However, there were no longer such things as “FPD local event” (compared with FY02 FPD STAR DAQ schematics (Figure 2.6)). Since FPD was still a faster detector than TPC, there were two modes of STAR DAQ (controlled by STAR RTS): fast detector mode and slow detector mode. In fast detector mode, TPC was taken out of the run. In slow detector mode, TPC was part of the run.

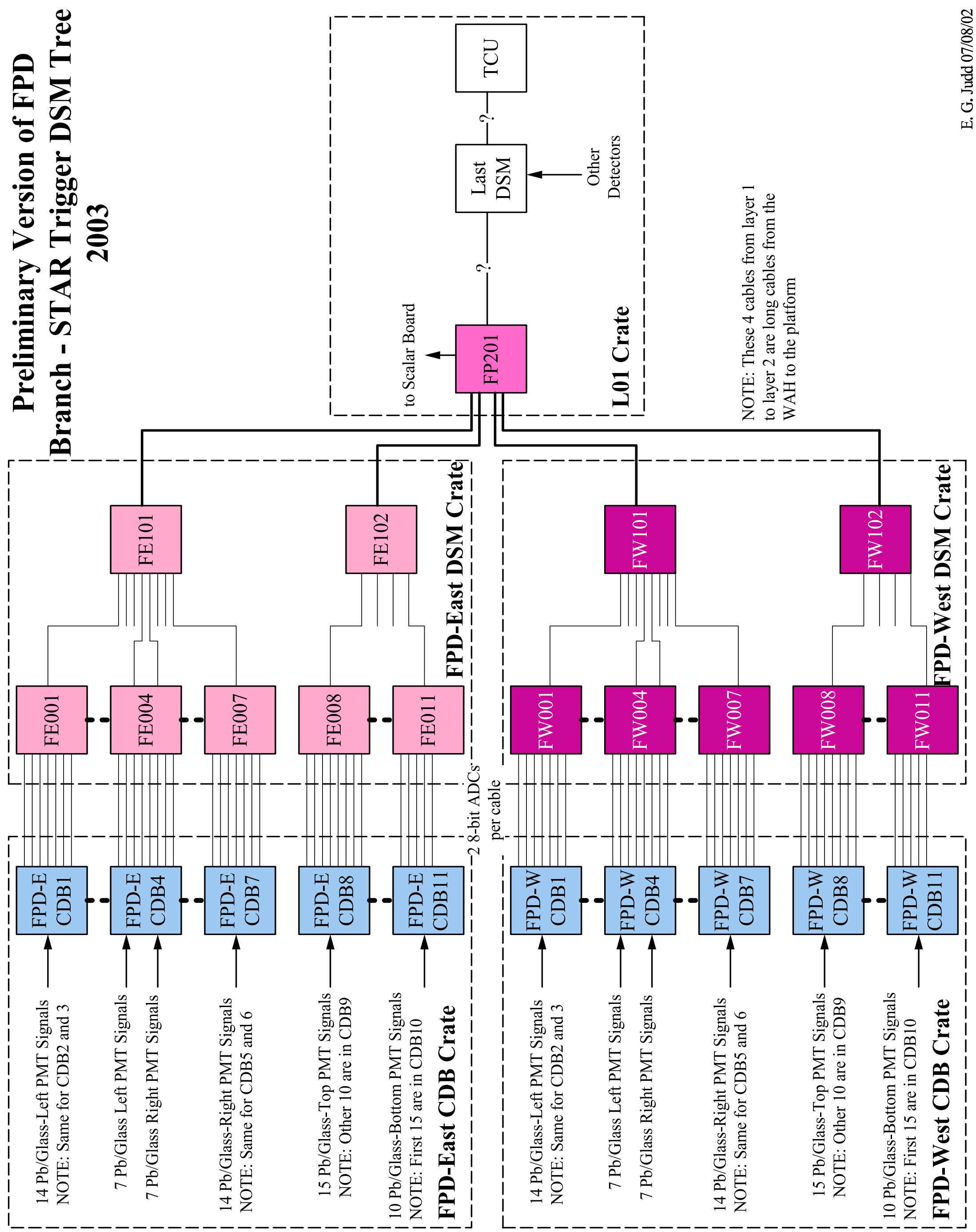

Figure 2.11: FPD DSM tree.

Chapter 3

Analysis Method

3.1 General Analysis Steps

For both FY02 and FY03, analysis of data taken with (prototype)FPD involves the following steps:

1. Pedestal analysis and subtraction of pedestals. In general, detector electronics readouts produce non-zero values (pedestals) even in the absence of beams. It is important to understand the possible time dependence of pedestals (pedestal drift), so that the pedestals can be subtracted from the data in the subsequent analysis. This step could be done in hardware level, as for FY03 Pb-glass detectors (but not for SMD).

2. π^0 event reconstruction. A software program is used to select di-photon events from FPD data and to reconstruct the invariant mass of the possible π^0s.

3. Calibration of detector. Adjust the software gain values of PMTs so the reconstructed π^0 invariant mass has the correct value.

4. Understand possible background correction and efficiency of the reconstruction program.

5. Use the results obtained in the previous steps and π^0 reconstruction program to extract physical observables from recorded data.

3.2 FY02 Analysis Program

π^0 has mean life time $\tau = (8.4 \pm 0.6) \times 10^{-17}$s, correponding to $c\tau = 2.51 \times 10^{-8}$m. Even for high energy π^0 (up to 80 GeV, corresponding to Lorentz boost $\gamma \approx 600$), for practical purpose, we can regard that it decays instantaneously, most likely ($\approx 98.8\%$) to 2 photons.

To reconstruct a π^0 particle, we need to detect both its daughter photons at the detector (pFPD for FY02 and upgraded FPD for FY03). When we observe a di-photon event, we try to evaluate the invariant mass of the photon pair. The formula for the invariant mass reconstruction is:

$$M_{\gamma\gamma} = E_{\gamma\gamma}\sqrt{1 - z_{\gamma\gamma}^2}\sin\left(\frac{\phi_{\gamma\gamma}}{2}\right) \approx E_{\gamma\gamma}\sqrt{1 - z_{\gamma\gamma}^2}\frac{d_{\gamma\gamma}}{2Z_V}\,, \tag{3.1}$$

where $E_{\gamma\gamma}$ is the energy sum of the 2 photons, $\phi_{\gamma\gamma}$ is the angle between the momenta of the 2 photons (which, to a good approximation, is given by the ration of the distance between the 2 photon hits at FPD to the distance from FPD to interaction vertex), and $z_{\gamma\gamma}$ is the so-called energy-sharing factor of photon energies E_1 and E_2,

$$z_{\gamma\gamma} = \frac{|E_1 - E_2|}{|E_1 + E_2|}\,. \tag{3.2}$$

SMD is quite good in determining the positions of photons, and the towers measure the photon energy well. Figure 3.1 illustrates the π^0 event reconstruction for run FY02.

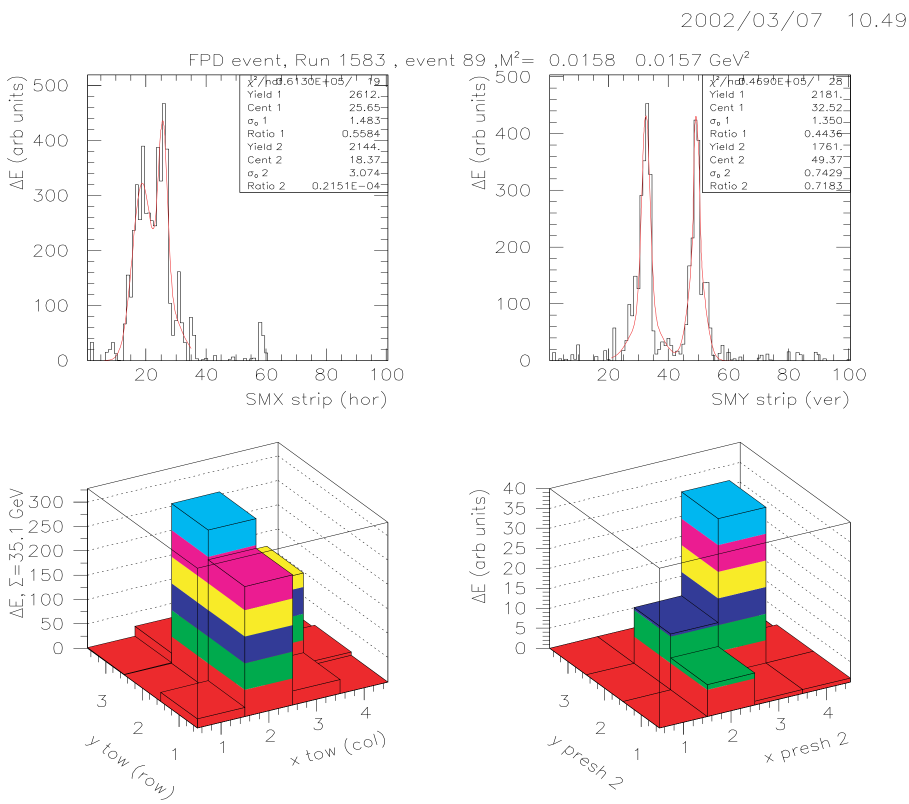

Figure 3.1: neutral Pion reconstruction with SMD, run FY02

In addition, the invariant mass $M_{\gamma\gamma}$ has only a week dependence on $z_{\gamma\gamma}$ when $z_{\gamma\gamma}$ is not close to 1 (for the majority of events that is to say). For FY02 data analysis, we took the areas under the fitted SMD peaks as proportional to the energies of the photons, and calculated $z_{\gamma\gamma}$ as such.

The relative gain factors of SMD strips were determined by matching the exponential slope of spectrum of each strip. The gain factors of towers were adjusted iteratively so that the centroid of the reconstructed invariant mass peak was located at π^0 mass.

3.3 Absolute Luminosity Measurement

Absolute luminosity at STAR was obtained by measuring the transverse size of the colliding beams and the number of protons in each beam. If two bunches containing n_1 and n_2 particles collide with frequency f, the luminosity is

$$\mathcal{L} = f \frac{n_1 n_2}{4\pi\sigma_x\sigma_y}\,, \tag{3.3}$$

where σ_x and σ_y are the Gaussian transverse beam profiles in the horizontal (bend) and vertical directions.

For multiple bunches in each rings, luminosity is obtained by summing all bunch crossing. For spin-sorted luminosity, for example, luminosity sorted by Yellow beam polarization, $\mathcal{L}_{\pm}$ is the sum over bunch crossings with Yellow beam polarization up (+) or down (-).

The circumference of the RHIC rings is 3.834 km. For a certain bunch crossing, $f = \frac{v}{2\pi R} \approx \frac{c}{2\pi R} = 7.825 \times 10^4$Hz. For 60 bunch fills (including 4 bunch abort gap), the time between bunch crossing is $T = 2.13 \times 10^{-7}$s. For 120 bunch fills (including 10 bunch abort gap), the time between bunch crossing is halved.

Number of protons in each bunch is monitored and measured by wall-current monitors, as charged particle beam in the beam pipe creases (mirror) charged current in the beam pipe.

The transverse beam profiles can be measured by STAR beam-beam counter (BBC) during the so-called VanderMeer scan [33]. The cross section measured by BBC can then be determined by $\sigma_{BBC} = \frac{R}{\mathcal{L}}$, where R was the interaction rate observed by BBC, and $\mathcal{L}$ was the luminosity measured by VanderMeer scan. The cross section thus measured by FY02 STAR BBC was 26.1±0.2(stat.)±1.8(sys.) mb, consistent with simulation [34, 35]. The BBC observed 87±8% of the inelastic, non-singly diffractive cross section according to the simulation.

Once the BBC cross section σ_{BBC} was determined, luminosity at STAR could then be determined by measuring the BBC interaction rate R_{BBC}

$$\mathcal{L} = \frac{R_{BBC}}{\sigma_{BBC}} . \tag{3.4}$$

Polarization-sorted luminosity was measured by sorted BBC data by the desired polarization of bunch crossings.

3.4 Background Corrections and Reconstruction Efficiencies

There are two kinds of backgrounds in the data: non-collision background that are mainly beam-gas events, and collision background that are mis-identified events.

Non-collision background is suppressed by BBC coincidence requirement in the analysis. For run FY02, it was suppressed to the level of 1%.

It is expected that the high energy π^0 is accompanied by hadronic jet. Since FPD has about 1 hadronic radiation length of material, there is additional hadronic energy deposit. This will increase the total measured energy in the detector by a certain amount (estimated as 3 GeV in FY02 analysis). For FY03, we use the shower profile fitting method to reconstruct the photons. As the jet will deposit the energy to a larger number of towers, only part of of the jet energy will contribute to the fitting (with respect to the towers within a cluster). Thus it is conceivable that if we use the fitted energy as photon energy, this method might reduce the effect of jet background.

In addition, it is now possible that what we perceive as two photons from a π^0 decay may indeed be one of the daughter photon and something else. Fortunately, the second possibility usually lies at low end of invariant-mass spectrum and can be reduced by $z_{\gamma\gamma}$ cut.

To study the effect of collision background and reconstruction efficiency, a simulation using PYTHIA [34] to model $p+p$ collisions and GEANT [35] to model detector response is developed. Please refer to the section of Chapter 4 on comparison with simulation for a few more details. Background effect can be thus modeled. We can choose to subtract the background in both the simulation and data, or not to do so in either case. Systematic uncertainty with respect to the background can be estimated, including the difference between the background-subtract and non-subtract methods.

To determine the reconstruction efficiency, simulation data will be run against the same analysis program as is used for real data. The efficiencies (ratio of number of reconstructed event vs number of simulated event, both satisfying the same event selection criteria) can written as a matrix of E_π and η. The main factor in efficiency is the geometric acceptance of the detector.

3.5 FY03 Analysis Program

For run FY03, although there are more towers (Pb-glass detectors), the granularity of the Pb-glass is still large enough that, for higher energy π^0, it is still difficult to separate the two photons from π^0 decay, as showed in Figure 3.2.

It is obvious from the above examples that SMDs are very useful to separate merged photons. However, as explained earlier, for p-p run FY03, we did not have electronic readout for West-South SMD. Top or Bottom FPD modules had no SMD in front of them. Therefore, we need a lead-glass-only method of reconstructing π^0 events.

Before we delve into detail, it is important to emphasize the importance of energy calibration of the detector. As we can see from E704 results (Figure 1.1), the analyzing power A_N increases with x_F (therefore E_π), and at the same time the cross-section falls with increasing E_π. If the calibration of the detector were incorrect, mixing of events from wrong energy would then tend to smear out the x_F dependency of the asymmetries.

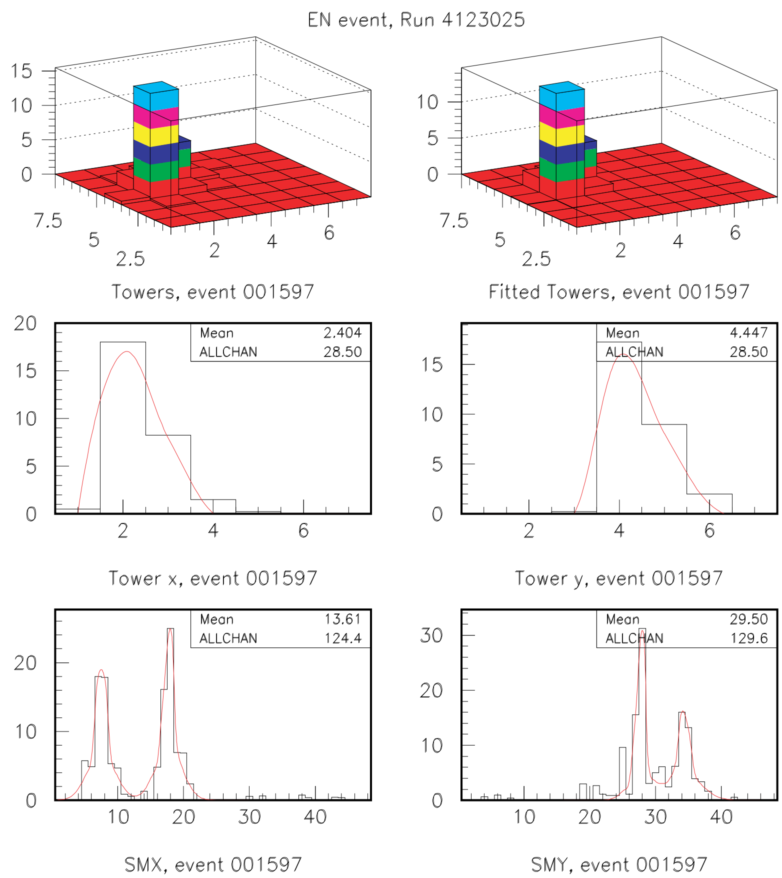

Figure 3.2: neutral Pion reconstruction with SMD, run FY03

Gain factors of SMD strips were determined by matching the spectrum shape of each strip for detector modules with SMD and SMD readout electronics.

3.5.1 Shower Shape

When a high-energy Electromagnetic particle (photon, e^+, e^-) enters the Pb-glass detector, it will trigger an Electromagnetic shower ([29]). Two characteristic quantities of the material govern how the shower is developed in the material, the radiation length X_0, the critical energy for electrons E_c and Moliere radius R_M. For Pb-glass, $X_0 = 2.5$ cm (from now on, when we speak about radiation length, we have in fact converted it to length, usually in unit of cm, by multiplying it with the density of the material), $E_c = 15.8$ MeV, and $R_M = 3.32$ cm.

The final Cerenkov lights are collected in the PMT tube and converted to the signal. As explained earlier, we need to extract both energy and position information of the incoming photons. The idea is then to fit the Pb-glass tower responses (a 2-D array of energy deposit in 7×7 Pb-glass towers) with the profile shape of the Electromagnetic shower.

However, keep in mind that what we measure in Pb-glass towers is not the Electromagnetic shower shape itself, but rather the integral of the shower within the Pb-glass volume. Furthermore, we assume that the longitudinal functional form of the shower is the same regardless of the photon energy, thus we integrate over the length of the Pb-glass detector from now on. The result is a 2-D function, with x and y as the transverse coordinates of photon fit location from the center of the Pb-glass .

In [36], the transverse Electromagnetic Shower shape was modeled by the following functions:

$$G(x,y) = F(x+\frac{d}{2}, y+\frac{d}{2}) - F(x+\frac{d}{2}, y-\frac{d}{2}) - F(x-\frac{d}{2}, y+\frac{d}{2}) + F(x-\frac{d}{2}, y-\frac{d}{2}), \tag{3.5}$$

$$F(x,y) = \frac{1}{2\pi}\sum_{i=1}^{3} a_i \left(\arctan \frac{xy}{b_i\sqrt{b_i^2 + x^2 + y^2}} \right), \tag{3.6}$$

where d is the width of a Pb-glass detector, and the parameters a_i and b_i are:

Table 3.1: Default Shower-shape parameters.

i	1	2	3
a_i	0.8	0.3	-0.1
b_i	0.8	0.2	7.6

Integrating $G(x,y)$ over the entire $x-y$ plane and demanding the result to be 1, we arrive at the condition that $a_1+a_2+a_3 = 1$. The above values above were chosen with this restriction in mind. However, it is somewhat natural to have $a_3 = -0.1$ to be negative, as it resulted in negative value (albeit very small) far away from the center of shower.

Figure 3.3 is 1-D projection of such a profile for a photon which hits right at the exact center of a North or South FPD module. We can see that if the photon hits right at the center of a Pb-glass tower, roughly 80Pb-glass, with the most of rest of the energy deposited at Pb-glass towers right next to high-tower.

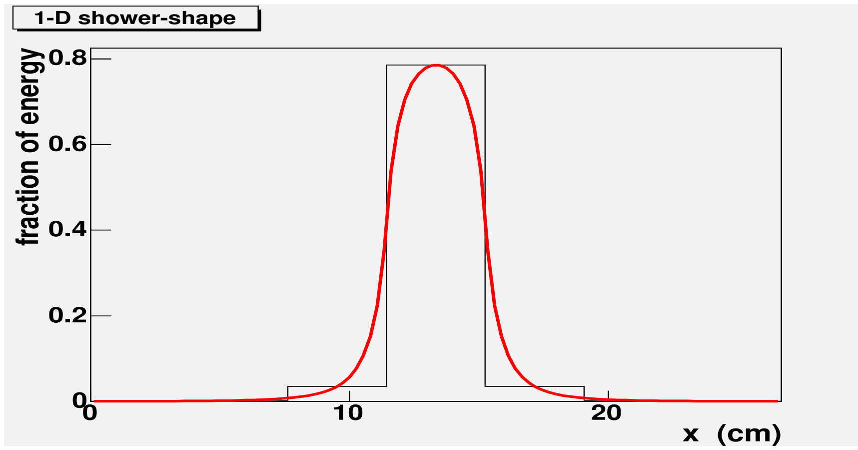

Figure 3.3: 1-D Shower Shape

3.5.2 Clustering and Moment Analysis

Let's take a look at Equation (3.1) again. For a relatively lower energy ($E_\pi < 30$ GeV) π^0, the distance between two photons that are decay products of the same π^0 will be sufficiently large that the responses from the 7×7 lead-glass towers will have two distinct peaks (Figure 3.4). In these cases, we can fit the 2 photons independently. As we can see late in Section (3.5.4), we have a very good handle on the fitting for these type of events.

However, when we go to higher π^0 energy, $d_{\gamma\gamma}$ will become smaller. At sufficiently high π^0 energy (roughly 50-60 GeV), the hits from the two photons will merge (see Figure 3.5). Two questions arise: the first is to figure out whether an event contains 1 or 2 photons; the second is find a good fitting algorithm for 2-photon fit.

We can see when two photons merge, the resultant collection of towers

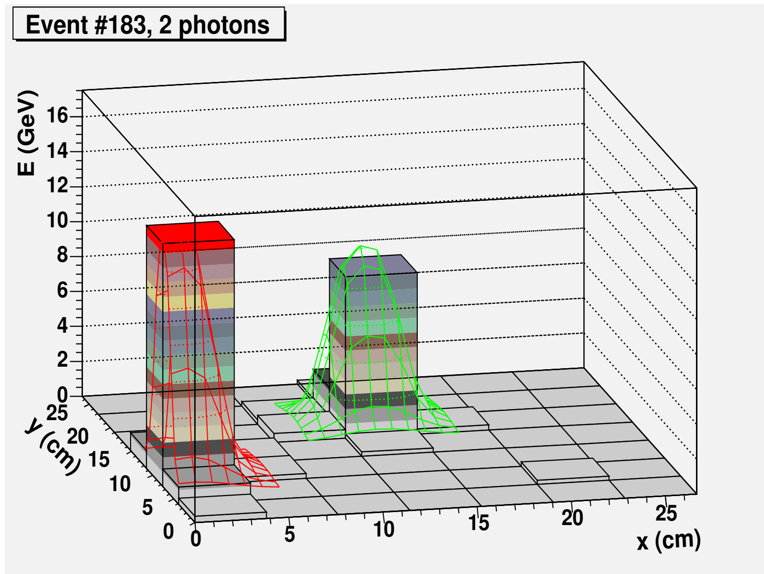

Figure 3.4: Typical lower-energy π^0 event

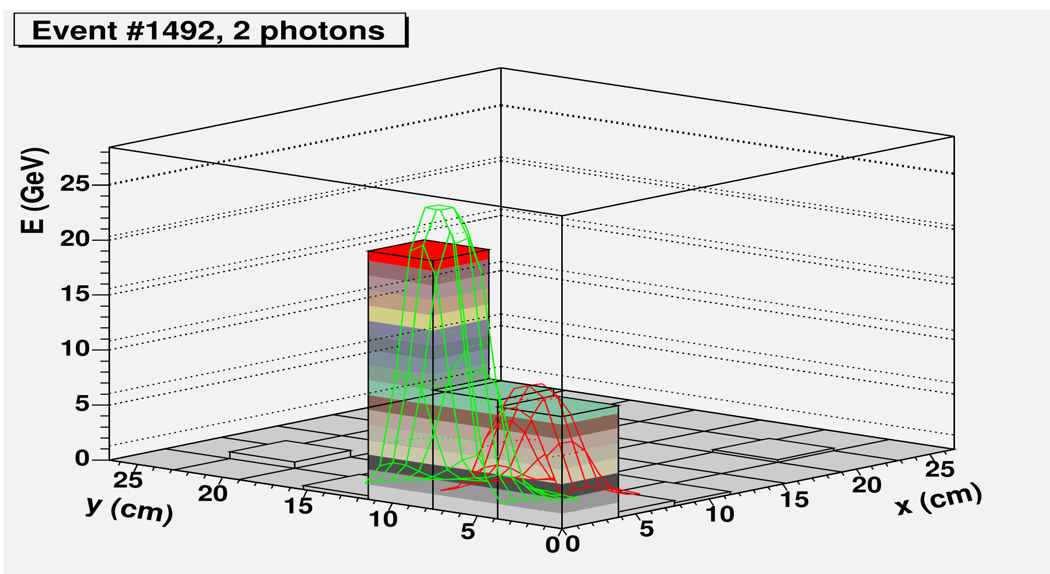

Figure 3.5: Typical higher-energy π^0 event

that have none-zero energy deposit generally has larger number of towers that for a single photon. From this point on, we will call the collection of towers a cluster. Explicitly, a cluster is the collection towers of none-zero energy deposit that are surrounded by zero-energy towers or by the boundary of tower array. The following requirements can be easily translated into a C program.

Definition of a Cluster:

1. A collection of FPD towers within one FPD modules that have none-zero energy deposit in an event.

2. These towers within the collection are next to each other, *i.e.* they are topologically connected in the column-row 2-D lattice space. Two towers are considered next to each other when either they are in the same row and their column number differ by 1, or they are in the same column and their row number differ by 1.

3. Two clusters are separated by zero-energy towers. That is the same as to say that a cluster is bounded by zero-energy towers or the boundary of the FPD module.

4. We require that the sum of energy of towers in the cluster (so-called cluster energy) be greater than 2 GeV. This cut is to separate real photon hits from statistical fluctuation or energy deposited by MIPs. Since later in the analysis a cut on $z_{\gamma\gamma}$ is used, effectively cutting out low energy cluster, this restriction does not impose additional bias in event selection.

The first 2 requirements are quite natural (on the other hand, they do not rule out the possibility of a "hole" inside a cluster). The last requirement is ad hoc. It seems to work quite well for π^0 event analysis. However, it will tend to combine all none-zero towers into one big cluster. If we want to analyze events to have more than 2 photons (like K_s^0, which most likely have 4-photon final decay product), other cluster definition that cut large blocks into smaller ones in a reasonable way might be a better idea.

To write a event reconstruction program, we need a quantitative way of deciding whether a cluster is likely to contains one photon or two (or more) photons. More importantly, we will find out that the size of a cluster that contains two photons from the same π^0 decay is directly related to the π^0 mass. Either way, we start by performing a moment analysis of the cluster.

Let's consider the 2-D plane that is the cross section of one FPD module. To be more specific, let's concentrate on the 7×7 North or South module. The method we describe below is independent of the number of lead-glass array, and can be extended to Top or Bottom modules (5×5 array of lead-glass detectors) straightforward.

The local coordinate system is defined in the Figure (3.6). We simply treat the energy deposit E_i in tower i as if it is deposited right at the center of that tower. We then calculate various moments of such a collection of points, weighted by the energy at various points (the cluster).

The 0th moment is just the sum of energy of the cluster,

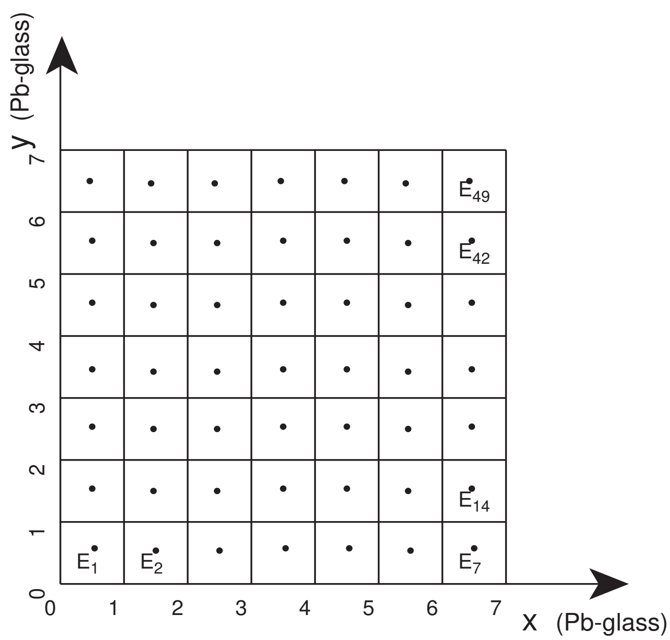

Figure 3.6: Coordinate system of towers.

$$E_c = \sum_i E_i \tag{3.7}$$

The 2 first-moments, one for x and one for y, give the position of the "center of gravity" of the cluster,

$$x_0 = \frac{\sum_i x_i E_i}{\sum_i E_i} = \frac{\sum_i x_i E_i}{E_c} \tag{3.8}$$

$$y_0 = \frac{\sum_i y_i E_i}{\sum_i E_i} = \frac{\sum_i y_i E_i}{E_c} \tag{3.9}$$

The 2nd-moments form a 2×2 matrix. They provide information about the size and orientation of the cluster,

$$M = \begin{pmatrix} \sigma_{xx} & \sigma_{xy} \\ \sigma_{yx} & \sigma_{yy} \end{pmatrix}, \tag{3.10}$$

where,

$$\sigma_{xx} = \frac{\sum_i E_i (x_i - x_0)^2}{\sum_i E_i} = \frac{\sum_i E_i x_i^2}{E_c} - x_0^2, \tag{3.11}$$

$$\sigma_{yy} = \frac{\sum_i E_i (y_i - y_0)^2}{\sum_i E_i} = \frac{\sum_i E_i y_i^2}{E_c} - y_0^2, \tag{3.12}$$

$$\sigma_{xy} = \sigma_{yx} = \frac{\sum_i E_i (x_i - x_0)(y_i - y_0)}{\sum_i E_i} = \frac{\sum_i E_i x_i y_i}{E_c} - x_0 y_0, \tag{3.13}$$

Since M is symmetric (and in addition positive definite), we can alway diagonize it. The two eigenvalues (diagonal elements of the diagonized matrix) are positive definite. We call the larger one σ^2_{max}, and the smaller one σ^2_{min}.

$$\sigma^2_{max} = \frac{(\sigma_{xx} + \sigma_{yy}) + \sqrt{(\sigma_{xx} - \sigma_{yy})^2 + 4\sigma^2_{xy}}}{2}, \tag{3.14}$$

$$\sigma^2_{min} = \frac{(\sigma_{xx} + \sigma_{yy}) - \sqrt{(\sigma_{xx} - \sigma_{yy})^2 + 4\sigma^2_{xy}}}{2}. \tag{3.15}$$

Also, the eigenvector for eigenvalue σ^2_{max} is

$$\begin{aligned} \begin{pmatrix} a \\ b \end{pmatrix} = & \begin{pmatrix} \sigma_{xy} \\ \frac{\sqrt{(\sigma_{xx}-\sigma_{yy})^2+4\sigma^2_{xy}}-(\sigma_{xx}-\sigma_{yy})}{2} \end{pmatrix} \\ & = \begin{pmatrix} \frac{\sqrt{(\sigma_{xx}-\sigma_{yy})^2+4\sigma^2_{xy}}+(\sigma_{xx}-\sigma_{yy})}{2} \\ \sigma_{xy} \end{pmatrix} \end{aligned} \tag{3.16}$$

We are going to use the polar angle (restrict to only in the range of $(-\frac{\pi}{2}, \frac{\pi}{2}]$) of the above eigenvector in the x-y plane,

$$\begin{aligned} \tan\theta = \frac{b}{a} = & \frac{\sqrt{(\sigma_{xx} - \sigma_{yy})^2 + 4\sigma^2_{xy}} - (\sigma_{xx} - \sigma_{yy})}{2\sigma_{xy}} \\ & = \frac{2\sigma_{xy}}{\sqrt{(\sigma_{xx} - \sigma_{yy})^2 + 4\sigma^2_{xy}} + (\sigma_{xx} - \sigma_{yy})} \end{aligned} \tag{3.17}$$

In the special case $\sigma_{xy} = 0$, one of the above expression for the eigenvector is reduce to (0, 0), which does not make sense. In this case, use the other expression which is still meaningful (which gives either $\theta = 0$ or $\theta = \frac{\pi}{2}$).

Now we want to address the question why we want to do the above exercise of clustering and moment analysis, and what is the relationship between the size of the cluster (the σs) and π^0 mass. Basically, we want to know whether a cluster is likely to be the result of a single photon hit or two (or more) photon hits, before we do any fit. The reason is partly because fitting algorithms have their limits. It is difficult just by looking at χ^2/NDF to tell whether it is a reasonable fit. Looking at simulation data, it is not uncommon that a fit of 2 close artificial photons produce a smaller χ^2/NDF for a real 1-photon cluster. The other reason is simply that we can extract a lot of informations about the cluster by moment analysis.

Now imagine one single photon hits one of the FPD module. A Electromagnetic shower is developed. We have the energy deposit for each lead-glass tower. Now imagine two such photons hit the FPD module. Without the other one, each would form a cluster. If we assume that the response of lead-glass detectors is linear, the resultant energy deposit at each tower should be the sum of those from each of the photons. The cluster formed by these 2 photons should then be a superposition of 2 single-photon clusters.

$$E = E_1 + E_2\,, \tag{3.18}$$

$$x = (E_1 x_1 + E_2 x_2)/E\,, \tag{3.19}$$

$$y = (E_1 y_1 + E_2 y_2)/E\,, \tag{3.20}$$

$$E\sigma_x^2 = E_1\sigma_{1x}^2 + E_2\sigma_{2x}^2 + E_1(x_1 - x)^2 + E_2(x_2 - x)^2\,, \tag{3.21}$$

$$E\sigma_y^2 = E_1\sigma_{1y}^2 + E_2\sigma_{2y}^2 + E_1(y_1 - y)^2 + E_2(y_2 - y)^2\,. \tag{3.22}$$

Add the last two equations together, and using the previous 3 equation, we arrive at:

$$\sigma_x^2 + \sigma_y^2 = \frac{E_1(\sigma_{1x}^2 + \sigma_{1y}^2) + E_2(\sigma_{2x}^2 + \sigma_{2y}^2)}{E} + \frac{E_1E_2[(x_1 - x_2)^2 + (y_1 - y_2)^2]}{E^2}\,. \tag{3.23}$$

Remember that $(x_1-x_2)^2+(y_1-y_2)^2 = d_{\gamma\gamma}^2$, $E_1 = \frac{1+z_{\gamma\gamma}}{2}E$, $E_2 = \frac{1-z_{\gamma\gamma}}{2}E$, and call "$\sigma_x^2 + \sigma_y^2$" by a simpler name "$\sigma^2$", we have,

$$E^2\sigma^2 = E(E_1\sigma_1^2 + E_2\sigma_2^2) + \frac{E^2}{4}(1 - z_{\gamma\gamma}^2)d_{\gamma\gamma}^2 \tag{3.24}$$

Compared with equation (3.1), we see that the quantity $E^2\sigma^2$ for a 2-photon cluster is related to the π^0 invariant mass.

Before we end this section, let's finally put out the operational definition of cluster. We found the following definition works quite good for both the simulation and real data, and this will be the one that we use through out this paper.

3.5.3 Categorizing Event

To gain a quantitative understanding of the cluster, we look at simulation of $\pi^0 \to \gamma\gamma$ decay. We plot E_c vs $E_c\sigma_{max}$, for both clusters that contain only one of the photon and clusters that contain both photons. Red points are 1-photon clusters, and blue points are 2-photon clusters.

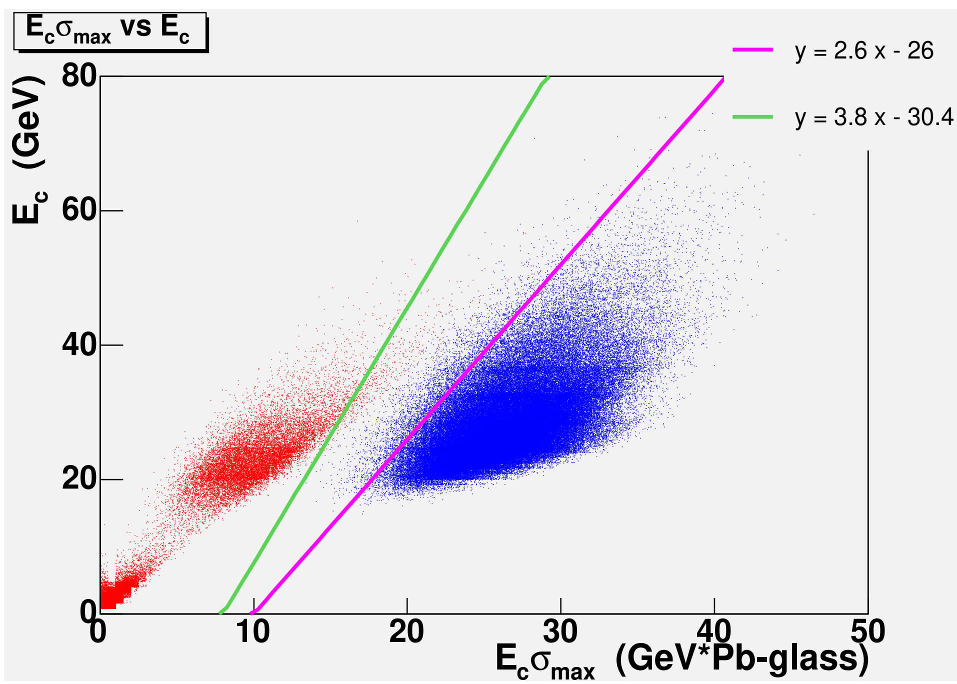

Figure 3.7: Category of clusters: simulation

It is clear that we can largely separate 1-photon or 2-photon clusters. We can thus draw the two colored lines in the above graph, and categorize clusters by their cluster energy and cluster size σ_{max}.

1. Category-1 clusters: Clusters that have small size (relative to the cluster energy) most likely contain only 1 photon.

2. Category-2 clusters: Clusters that have large size (relative to the cluster energy) most likely contain 2 or more photons.

3. Category-0 clusters: Ambiguous clusters that sit in between Category-1 clusters and Category-2 clusters.

Next, let's look at real data. Again, we plot E_c vs $E_c\sigma_{max}$ for all clusters found by our code.

We can still see a gap between clusters that most likely contain just one photon and clusters that most like contain at least two photons. Naturally, there are more ambiguous cases.

3.5.4 1-photon Fit parameterization

For every photon that hits FPD, we need 3 parameters to describe it: x-position, y-position, and energy E. It is quite natural that, for 1-photon fit, we will try to use these 3 parameters. It turns out to be a very good choice. In deed, x_0 of equation (3.8) gives a very good starting point for x-position, and y_0 of equation (3.9) for y-position. The deviation from those starting

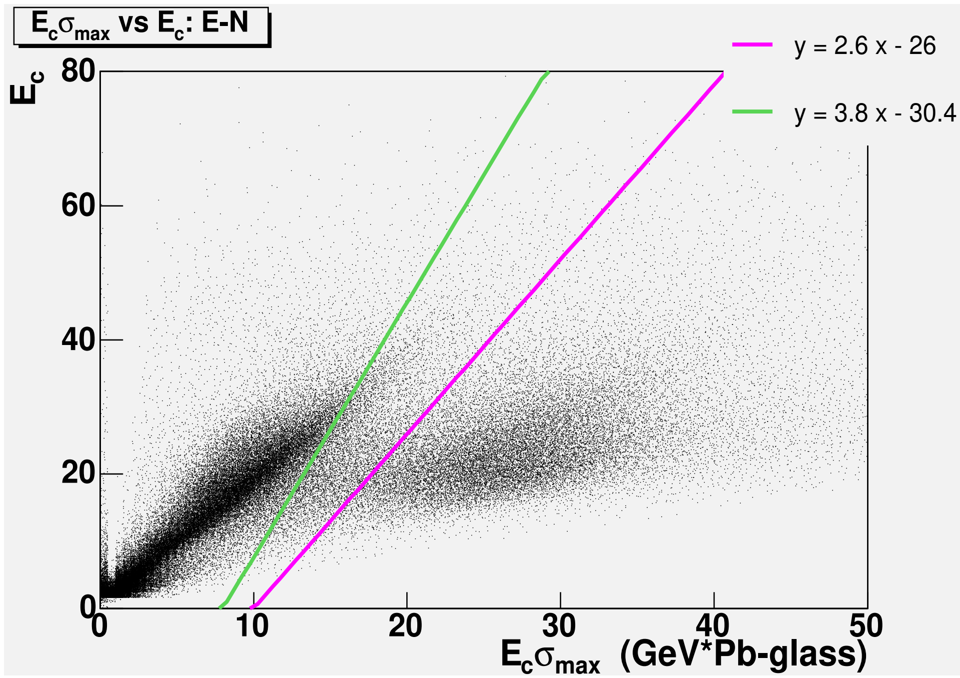

Figure 3.8: Category of clusters: East-North FPD

point is small (less than 0.2 unit of Pb-glass size or 0.8 cm) when we apply this parameterization of 1-photon fit to the simulation data (see Appendix A). Figure (3.9) plots a 2-D position difference of the fitted photon position from the simulated photon position. As for the photon energy, past experience tells us that sum of energy deposited in Pb-glass towers (E_c of equation (3.7)) is a good measurement of photon energy.

One thing that is interesting about Figure 3.9 is that the differences ($\delta x = x_0 - x_{simu}$ and $\delta y = y_0 - y_{simu}$) are not centered at 0. This probably reflects the finite-granularity of Pb-glass detectors. As the simulated data were generated with the default shower shape (which is also used in the fitting), it

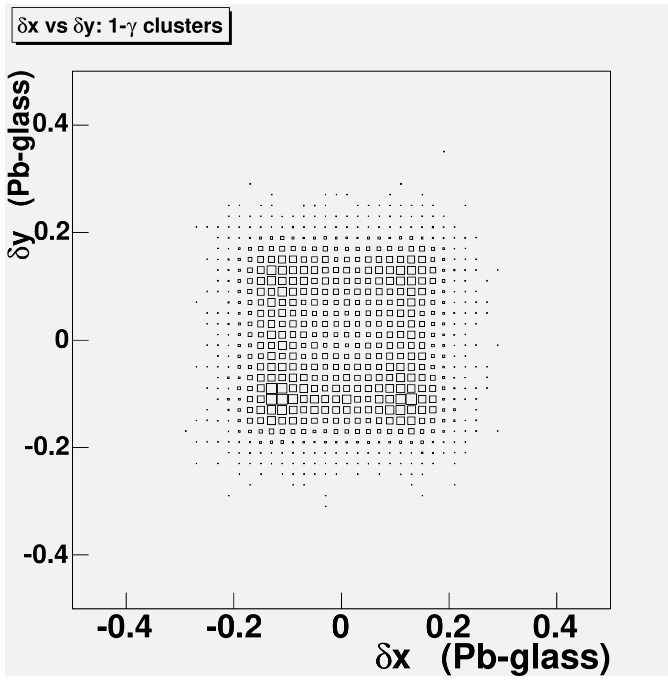

Figure 3.9: Difference of x and y for 1-photon clusters: moment analysis vs simulation.

is probably irrelevant that the default shower shape does not fully describe the characteristics of the shower observed at FPD Pb-glass towers.

3.5.5 2-photon Fit parameterization

Category-1 clusters are easy as fitting is concerned. However, when doing 2-photon fit for a category-2 cluster, simple using 2 sets (6 parameters in total) of the above parameter may not be appropriate. For example, let's look at a Category-2 cluster which most likely contains 2 photons. If we simply let Minuit handles the fit without any restriction or guidance, the parameter space is just too large. Remember that our Pb-glass detector has a cross-section of 3.81×3.81 cm^2 square. If we put a grid of 5×5 on this square (with spatial resolution roughly 0.8 cm), then for 10 towers (typical Pb-glass occupancy for 2-photon cluster), the position space alone for one photon is 250. For two photons we will need to square this number ($\approx 6 \times 10^4$). In addition, there are two more parameters for the two energies. Either We may end up with a bad fit for not sampling enough points or we try to cover the entire parameter space and thus require an unreasonable amount of computation power.

The way out is to realize that, first, we have a lot information about the cluster. Furthermore, we are only interested in the cases when the two photons are at least moderately separated (otherwise due to the granularity of Pb-glass we won't be able to distinguish the event from a single-photon event). A parameterization that will automatically put the two photons in separated positions is much better than the above naive parameterization. Luckily, if we just go back to equation (3.1), we find that using $d_{\gamma\gamma}$ as one of the parameter is intuitive. Things become clearer if we look at Figure (3.10).

Here we have two photons represented by two blue points labeled as 1 and 2. The blue point labeled as π^0 is the location where the parent π^0 would hit the detector if it did not decay. We call the x and y coordinates of point π^0 x_π and y_π respectively. The distance between points 1 and 2 is $d_{\gamma\gamma}$, while the line connecting points 1 and 2 forms an angle θ with the x-axis. In addition, if photon 1 (at blue point 1) has energy E_1 and photon 2 (at blue

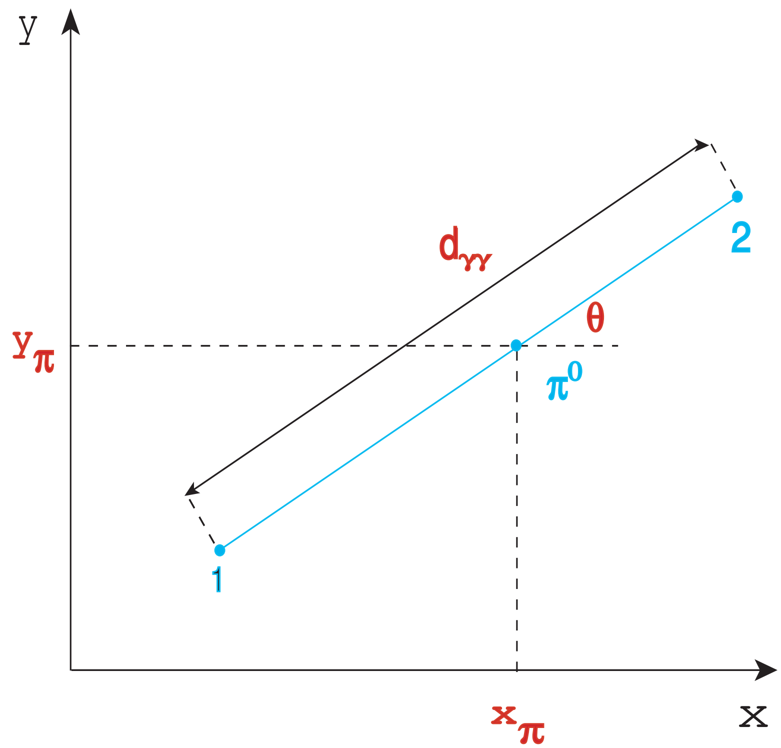

Figure 3.10: Parameters of 2-photon Fit

point 2) has energy E_2 (therefore the π^0 has energy $E = E_1 + E_2$), blue point π^0 should be the "center of mass" of blue points 1 and 2. In the case $E_1 = E_2$, or $z_{\gamma\gamma} = \frac{E_1 - E_2}{E_1 + E_2} = 0$, blue point π^0 should be right in the middle of line 12. In the other extreme when $|z_{\gamma\gamma}| \to 1$, blue point π^0 would approach the photon that has most of the energy from the decay.

The above parameterization of a 2-photon system at FPD is a general one. There are six parameters in total:

1. x_π: x-position of the fictitious π^0 hit position.

2. y_π: y-position of the fictitious π^0 hit position.

3. θ: polar angle of the line that connects the two photon hits in the detector's local coordinate system.

4. $d_{\gamma\gamma}$: distance between the two photon hits.

5. $z_{\gamma\gamma}$: energy sharing between the two photons, $z_{\gamma\gamma} = \frac{E_1 - E_2}{E_1 + E_2}$.

6. $E_{\gamma\gamma}$: total energy of the two photons, $E_{\gamma\gamma} = E_1 + E_2$.

From the above 6 parameters, we can easily compute the original 6 parameters:

$$x_1 = x_\pi - d_{\gamma\gamma} \frac{1 - z_{\gamma\gamma}}{2} \cos\theta \tag{3.25}$$

$$y_1 = y_\pi - d_{\gamma\gamma} \frac{1 - z_{\gamma\gamma}}{2} \sin\theta \tag{3.26}$$

$$E_1 = E_{\gamma\gamma} \frac{1 + z_{\gamma\gamma}}{2} \tag{3.27}$$

$$x_2 = x_\pi + d_{\gamma\gamma} \frac{1 + z_{\gamma\gamma}}{2} \cos\theta \tag{3.28}$$

$$y_2 = y_\pi + d_{\gamma\gamma} \frac{1 + z_{\gamma\gamma}}{2} \sin\theta \tag{3.29}$$

$$E_2 = E_{\gamma\gamma}\frac{1 - z_{\gamma\gamma}}{2} \tag{3.30}$$

Let's go back to the other point: the above parameterization fits well with the informations we can extract from moment analysis of the Category-2 cluster. 4 of the 6 parameters correspond directly to the result of moment analysis of the cluster: x_π is mapped to x_0 of equation (3.8), y_π is mapped to y_0 of equation (3.9), θ is mapped to θ of equation (3.17), and $E_{\gamma\gamma}$ is mapped to E_c of equation (3.7). Another parameter $d_{\gamma\gamma}$ is correlated to the size of cluster σ. The only parameter that is free (but restricted to $(-1, 1)$ by definition) is $z_{\gamma\gamma}$.

Next, let's see how well this parameterization works for the simulation.

First let's compare the difference of x_π and x_0 and the difference of y_π and y_0. We can see from Figure (3.11) that both of them are smaller than 0.2 unit of Pb-glass size (or 0.8 cm) in most cases.

Next compare the angle θ from simulation vs the one from moment analysis. We plot the difference vs the asymmetry of the cluster ($\sigma_{min}/\sigma_{max}$. We expect the difference for largely asymmetrical clusters (when the line that connects two photons is more obvious) is small. Indeed it is (Figure 3.12). For most cases, the difference is smaller than 0.1 radian.

From equation (3.24), we can see $d_{\gamma\gamma}$ is correlated with σ of a Category-2 cluster. Below we plot $d_{\gamma\gamma}$ from simulation vs σ of cluster from moment analysis (Figure 3.13).

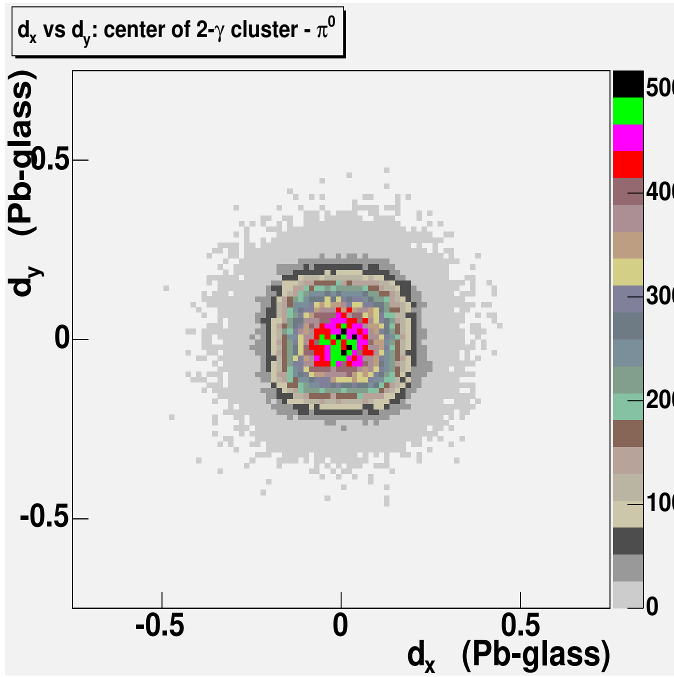

Figure 3.11: Difference in x_π and y_π: moment analysis vs simulation

For $E_{\gamma\gamma}$ and E_c, it is the question of how well we measure the photon energy. From past experiment, we know the energy resolution is roughly

$$\frac{\Delta E}{E} \approx 15\% \frac{1}{\sqrt{E}}, \tag{3.31}$$

when the energy is in GeV.

All in all, moment analysis provides a very good starting point for the parameters of the fits. This is crucial, as we pointed out at the beginning of the section. Minuit has much better chance of finding the right answer if it starts not too far away from the correct position.

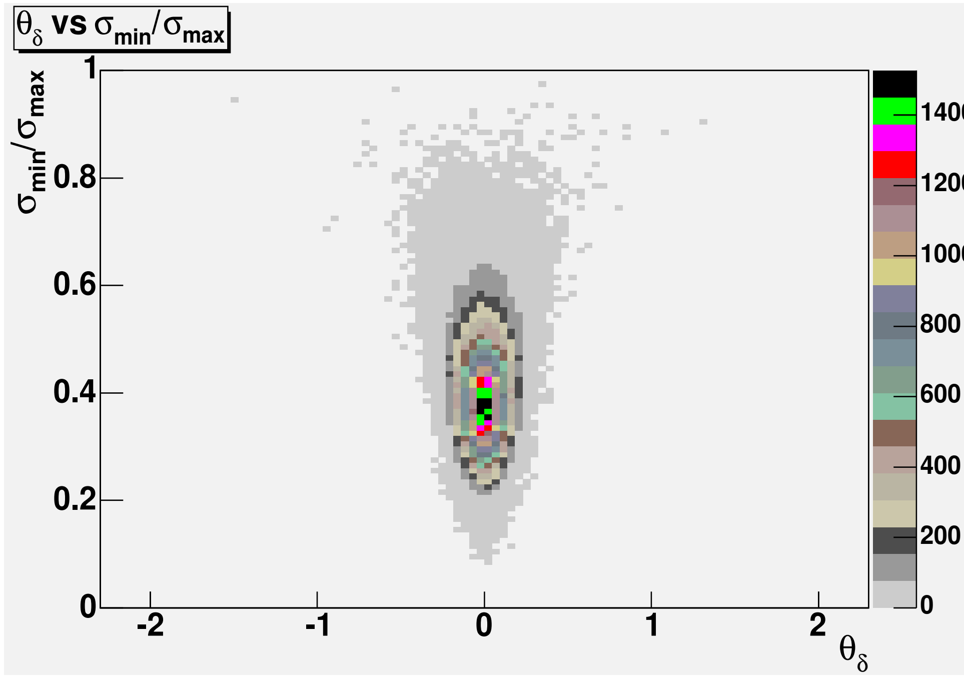

Figure 3.12: Difference in θ: moment analysis vs simulation

3.5.6 Fit procedure

Here we describe the flow chart of the fitting program.

1. For each event above a preset threshold (say, 25 GeV) for any given FPD module, we first divide the towers into clusters. For the operational defined of clusters, see Section (3.5.2).

2. Moment analysis is performed for all clusters. Depend on the 2nd moments of the cluster, it is categorized as either category-1, category-2, or category-0 cluster.

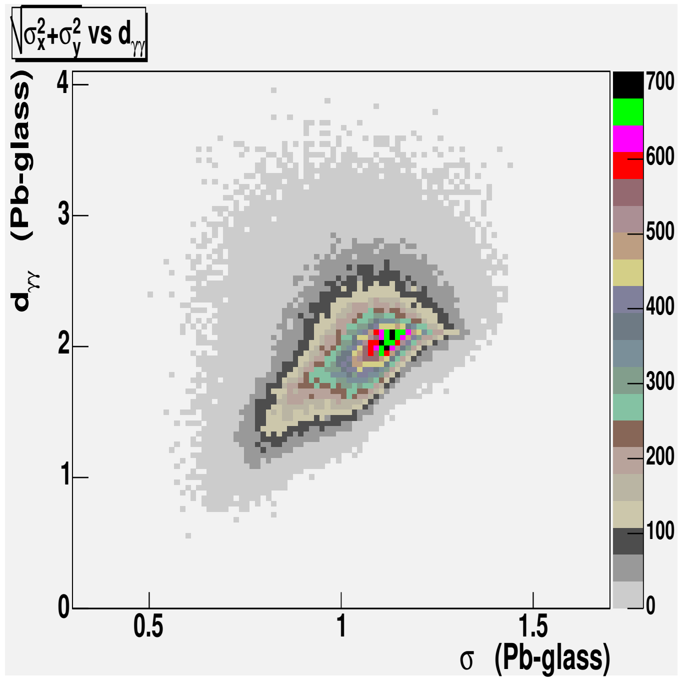

Figure 3.13: Correlation of $d_{\gamma\gamma}$ of simulation and σ from moment analysis.

3. For category-1 cluster, 1-photon fit is perform on the cluster. As a result, we obtain fitted photon energy and its x and y position.

4. For category-2 cluster, 2-photon fit is perform on the cluster. However, we require the goodness of fit (χ^2/NDF be smaller than a preset value). This is to reject clusters than contain too many towers to be justified as a 2-photon cluster. As explained in the definition of cluster at the end of Section (3.5.2), the operational definition used in this paper is appropriate for π^0 analysis, where we expect only 2 photons for the majority of events. There are events that looks very much like 3 or 4

photon events. When there are multiple photons, the chance of those photons are included in a single cluster increases. For this reason, it might be beneficial to use a different definition of cluster.

5. For category-0 cluster, 1-photon fit is tried first. If the goodness of fit (χ^2/NDF be smaller than a preset value), we consider the fit good enough and try the cluster as just a single photon hit. Otherwise, 2-photon fit is also tried. The χ^2/NDF for both fits are compared, and the better fit is selected. At the moment, the criteria used is just a simple straight comparison of the tow χ^2/NDF values, and the smaller χ^2/NDF is considered better. It is conceivable that a more elaborate criteria can be established (by applying the fitting program to full event simulation) and adopted later.

It is worth emphasizing that the quality of the fit depends on the quality of the shower shape function. As pointed out at Section (3.5.1), more efforts are needed in establish a good shower shape function.

3.5.7 Calibration of PMT Gains

To correctly measure the photon energy, we need to first calibrate the detectors. Past experience tells us that a good way to calibrate Electromagnetic Calorimeter such as FPD is through π^0 invariant mass reconstruction. If the PMT gains are calibrated correctly, we should see a peak at π^0 mass ($\approx$ 0.135 GeV).

One thing that comes up first is the definition of energy. There are 3 energy definitions used in our analysis: sum of energy deposited in all towers (tower-energy), or sum of energy within a cluster (cluster-energy), or the energy that is the result of the fitting program (fitted-energy). On one hand, tower-energy or cluster-energy is a quantity that is directly measured. On the other hand, because of the energy-dependency of longitudinal shower containment, fitted-energy might more accurately represent the incoming photon energy across the energy range. We have seen from Section (3.5.1) that the longitudinal shower containment factor could be significantly different for lower energy (a few GeV) photons and higher energy photons (greater than 20 GeV). For this reason, we choose the fitted-energy as the energy definition for calibration of PMT gains and for the rest of the analysis.

Since FPD North (or South) modules are made up of 7×7 array of Pb-glass detectors, there are cross-correlation of gains of nearby Pb-glass tower PMTs. Nevertheless, the following method had been used and were found to yield convergent PMT gain factors after multiple iterations.

Since events with only two Category-1 clusters represent the clearest di-photon events, we are going to use them to calibrate the gains. We start from a set of gains obtained from matching each PMT energy spectrum.

1. Sorting invariant mass by high tower: For each event with only two Category-1 clusters, reconstruct the event, and associate the invariant mass with the tower with highest energy deposit.

2. Determine the mass peak: Loop over all events and increment the corresponding invariant mass histogram associated with that particular high tower. In the end, we obtain $7 \times 7 = 49$ histograms. Find the mass peak M_{peak}.

3. Determine the new gain: The new gain for each tower PMT is then scaled by the π^0 mass:

$$g_{new} = g_{old}\frac{M_{\pi^0}}{M_{peak}} \tag{3.32}$$

4. Iterate the process until the gains converge.

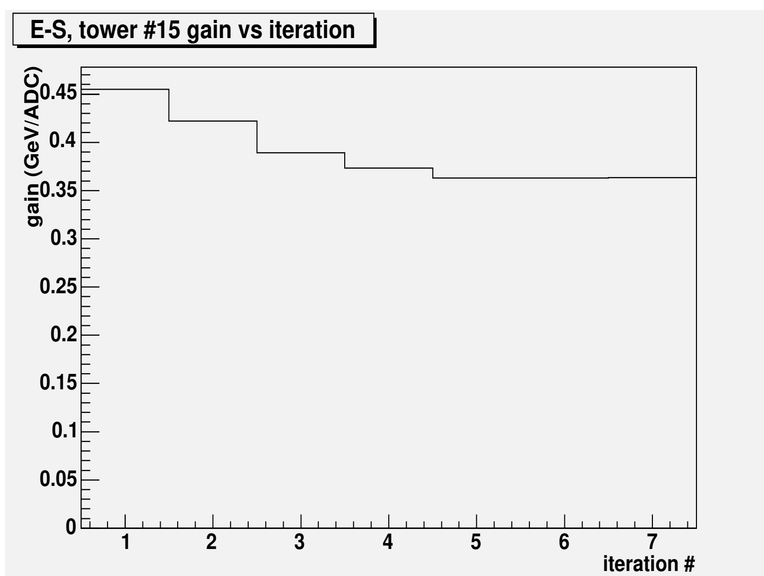

Figure 3.14: Gain vs Iteration for East-South tower #15.

The gains converged after several iterations for East-South FPD tower #15 (Figure 3.14).

3.5.8 Summary of FY03 π^0 Reconstruction Steps

To summarize, here are the Analysis Steps to reconstruct π^0 events.

1. Clustering and moment analysis: For each event, divide the towers into clusters, and perform moment analysis on every clusters.

2. Event categorizing: decide whether a cluster is category-1 (most likely containing just 1 photon), category-2 (most likely containing 2 or more photons), or category-0 (ambiguous case).

3. Fitting using shower-shape function.

4. Use events with only one category-2 clusters for calibration of PMT gains.

5. Use matched gains for asymmetry analysis.

3.5.9 Remaining Issues

Finally, let's address two remaining issues in the FY03 analysis program. Both issues are related to the imperfection of the default shower shape used. The first issues is related to the longitudinal profile of the shower, while the second one has to do with the transverse shower profile.

One bad feature of π^0 reconstruction using the default shower shape is that the reconstructed π^0 invariant mass has an energy-dependence. Specifically, we saw the peak of the invariant mass distribution increased as the energy of the photon pair, by roughly 10% from energy bin of 20-30 GeV to energy bin of 45 GeV and above. This (and other things) lead us to investigate the possibility that photons of different energy have different shower-shape. In case, the effect might be two-fold. One is that the overall scale of the shower-shape function, *i.e.* the integral of the shower-shape, might depend on the photon energy, taking into account that there are materials in front of the Pb-glass towers (materials in STAR, beam pipe, lead-plate shower converter, pre-shower Pb-glass). The other is that shower-width could be energy-dependent.

Our Russian colleagues at Protvino have done some simulations on shower shapes of Pb-glass. Figure (3.15) shows preliminary 1-D shower shape simulation, where r is the distance of the photon from the center of Pb-glass.

We can see from Figure (3.15) that the shower shape depends on how much materials are in front of Pb-glass detectors. Also, in the case there are substantial materials upstream, the shower shape is clearly energy-dependent. It is evident that the overall scale of the shower-shape function, *i.e.* the integral of the shower-shape which represent the maximum fraction of energy that could be deposited in FPD towers, actually depends on the photon energy. On the other hand, we need to parameterize those simulation data points to say whether the shower width is also energy-dependent. One thing is clear, default shower shape alone would not be able to describe the detector responses

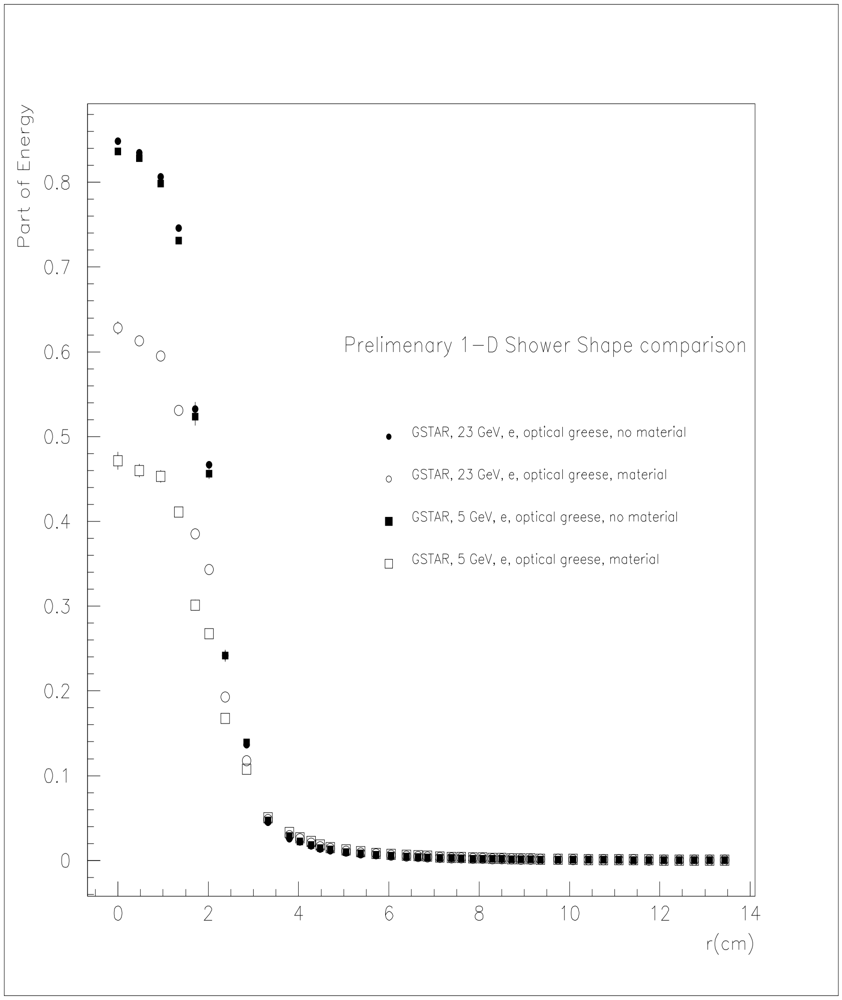

Figure 3.15: Preliminary 1-D shower shape simulation.

well.

Before we embark on parameterization, we want to show, through some simple calculations, that energy-dependent Pb-glass detector response is not unexpected. For FY03 p-p run, the material in front FPD Pb-glass towers includes 1 radiation-length of STAR material and beam pipe, 1.27 cm thick lead sheet (2.3 radiation length), and 1.5 radiation-length of pre-shower Pb-glass (see Section 2.4.2). The non-active lead sheets were put in from of pre-shower Pb-glass to improve the effectiveness of SMD, so very high energy photons (particular for $\sqrt{s} = 500$ GeV RHIC proton runs in the future) can be separated by SMD. The downside of this arrangement is that low energy photons will lose a larger percentage of their energy in the lead sheet (and this part of energy lost is not measured) than high energy photons, as will be shown below.

Electromagnetic cascades (showers) within material have been carefully studied before. For convenience, we put down Equations (26.28, 26.29 and 26.30) of [29] here. It is useful to use t as distance in unit of radiation length and y as energy in unit of critical energy of electron in Pb,

$$\begin{aligned} t &= x/X_0, \\ y &= E/E_c. \end{aligned} \tag{3.33}$$

The longitudinal profile of the shower can be modeled as

$$\frac{dE}{dt} = E_0 b \frac{(bt)^{a-1} e^{-bt}}{\Gamma(a)}. \tag{3.34}$$

The shower maximum occurs at $t = t_{max}$

$$t_{max} = (a-1)/b = 1.0 \times (\ln y + C_j), \quad j = e, \gamma \tag{3.35}$$

where $C_e = -0.5$ for electron induced shower and $C_\gamma = 0.5$ for photon induced shower. Furthermore, we will use an energy-independent $b = 0.5$ for the following rough estimate.

For simplicity, we will treat as if there were 4.8 radiation-length of Pb-glass materials right in front of Pb-glass tower and the EM shower was transversely fully contained by these materials and Pb-glass towers. On the other hand, to calculate the total energy deposit in Pb-glass towers, we will only integrate over the length of the towers. Remember that 45 cm of Pb-glass is 18 radiation length, we then integrate from $t = 4.8$ (end of pre-shower Pb-glass and beginning of Pb-glass tower) to $t = 4.8 + 18 = 22.8$ (end of Pb-glass tower). In this simply model, we can just use $C_j = C_\gamma = 0.5$. Nevertheless, calculation using $C_j = C_e = -0.5$ (electron shower) is done, just for the sake of comparison.

Armed with the above information, we can then integrate Equation (3.34) over t from $t = t_0$ to $t = 18.0 + t_0$, (t_0 is the radiation length of material in front of Pb-glass) for 5 GeV photons and 23 GeV photons, using both $C_j = C_e = -0.5$ and $C_j = C_\gamma = 0.5$. The results are collected in Tables (3.2–3.3).

Although our simple model is crude, it does show possible energy-dependence of measurement of total energy in Pb-glass towers. The crucial

Table 3.2: Tower Energy containment of EM Shower ($t_0 = 5$ radiation length in front).

E_0	C_j	t_{max}	a	$\Delta E/E_0$
5 GeV	$+0.5$	6.25718	4.1286	0.7753
5 GeV	-0.5	5.25718	3.6286	0.6850
23 GeV	$+0.5$	7.78324	4.8916	0.8708
23 GeV	-0.5	6.78324	4.3916	0.8140

Note: we use an energy-independent $b = 0.5$, and 5.0 radiation length of materials in front of Pb-glass towers.

Table 3.3: Tower Energy containment of EM Shower ($t_0 = 1$ radiation length in front).

E_0	C_j	t_{max}	a	$\Delta E/E_0$
5 GeV	$+0.5$	6.25718	4.1286	0.9816
5 GeV	-0.5	5.25718	3.6286	0.9865
23 GeV	$+0.5$	7.78324	4.8916	0.9632
23 GeV	-0.5	6.78324	4.3916	0.9767

Note: we use an energy-independent $b = 0.5$, and 1.0 radiation length of materials in front of Pb-glass towers.

point is the 7.0 radiation length of materials in front of Pb-glass. In fact, if we use only 1.0 radiation length of materials in front of Pb-glass, the energy-dependence would be much smaller (Table **??**). The reason is simple. Figure (3.16) plots the longitudinal profile function (Equation 3.34).

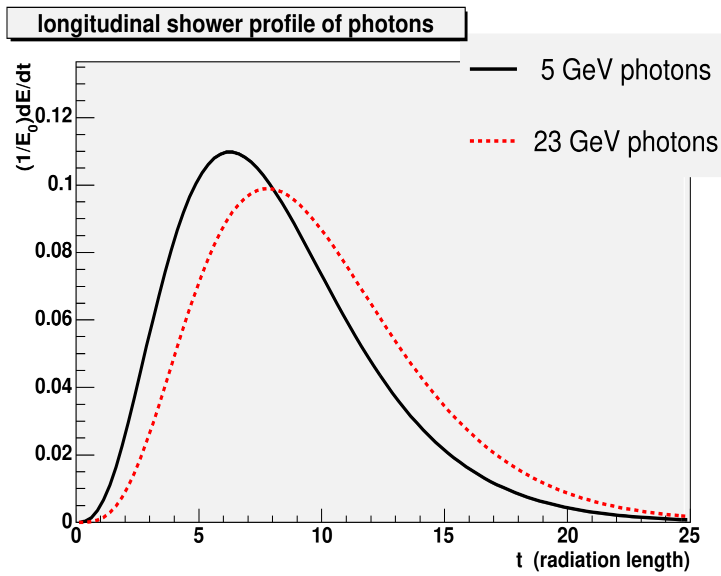

Figure 3.16: Longitudinal shower profile.

We can see for low energy photon, more materials in front of Pb-glass (in addition to 1.0 radiation length of STAR materials) will cut on the front of the peak and thus quickly reduce the fraction of total energy deposited. Low energy photons also have small tail, thus less leakage through the back of Pb-glass detector. For high energy photon, tail of the distribution is more. Actually more materials in front (≈ 1.0 radiation length) will increase slightly the fraction of total energy deposited. Beyond that, more materials will also quickly reduce the fraction of total energy deposited (but slower compared to lower energy photon).

As a side note, if Shower-Maximum-Detector (SMD) is not used, it might be better to have less (or no) additional materials in front Pb-glass towers so that we have better low-energy photon detection and we don't need adjustment for energy-dependent total energy containment. On the other hand, if the materials in front of Pb-glass also measure the EM energy deposit in them (preferably sectioned 7×7 exactly as the Pb-glass towers), the sum of a pre-shower and the tower right behind it would provide a good measurement of EM energy, with less energy dependence. Otherwise, detailed simulations (and calibration experiment) are needed to full understand the detector responses. In the case of FPD configuration of FY03, more simulations are the way to go, not only in the total energy calibration, but also for transverse shower shape.

It is also pointed out in [29] that transverse distribution of Electromagnetic shower is also energy dependent. However, no simple formulae are given. To repeat, we will have to resort to more detail simulations to find the correct parameterization of Pb-glass shower-shape. Our Russian colleagues at Protvino have been working in this direction and have make significant progress. Their findings will be incorporated into the final analysis program.

For the case of 5.0 radiation length of material in front of Pb-glass tower, we can plot the longitudinal shower containment, namely assuming full transverse containment, from our simple model calculation. In F figure (3.17), the 7 points correspond to the above longitudinal shower containment calculation. The dotted line is the following function

$$\rho = \ln(E/E_c)\,,$$
$$C(E) = c_0 + c_1\rho + c_2\rho^2\,, \tag{3.36}$$

where $c_0 = 0.02$, $c_1 = 0.186$, $c_2 = -0.0095$, and E_c is the critical energy introduced in Equation (3.33). We can see that the function describes the longitudinal shower containment reasonably well. We will use such a function as an overall scale multiplying the transverse shower profile (what we called $\Delta E/E_0$ in Tables 3.2–3.3), to account for the energy dependent shower containment. Of course, when more simulation data are available, the parameters of the function $C(E)$ will be updated.

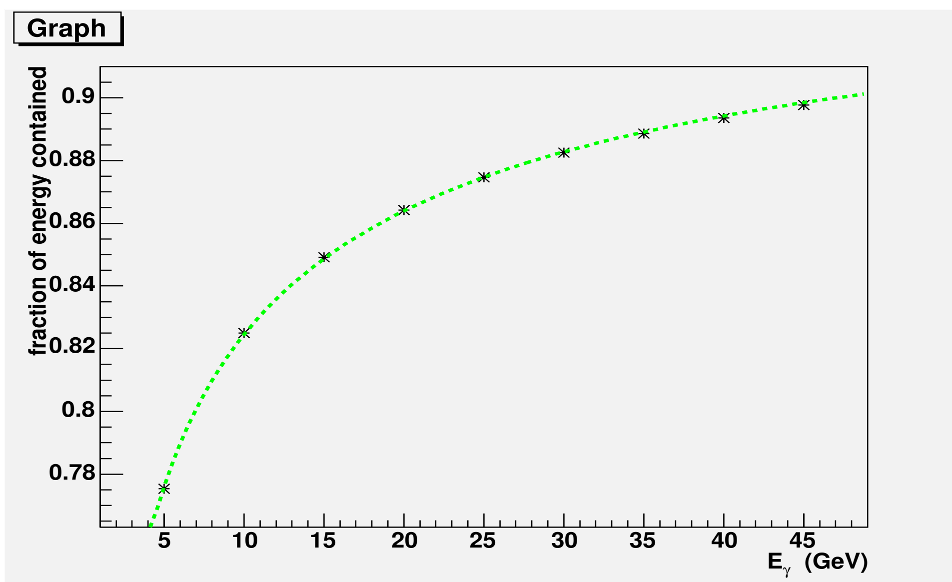

Figure 3.17: Longitudinal shower containment.

One natural way to reduce the invariant mass peak's dependence on the energy is to include energy deposited in the pre-shower towers. Once the 7 pre-shower towers are correctly calibrated (in a similar manor as the 7×7 towers), inclusion of pre-shower towers makes the total energy sum less sensitive to the incident photon energy, since there are less inactive materials upstream and the total radiation length of the active region becomes larger. In fact, the final analysis program will include the pre-shower Pb-glass detectors, as preliminary study indicates that doing so improves both energy and mass resolution of the analysis program.

Next consider the effect of a inaccurate shower-shape function on the photon position reconstruction. Let's briefly go back to the EM shower itself (albeit integrated over the Pb-glass length). And for simplicity, we consider just 1-D analog. Suppose that compared with the real EM shower, the model we use has a narrow functional form. The energy deposit in towers around the high-tower is given by the actual shower-shape (when we ignore fluctuation and digitization errors). However, using the model with narrow shape, if we put the photon hit at its actual location, the predicted energies in the towers surrounding the high-tower would be less than the actual measured ones. Consider the 2nd-highest tower since it would contribute more to χ^2 besides the high-tower. To compensate for the fact that 2nd-highest tower has more energy, the fitting algorithm would then move the position of the photon toward the 2nd-highest tower (the edge of the high-tower). Thus, the fitting will result in enhancement of photon position distribution at the edges of towers.

Conversely, if the shower model used in the fitting is broader than the actual shower, the fitting will enhance photon position distribution at the centers of towers.

In Figures (3.18, 3.19), we show the fitted photon position distribution using the default Lednev shower shape. The width of Pb-glass is 3.81 cm, and the outer-edge of the first column (row) of Pb-glass is located at $x = 0$ (or $y = 0$). It is obvious that there are clear peaks at the edges. The default shower shape is too narrow. (A word of caution for Figures 3.18, 3.19, 3.22, and 3.23: those figures were plotted using present gain calibrations. As pointed out earlier, we are still in the process of better understanding the gains. Substantially different final gains may change the characteristics of those figures.)

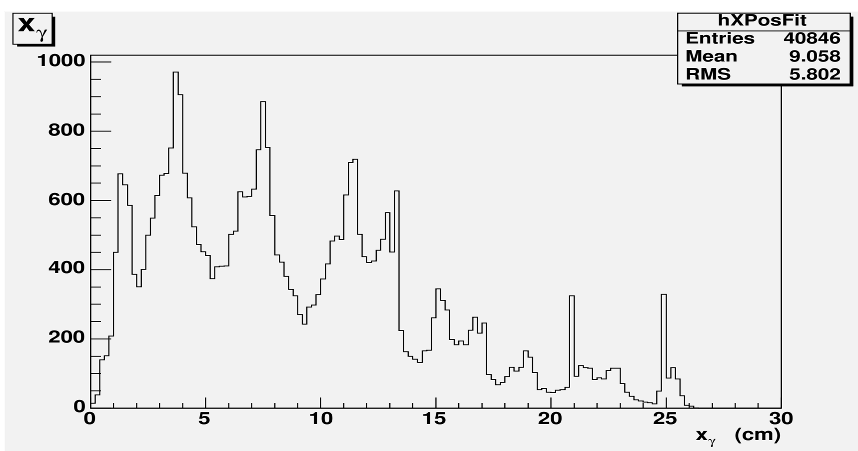

Figure 3.18: x_γ distribution using default shower shape.

A few words on the features of Figures (3.18, 3.19) are in order. First of all, in Figures (3.18), we see a falloff of number of entries from small x to

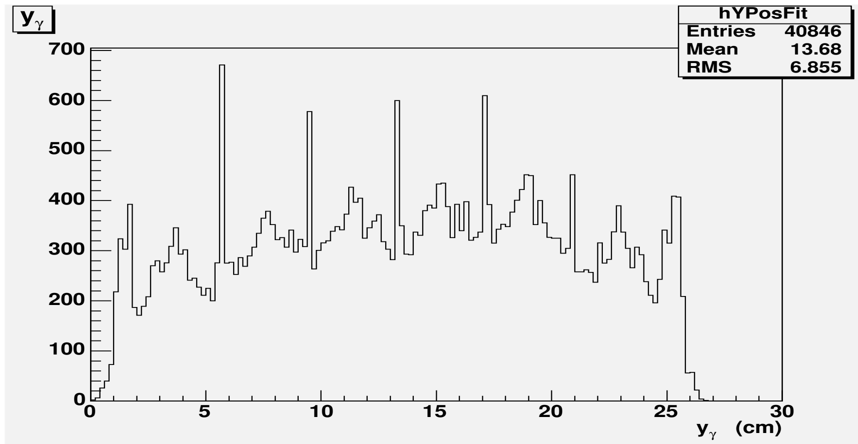

Figure 3.19: y_γ distribution using default shower shape.

large x. This is the expected behavior of event rates falling with increasing P_T, as small x represents position closer to the beam pipe (hence smaller P_T) and large x represents large P_T. Another feature (particular obvious in Figure (3.19)) is narrow spikes at precise the location of centers of tower. The reason is simple. The fitting program fits photon hit(s) within each cluster (we will describe what clusters are and how we use them in the following sections). There are clusters that consists of only 1 or 2 towers. In addition, the fitting program initially puts the hypothetical position of the photon at the "center" of the cluster. For clusters with only 1 tower, the "center" of the cluster is **always** exactly at the center of the tower. For clusters with only 2 towers, one of the x and y position of the "center" of the cluster is **always** exactly at the common center of 2 towers. Because the fitting program has only 1 or 2 data point(s), it will not move the x and (or) y position of fitted photon. Hence we see those artificial spikes. If we require the clusters to have at least 3 towers while looking into these distribution of fitted photon positions, we can largely eliminate these spikes (it is still possible that 3 or more towers are aligned in either x or y and hence produce such enhancement at the center, but the probability of such configuration decreases rapidly with increasing number of towers).

Another fact that has been neglected in the previous shower-shape analysis of FPD Pb-glass towers is the possibility of different shower-shape parameters in x direction or in y direction. The reason for these possible differences is purely geometrical. Take FPD East-North module for example. The x direction is the horizontal axis, while y is the vertical axis. Remember that East-North is placed to the north side of and parallel to the beam pipe, with the center of 7×7 roughly at the same height as the center of beam pipe. This means that the center of East-North FPD towers is at $y \approx 0.$ but at $x \neq 0$. At the far position of FPD, $|x| = 30$ cm. For a photon coming from the STAR IP ($|z| = 750$ cm from STAR IP to FPD) and hitting the center of East-North, vertically (in y direction) the photon is parallel to the beam, but horizontally (in x direction) it is at angle of 0.04 radian. This is small until we consider the length of a Pb-glass, 45 cm. From front of the Pb-glass toward the end, that angle makes a horizontal shift of 1.8 cm. That is almost half the width of Pb-glass. Even if the whole length of Pb-glass (45 cm) over-estimate the effect (the photon will deposit most of its energy in less distance), it is still clear that a photon is more likely to deposit more energy in another tower in horizontal (x) direction than vertical (y) direction. Consequently, shower-shape in horizontal (x) direction should be broader than in vertical (y) direction for North (or South) modules. For Top (or Bottom) modules, because of reverse roles of horizontal and vertical in terms of x and y, the situation is just the reverse. In any case, direction-dependent shower-shape is not such a crazy idea for current FPD setup.

New energy-dependent shower-shape function:

$$F(x, y, E) = \frac{C(E)}{2\pi} \sum_{i=1}^{2} a_i \left(\arctan \frac{(x/b_i)(y/c_i)}{\sqrt{1 + (x/b_i)^2 + (y/c_i)^2}} \right), \tag{3.37}$$

where d is the width of a Pb-glass detector, and $C(E)$ is the energy-dependent longitudinal shower containment function in Equation (3.36). Let me repeat the importance of $C(E)$ as a function of photon energy E: it may have a significant effect on the energy calibration of the calorimeter. A good choice of $C(E)$ should hopefully make the calibrated gains independent of the energy. Notice also that x and y have independent set of shape parameters b_i and c_i (to accommodate the possibility of different parameters in x and in y, as discussed above). All of a_i, b_i and c_i may have varying degrees of dependence on E. When the final simulation data are out and there more data points at different energies, we can try to model the energy dependence of a_i, b_i and c_i. Until then, we just use the following parameterization in Table (3.4).

Now let's present a new set of parameters and compare the 1-D (x direction) shower shape with that of the preliminary shower simulation results. For the moment, the simulation data of shower profile is 1-D. We will use them to get a_i and b_i (x direction). We simply pick a different (but smaller) set of

c_i for y directions. Of cause this may change later.

Table 3.4: New Shower-shape parameters.

E	$C(E)$	a_1	a_2	b_1	b_2	c_1	c_2
5 GeV	0.776	0.60	0.40	1.05	0.60	0.95	0.50
23 GeV	0.871	0.14	0.86	1.05	0.60	0.95	0.50

Note: $C(E)$ are from our model for 5 radiation length of material in front of Pb-glass towers

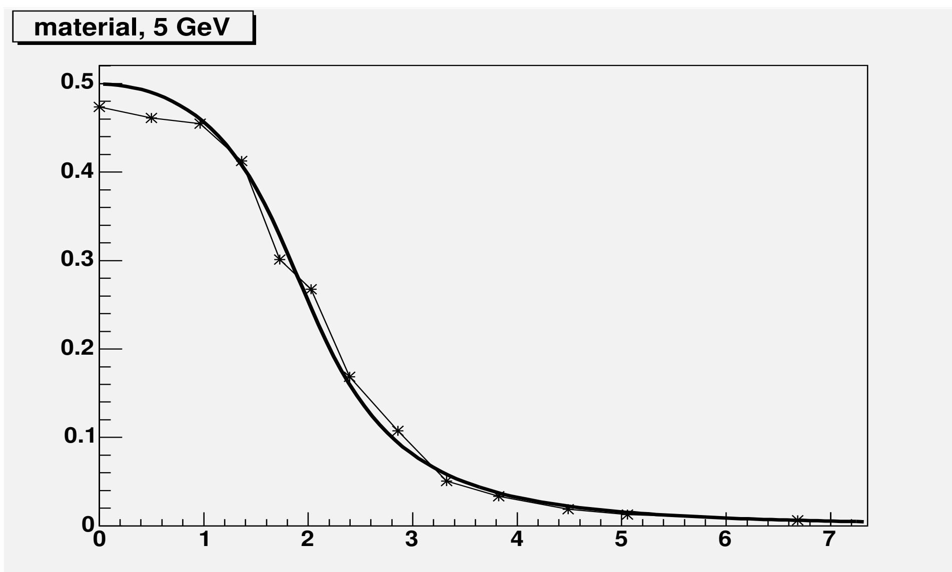

Figure 3.20: 1-D shower shape (5 GeV).

The comparison with simulation is shown in Figures (3.20–3.21). We can see that our new shower shape function (including the overall longitudinal shower containment factor from our simple model) is not too far off from the simulation (except that we speculate on different y-direction shape).

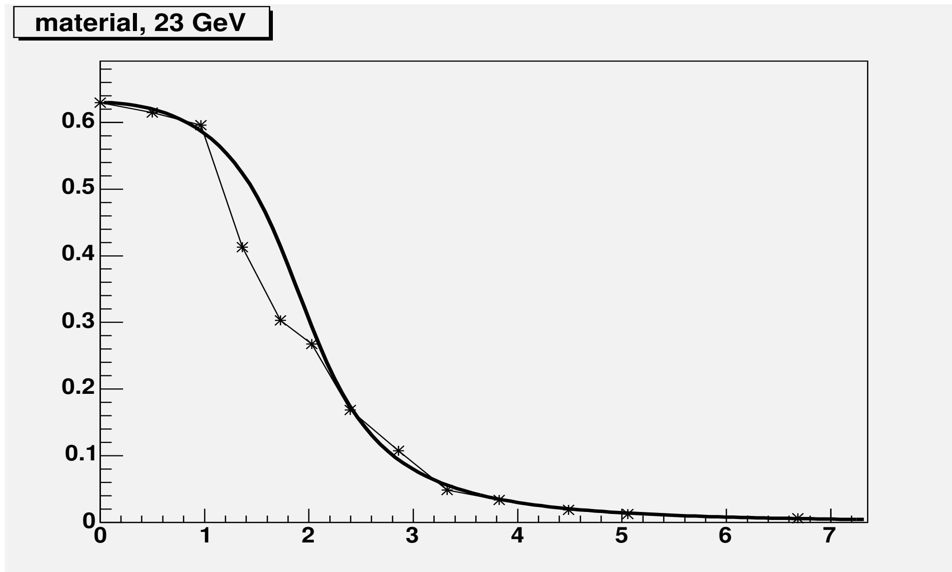

Figure 3.21: 1-D shower shape (23 GeV).

If we use the new shower shape function and repeat the analysis that led to Figures (3.18, 3.19), the new fitted position distributions will look like Figures (3.22, 3.23):

If we had better energy-dependent transverse shower-shape parameters, we would certainly improve the fitting result and get a more smooth position distribution. See the discussion in Appendix A.

To conclude the this section, we should note that the above discussion of alternative shower shape does not effect the previous discussion of clustering and moment analysis qualitatively. The principles behind those analysis (section 3.5.2) are independent of the details of the shower shape.

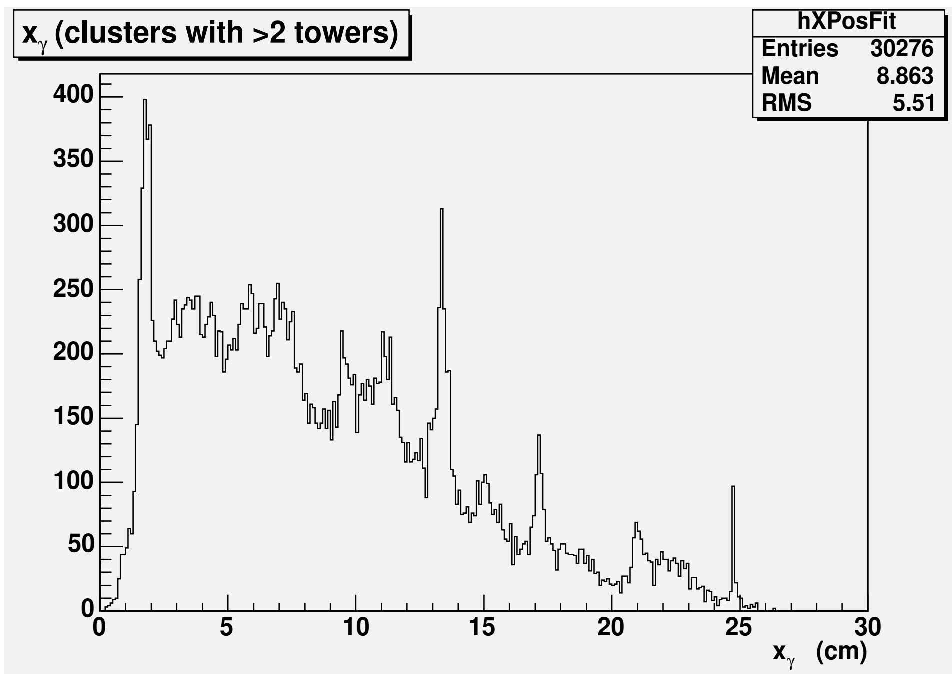

Figure 3.22: x_γ distribution using new shower shape.

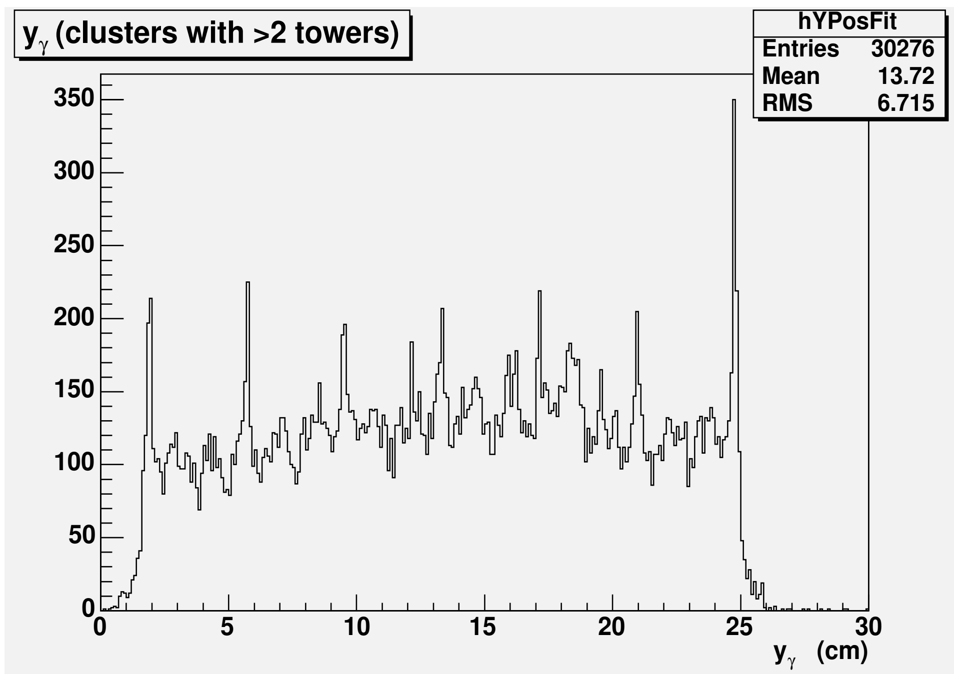

Figure 3.23: y_γ distribution using new shower shape.

Chapter 4

Result

FY02 FPD analysis result [37] will be presented. As the analysis of run FY03 p-p data taken at FPD is still on-going and no final result is available at this moment, we will show briefly a comparison of full simulation (PYTHIA event generation and Geant (GSTAR) detector simulation) [34, 35] and FY03 data.

4.1 FY02 FPD results

As discussed in Section (2.1) regarding the polarization and the CNI polarimeter analyzing power, we assume an average value of $\langle P_{beam} \rangle = 0.16$ for the Yellow beam.

The luminosity was measured by STAR BBC (Equation 3.4), with $\sigma_{BBC} = 26.1 \pm 0.2(\text{stat.}) \pm 1.8(\text{sys.})$ mb.

For FY02, all FPD modules (North, South, Top, and Bottom) were read out when the energy deposited in any of the modules was above 15 GeV electron-equivalent energy. Further more, BBC coincidence was required to select proton-proton collision events. Non-collision background was suppressed to the level of 1% by this requirement. To account for the bias introduced by this requirement, the cross section measured by FPD was increased by 10%, according to the simulation (Section 3.3).

Since FPD was at a fixed position, average P_T, E_π and x_F were correlated.

For the cross section measurements, data with $3.4 < \eta < 4.0$ were selected, with $\langle eta \rangle = 3.8$ independent of E_π. Major factors of uncertainty of the cross section measurements were:

1. absolute transverse position of the detector relative to the beam pipe (10%). This affected the angle measurement of the π^0 momentum, and led to uncertainty of the normalization of the cross section.

2. absolute luminosity determination (8%).

3. model dependence of BBC efficiency (8%). BBC coincident condition imposed in the analysis introduced bias. The cross section thus needed a correction based on simulation. An uncertainty was thus introduced.

In contrast with measurement at mid-rapidity at lower $\sqrt{s}$ [38], Figure (4.1) showed good agreement between NLO pQCD calculation (particularly the one used "Kniehl-Kramer-Pötter" (KKP) set of fragmentation functions [39]) for single spin asymmetries at forward region, despite the fact that P_T is in the region of only a few GeV. At midrapidity but at higher $\sqrt{s}$, results from inclusive charged-hadron production in $p\bar{p}$ collision at $\sqrt{s}$ above 200 GeV [39] and inclusive π^0 production in pp collsion at $\sqrt{s} = 200$ GeV [40] show

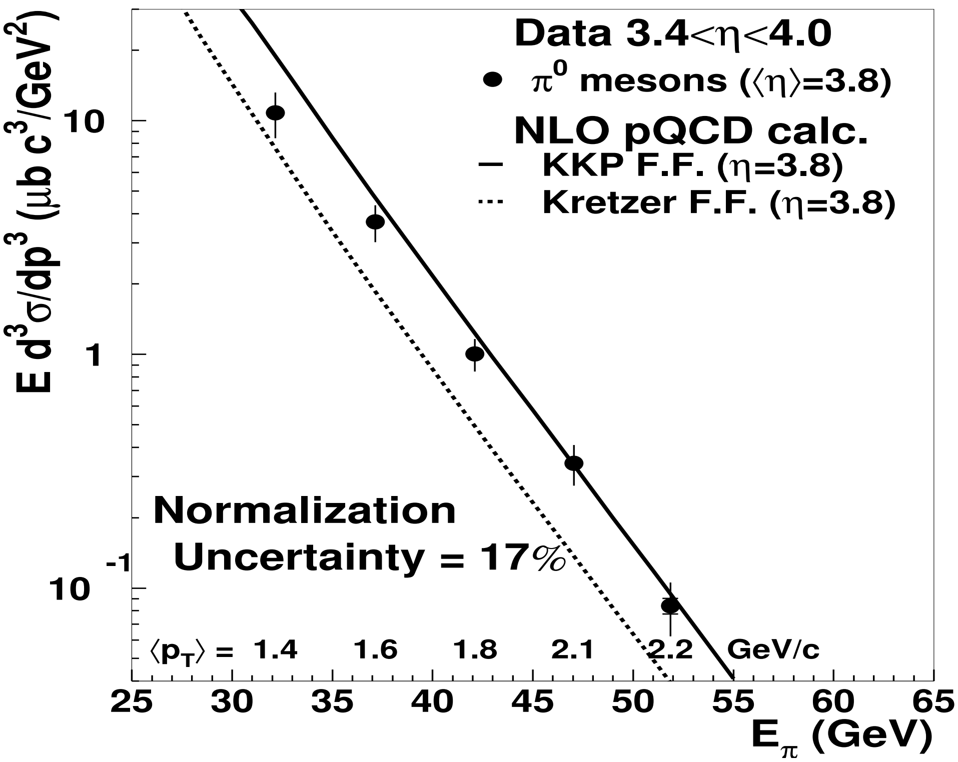

Figure 4.1: FY02 Invariant differential cross section for inclusive π^0 production versus leading π^0 energy.

The inner error bars were the statistical uncertainty, and were smaller than the symbols for most data points. The outer error bars were the statistical and E_π-dependent systematic uncertainties added in quadrature. The curves were NLO pQCD calculations evaluated at $\eta = 3.8$ using different fragmentation functions.

agreement between inclusive particle production cross section and state-of-art NLO pQCD calculations down to quite low p_T ($\approx$ 1 GeV/c). It seems that the understanding of cross section of particle production extends over a much greater pseudorapidity range at RHIC energy than that at lower collision energy. As pointed out in [10], the implication is significant. Present NLO pQCD calculations under-estimate the cross section of E704 by roughly an order of magnitude, which suggests that soft processes dominate. STAR FY02 FPD result at $\sqrt{s} = 200$ GeV, on the other hand, seems to be consistent with pQCD calculation. This seems to indicate that hard scattering dominates in the kinematic region probed here.

In Figure (4.2), the analyzing power A_N measured by FPD North module (beam-left detector) is plotted again x_F. The solid points are identified π^0 events, while the open points are total energy, no π^0 reconstruction or fiducial volume cuts, and are shifted by $x_F = +0.01$ to ease viewing. For the solid points, $x_F = 2E_\pi/\sqrt{s}$, and for the open points, $x_F \approx 2\langle E_{tot}\rangle/\sqrt{s}$, where E_{tot} is the sum of total energy deposited in the calorimeter. The trend of non-zero (large) single spin asymmetries of inclusive π^0 production is preserved at $\sqrt{s} = 200$ GeV. The agreement between open points and solid points indicated that A_N was not sensitive to the π^0 reconstruction algorithm used. This was not surprising since simulation revealed that most (90%) of the high energy events were photons from π^0 decays. A_N as measured by the beam right detector (Pb-glass array) is similar. A systematic error was assigned to bring the difference between A_N shown in Figure (4.2) and the average A_N of beam-left

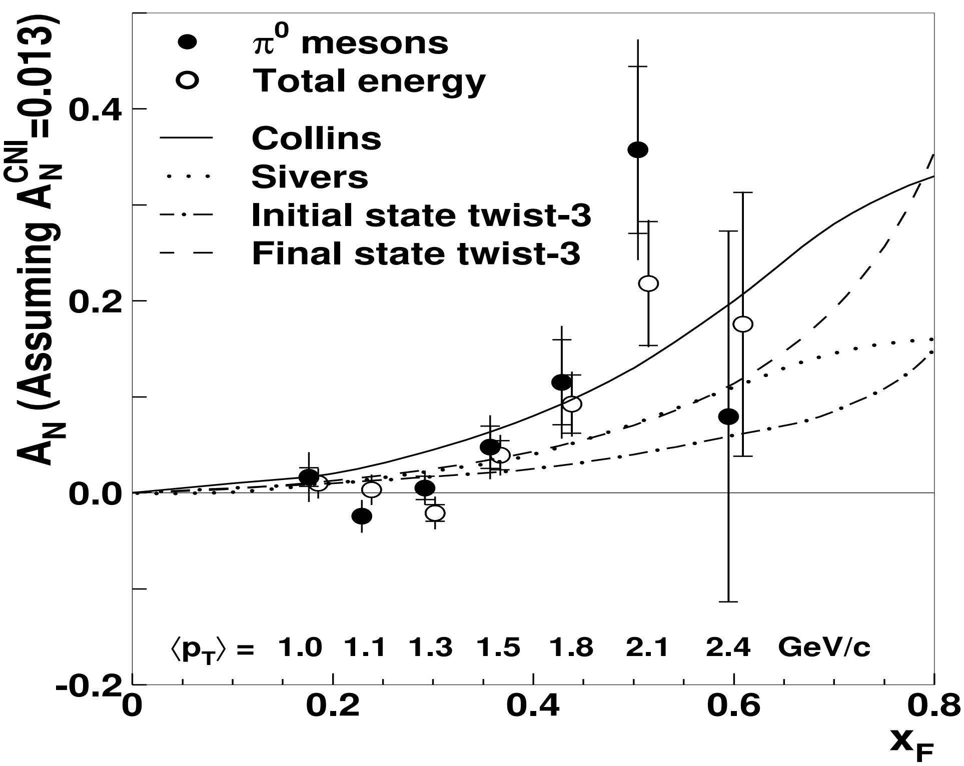

Figure 4.2: FY02 Analyzing powers versus x_F.

The inner error bars were the statistical uncertainty, and the overall errors were the statistical and point-to-point systematic uncertainties added in quadrature. The curves were predictions from pQCD models evaluated at $p_T = 1.5$ GeV/c. The measured A_N values are proportional to A_N^{CNI} at 100 GeV, which were assumed to be 0.013 (Section 2.1.

and beam-right data within one standard deviation of the average. In addition (not shown in the plot), asymmetries from Top and Bottom Pb-glass arrays were consistent with 0, as expected.

Although STAR's A_N covers roughly similar dynamics range in x_F as E704, we must keep in mind that FPD is roughly at a fixed location in θ, while E704's data covers a wide range of *theta* (however, non-zero A_N occurs only at small *theta* for E704). This fact signifies the importance of quantitative understanding the cross section measure in the forward region [10]. Also, the good agreement between FY02 cross section measurement and NLO pQCD calculation provides more confidence in the theoretical pQCD prediction to a non-zero A_N. It may well be that STAR measurement is the first to probe a large non-zero leading-twist pQCD single-spin asymmetry [10].

We would certainly like to distinguish between different leading twist intrinsic $\kappa_\perp$ effects and higher twist effects. To accomplish this goal, we need more precise measurement at higher P_T region, and even better will be measurement of the P_T-dependent of the asymmetries.

One comment about the FY02 measurement that is related to the above remark is that for FY02, the individual photon energy was derived (from the total energy measured in towers) as proportional to the energy deposit at SMD. Although SMD gives good positional information, its energy resolution is poorer than that of towers. As a result, the measure π^0 position (hence its η and P_T), being dependent on the relative photon energies, would have a larger systematic error. With the upgraded FPD (Pb-glass array) towers and new analysis algorithm described in this paper, we hope that we can improve the accuracy of such measurement.

4.2 Comparison with simulation

Now we have some ideas about what we may expect from FY03 run data, let's review the status of FY03 analysis. At present, the detector calibration is still on going, as we are trying to overcome the shortcoming of the default Pb-glass shower shape function and resolve the issue of energy dependent invariant mass peak (see Section 3.5.9).

Meanwhile, we have applied the analysis method described in chapter 3 to both the Geant simulation and FY03 data. The red lines are for Geant simulation, black lines are for FY03 data. For all the events selected (above 25 GeV of summed energy in towers, with π^0 reconstructed) we also applied a cut on the energy sharing ($z_{\gamma\gamma} < 0.7$). We should emphasize that the comparison was done using gain factors that could be substantially different than the final gains. When issues mentioned in Section (3.5.9) are resolved and final gains are obtained, we will repeat the comparison.

In Figure (4.3) we plot the energy reconstructed π^0 from FY03 pp run data and Geant simulation. They agree rather well. We see the expect exponential falloff of number of events as a function of π^0 energy.

We expect the distributions of $z_{\gamma\gamma}$ to be flat, and indeed they were.

The distributions of distances between the 2 photons also looked simi-

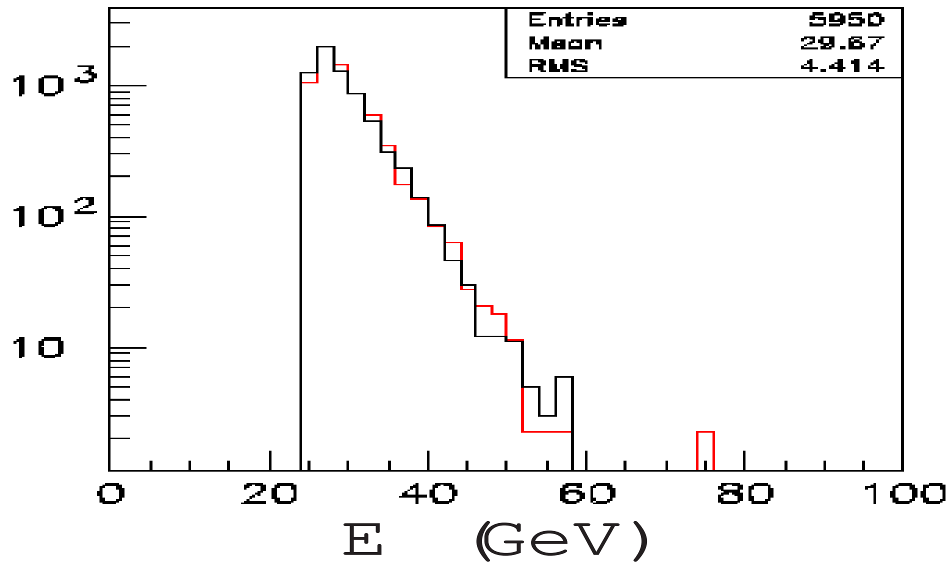

Figure 4.3: Energy of reconstructed π^0

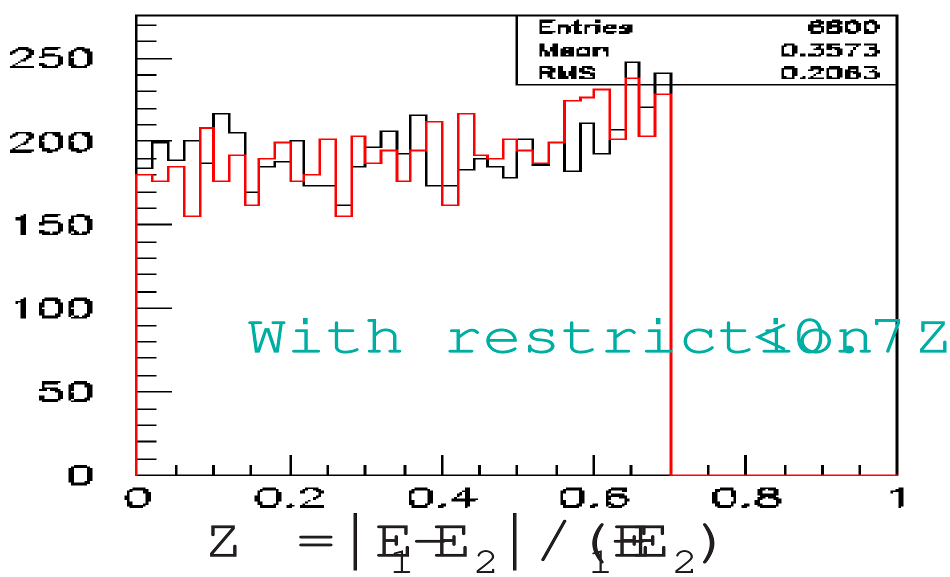

Figure 4.4: energy sharing between 2 photons.

lar.

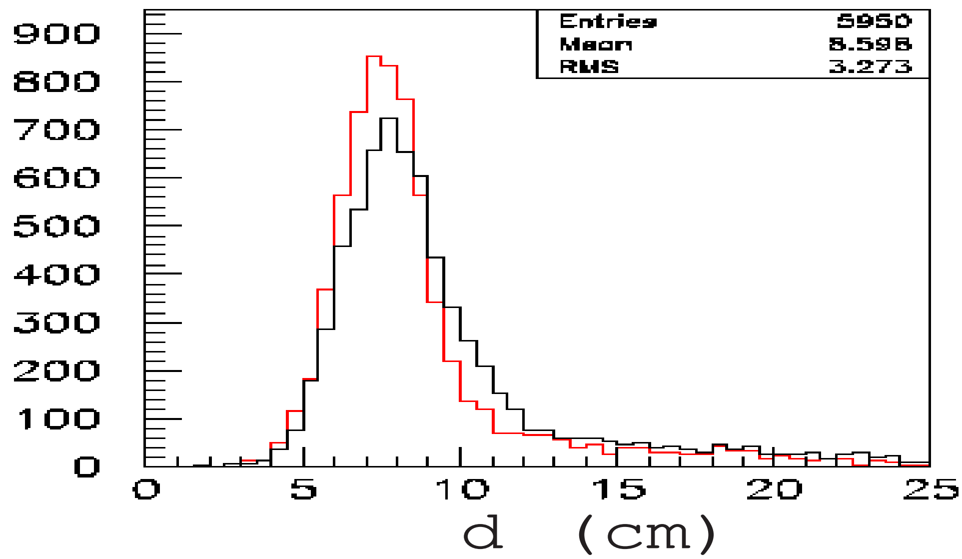

Figure 4.5: Distance between 2 photons.

By virtue of Equation (3.1), we know the distributions of $d_{\gamma\gamma}$ and $M_{\gamma\gamma}$ are correlated. Compared with Figure (4.5), we can see the similarity between the comparison of $M_{\gamma\gamma}$ and that of $d_{\gamma\gamma}$.

Simulation and data looks quite similar. We don't see any indication that the analysis program treat simulation and data differently. With improved calibration and better shower shape function, we expect the agreement between simulation and data to improve. Final FY03 run results should come once the remaining issues (see Section 3.5.9) are resolved.

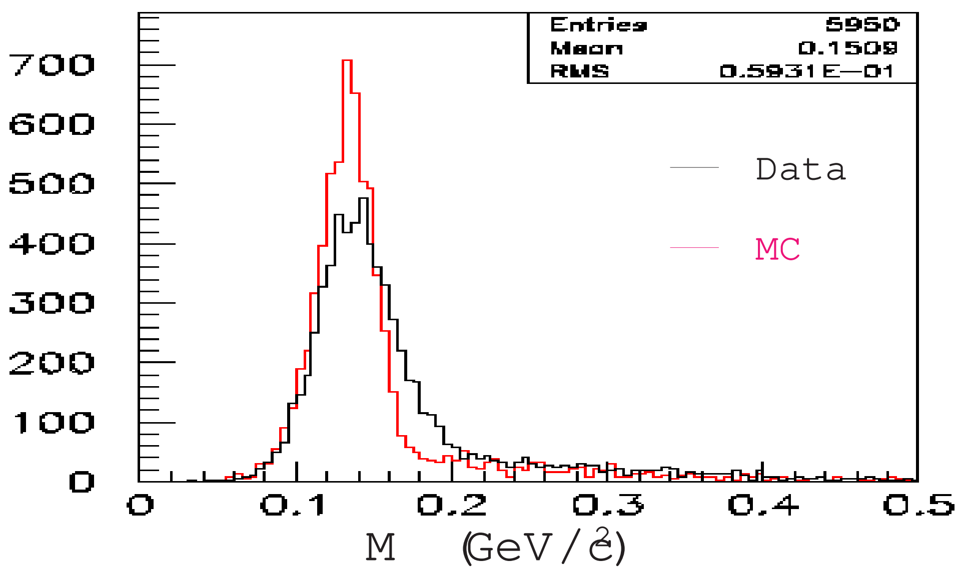

Figure 4.6: Invariant mass of 2 photons.

Chapter 5

Conclusion and Outlook

For the first time, polarized proton beams had been made available in RHIC. Inclusive high energy π^0 mesons production had been measured from $p_\uparrow + p$ collision at $\sqrt{s} = 200$ GeV and forward psudorapidities. The invariant differential cross section was consistent with perturbative QCD calculations. Analyzing power A_N of single spin asymmetry exhibited similar characteristics as previous results at $\sqrt{s} = 20$ GeV.

We also demonstrate a new Pb-glass only analysis tool for the STAR FPD detector. The calibration of detector is still on-going. Once the issues are resolved, final results of inclusive π^0 production measurement for FY03 polarized pp run will follow soon. The technique should be readily applicable to FY03 dAu data, especially for West-South FPD module which faced the deuteron beam. This may prove useful in testing the so-called gluon saturation models [41].

Appendices

Appendix A

Shower-shape Pb-glass Response Simulation

Steve Heppelmann of Penn. State University provided a simple FPD Pb-glass tower responses simulation based on Pb-glass shower-shape functions [36]. The functions are Equations 3.5 and 3.6. For simplicity, only pure $\pi^0 \to \gamma\gamma$ decay events were generated. This was not full simulation by all means, but the event characteristics was not unlike the real data (when we selected events that were most likely π^0), and it was simple and provided us with a way to inter-compare our event reconstruction algorithm with simulation input.

Generated pi^0 has a θ distribution that is 15% of Gaussian around θ_0 with $\sigma = 0.00236$ radian and 85% of exponential $\exp^{-(\theta-\theta_0)/\lambda}$ with $\lambda = 0.02$. The angle θ_0 is the θ angle from the center of West-South FPD module to STAR IP. The ϕ distribution is flat. The energy distribution of π^0 is exponential. Then we require that both photons from the decay are contained within a certain fiducial volume at FPD West-South location. Responses from each individual tower are calculated using the default shower-shape. The ADC counts are randomized using a Gaussian distribution around the calculated value, with $\sigma = 15\% \times \sqrt{E}$, where E is the calculated energy deposit in the tower in GeV. An ADC roundoff is applied to get the final simulated ADC counts.

We used the same default shower shape function for the analysis of this simulation data. Since in this case we know we have used the "correct" shower shape, let's see what the position reconstruction looks like (Figure A.1).

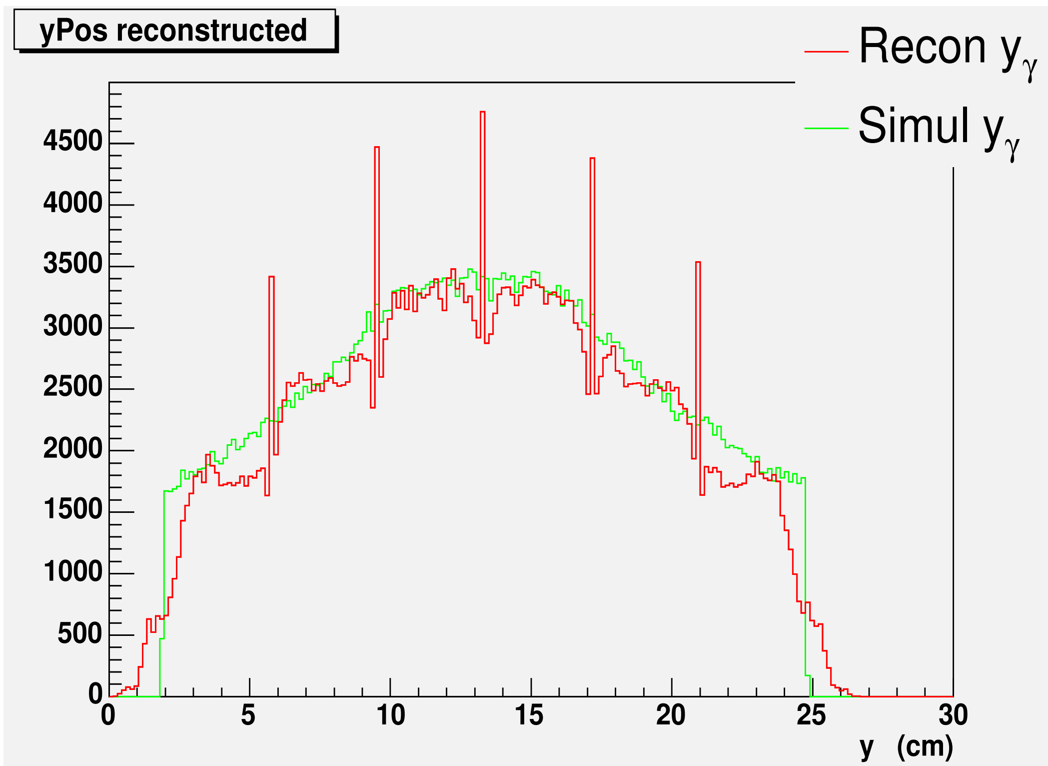

Figure A.1: Comparison of reconstructed and simulated y_γ distribution using default shower shape.

We can see that if we only look at data within a slightly tighter fiducial volume than the FPD module itself, the difference is not big (again, we should also ignore those spikes that are located exactly at the center of towers, as explained in the shower shape discussion in Chapter 2). The morale is, if we find a good shower shape, we should expect a reasonable position reconstruction.

Bibliography

[1] E. Hughes and R. Voss, Annu. Rev. Nucl. Part. Sci. **49**, 303 (1999).

[2] B. Adeva *et al.* (SMC Collaboration), Phys. Rev. **D58**, 112001 (1998).

[3] B. Adeva *et al.* (SMC Collaboration), Phys. Rev. **D58**, 112002 (1998).

[4] D. Adams *et al.*, Phys. Lett. **B261**, 201 (1991).

[5] D. Adams *et al.*, Phys. Lett. **B264**, 462 (1991).

[6] I. Alekseev *et al.*, in *Spin 2002: 15th International Spin Physics Symposium (Aip Conference Proceedings)* (American Institute of Physics, One Physics Ellipse, College Park, MD 20740-3843, 2003), Vol. 675, p. 812.

[7] A. Sokolov and L. Ternov, Phys. Dokl. **8**, 1203 (1964).

[8] S. Weinberg, *The Quantum Theory of Fields. Vol. 1: Foundations* (Cambridge Univ. Press, The Pitt Building, Trumpington Street, Cambridge CB2 1RP, 1995).

[9] J. Jackson, Phys. Review **D66**, 248 (2002).

[10] C. Bourrely and J. Soffer, hep-ph/ 0311101 .

[11] J. Collins, Nucl. Phys. **B396**, 161 (1993).

[12] D. Sivers, Phys. Rev. **D41**, 83 (1990).

[13] J. Qiu and G. Sterman, Phys. Rev. Lett. **67**, 2264 (1991).

[14] J. Qiu and G. Sterman, Nucl. Phys. **B378**, 52 (1992).

[15] J. Qiu and G. Sterman, Phys. Rev. **D59**, 014004 (1999).

[16] Y. Kanazawa and Y. Koike, Phys. Lett. **B478**, 121 (2000).

[17] Y. Kanazawa and Y. Koike, Phys. Lett. **B490**, 99 (2000).

[18] M. Anselmino, M. Boglione, and F. Murgia, Phys. Rev. **D60**, 054027 (1999).

[19] V. Barone, A. Drago, and P. G. Ratcliffe, Phys. Rept. **395**, 1 (2002).

[20] M. Anselmino, M. Boglione, and F. Murgia, Phys. Lett. **B362**, 164 (1995).

[21] M. Anselmino and F. Murgia, Phys. Lett. **B442**, 470 (1998).

[22] J. Collins and D. Soper, Nucl. Phys. **B194**, 445 (1982).

[23] A. Zelenski *et al.*, in *Proceedings of the Part. Acc. Conf.* (IEEE, 10662 Los Vaqueros Circle, P.O. Box 3014, Los Alamitos, CA 90720-1264, 1999), p. 106.

[24] O. Jinnouchi *et al.*, in *Spin 2002: 15th International Spin Physics Symposium (Aip Conference Proceedings, 675)* (American Institute of Physics,

One Physics Ellipse, College Park, MD 20740-3843, 2003), Vol. 675, p. 817.

[25] J. Tojo *et al.*, Phys. Rev. Lett. **89**, 052302 (2002).

[26] B. Kopeliovich, in *AIP Conference Proceedings* (American Institute of Physics, One Physics Ellipse, College Park, MD 20740-3843, 2003), Vol. 675, p. 740.

[27] L. Truman, hep-th/ 0203013 (2002).

[28] K. Johnson *et al.*, Phys. Review **D66**, 207 (2002).

[29] H. Bichsel *et al.*, Phys. Review **D66**, 195 (2002).

[30] C. Allgower *et al.*, Nucl. Instr. Meth. **A499**, 740 (2003).

[31] N. Saito, Ph.D. thesis, Kyoto University, 1995.

[32] H. Spinka *et al.* (unpublished).

[33] A. Drees and Z. Xu, in *Proc. of the Part. Acc. Conf.* (IEEE, 10662 Los Vaqueros Circle, P.O. Box 3014, Los Alamitos, CA 90720-1264, 2001), p. 3120.

[34] J. Sjöstrand, Comp. Phys. Commun. **82**, 74 (1994).

[35] *GEANT 3.21*, CERN program library.

[36] A. Lednev, Nucl. Instrum. Meth. **A366**, 292 (1995).

[37] J.Adams *et al.* (STAR Collaboration), Phys. Rev. Lett. **92**, 171801 (2004).

[38] P. Aurenche *et al.*, Eur. Phys. J. **C13**, 347 (2000).

[39] B. Kniehl, G. Kramer, and B. Pötter, Nucl. Phys. **B597**, 337 (2001).

[40] S.S.Adler *et al.* (PHENIX Collaboration), Phys. Rev. Lett. **91**, 241803 (2003).

[41] A. Dumitru and J. Jalilian-Marian, Phys. Rev. Lett. **89**, 022301 (2002).

Vita

Yiqun Wang was born in Guiyang, Guizhou Province, China on January 14, 1971, the son of Xiang-hong Wang and Su-zen Yuan. He received the Bachelor of Science degree in Physics from Peking University, Beijing, China in July 1991. He went back to his hometown, and worked in Guizhou Institue of Transportation for the next several years. In the meaning, he brushed up his English skills and took the TOEFL and GRE tests. Then he applied to the University of Texas at Austin for enrollment in their physics program. He was accepted and started graduate studies in August, 1994. At first, he majored in theoretical physics, string theory in particular. In 2000, he transferred to high energy nuclear physics, and participated in BNL's RHIC run FY02 and FY03 as a member of the STAR collaboration.

Permanent address: 23 Belmont Drive
Shirley, New York 11967

This dissertation was typeset with LaTeX[†] by the author.

[†]LaTeX is a document preparation system developed by Leslie Lamport as a special version of Donald Knuth's TeX Program.